Low frequency coherent Raman spectroscopy

Randy Bartels, Dan Oron, Hervé Rigneault

▶ **To cite this version:**

Randy Bartels, Dan Oron, Hervé Rigneault. Low frequency coherent Raman spectroscopy. Journal of Physics: Photonics, 2021, 3 (4), pp.042004. 10.1088/2515-7647/ac1cd7 . hal-03343175

HAL Id: hal-03343175
https://hal.science/hal-03343175

Submitted on 16 Sep 2021

HAL is a multi-disciplinary open access archive for the deposit and dissemination of scientific research documents, whether they are published or not. The documents may come from teaching and research institutions in France or abroad, or from public or private research centers.

L'archive ouverte pluridisciplinaire **HAL**, est destinée au dépôt et à la diffusion de documents scientifiques de niveau recherche, publiés ou non, émanant des établissements d'enseignement et de recherche français ou étrangers, des laboratoires publics ou privés.

Distributed under a Creative Commons Attribution 4.0 International License

JPhys Photonics

TOPICAL REVIEW • OPEN ACCESS

Low frequency coherent Raman spectroscopy

To cite this article: Randy A Bartels *et al* 2021 *J. Phys. Photonics* **3** 042004

View the article online for updates and enhancements.

This content was downloaded from IP address 139.124.244.81 on 16/09/2021 at 08:39

Journal of Physics: Photonics

OPEN ACCESS

RECEIVED
5 January 2021

REVISED
8 May 2021

ACCEPTED FOR PUBLICATION
8 August 2021

PUBLISHED
13 September 2021

Original Content from this work may be used under the terms of the Creative Commons Attribution 4.0 licence.

Any further distribution of this work must maintain attribution to the author(s) and the title of the work, journal citation and DOI.

TOPICAL REVIEW

Low frequency coherent Raman spectroscopy

Randy A Bartels[1,*], Dan Oron[2] and Hervé Rigneault[3]

[1] Departments of Electrical and Computer Engineering and Biomedical Engineering, Colorado State University, Fort Collins, CO 80523-1301, United States of America
[2] Weizmann Institute of Science, Rehovot, Israel
[3] Aix Marseille Univ, CNRS, Centrale Marseille, Institut Fresnel, Marseille, France
* Author to whom any correspondence should be addressed.

E-mail: randy.bartels@colostate.edu

Keywords: Raman spectroscopy, terahertz Raman, coherent Raman, impulsive stimulated Raman scattering

Abstract

We revisit low frequency coherent Raman spectroscopy (LF-CRS) and present a unified theoretical background that provides consistent physical pictures of LF-CRS signal generation. Our general framework allows to compute the signal to noise ratio in the multitude of possible LF-CRS, and more generally CRS, experimental implementations both in the spectral and time domain.

1. Introduction: low-frequency Raman scattering

The Raman effect, first predicted by Smekal in 1923 [1] and experimentally observed by Raman and Krishnan [2] and Landsberg and Mandelstam [3] in 1928, describes the inelastic scattering of light due to the induced-dipole interaction between light and molecules and has become a leading tool in performing vibrational spectroscopy and label-free chemically selective optical microscopy. Raman spectroscopy mostly addresses intramolecular bond vibrations and their possible alteration due to the environment (peak shifts and relative intensities) that have their signatures in the so-called 'fingerprint' region (between 200 and 1800 cm^{-1}). This fingerprint region is addressed by commercial Raman spectrometers with applications in material sciences [4], biology and medical fields [5]. The low frequency vibrational spectral range, below 200 cm^{-1}, has been less explored. Low frequency Raman spectroscopy (LFRS) is the signature landscape for intermolecular interactions such as translation, libration, and deformations of the molecular skeleton within the crystal lattice [6]. As an example, low frequency Raman is an effective technique for crystal identification and has found applications in pharmacology to detect polymorphism in active molecules [7], improving the control of drug synthesis in tablets and powders. LFRS has also been used jointly with the complementary low-frequency vibrational spectroscopy methods of inelastic neutron scattering [8] and terahertz spectroscopy [9] as a potent tool in the study of transient molecular dynamics in liquids. In addition, low frequency Raman signatures offer new potential for the detection of protein secondary structure [10, 11], ligand binding [12], vibrational coupling in the excited state [13], and the detection of viral capsids [14, 15].

LFRS presents two types of challenges. The first relates to the experimental difficulty in efficiently filtering out the incoming laser excitation light while retaining nearby spectral frequencies. Low frequency Raman spectroscopy was traditionally performed using triple monochromators and was experimentally challenging [16]. In the past decade, this difficulty has been solved using volume holographic grating based notch filters [17–19] that enable the acquisition of high-quality ultralow-frequency Raman spectra for vibrational shifts as low as a few wavenumbers [20]. Notably, however, this technological advance does not alleviate the issue of long integration times (>1 ms) because of the weak Raman scattering cross section.

The second challenge relates to the fundamental physics of low frequency vibrations. In crystaline materials a background-free vibrational spectrum can be usually obtained down to a very low vibrational frequency, which has recently been extensively used in the study of pharmaceutical compounds, hybrid organic-inorganic crystals and 2D materials. In contrast, in liquids (and in amorphous materials or crystals exhibiting strong anaharmonicity) there are strong Rayleigh wings around the zero frequency arising from the slow dynamics in the liquid. While this has been used as a tool to study vibrational relaxation dynamics in liquids for many decades [21], the broadened spectral features makes low-frequency spectroscopy of low

© 2021 The Author(s). Published by IOP Publishing Ltd

concentration solutes and, more generally, of biological specimens, difficult, as these weak signals are often masked by a featureless Rayleigh scattering.

Although terahertz spectroscopy has been reported long ago, there has been recently a revival of low frequency Raman investigations with the advances of coherent Raman scattering (CRS) techniques [22–27] that have the ability to boost the spontaneous Raman signal by orders of magnitude, taking advantage of the coherent excitation of vibrational states provided by ultra-short laser pulses [28, 29]. Because coherent Raman allows fast spectroscopy and imaging in the low frequency range with pixel dwell time as short as few microseconds [27], it opens opportunities to explore the low frequency range with applications in material, biology and medical sciences. However, the impact of these reports and the role CRS can play in advancing our ability to study materials and biological systems with low frequency Raman spectroscopy is difficult to assess due to a lack of a general and unified framework on how to perform low coherent Raman spectroscopy (i.e. spectral or time domain approaches) and how to quantitatively compare these methods by evaluating their relative signal to noise ratio (SNR).

In this Review, we directly address this deficiency by establishing a unified theoretical framework for the known low frequency coherent Raman spectroscopy (LF-CRS) methods and deriving formulae for the SNR to quantitatively compare the performance of these methods. Here, we revisit LF-CRS both from its theoretical background and its possible implementations to provide a consistent physical picture of signal generation in these methods. Throughout this discussion we will make use of *système international* (SI) units and for all quantities, we will provide order of magnitude numbers which place the measurements discussed in numerical context, meaning that we will present estimates of integration times for experimental conditions that are required to attain a given SNR.

2. Theory of low-frequency coherent Raman spectroscopy

The theory of Raman scattering is well developed and many excellent review and tutorial treatments are available [30–36]. Rather than rework this treatment, we provide a brief review of coherent Raman optical scattering. We will assume that the wavelengths of light used in the experiment are not resonant with electronic transitions and exhibit negligible multiphoton absorption. Under these approximations, we may invoke the Born–Oppenheimer approximation (BOA) in which we assume that the rapid motion of the electrons adiabatically follow the nuclei with this displacement [37]. Here we refresh the reader on the analysis of the induced nonlinear polarization density within the BOA [38].

2.1. The time-domain coherent Raman response

2.1.1. Microscopic nonlinear dipole response

A coherent Raman interaction is a four-wave mixing process involving three incident fields and a coherently Raman scattering (CRS) signal that we wish to detect. To model the CRS process, we consider the third-order nonlinear polarization density, $P^{(3)}$. To obtain the relevant macroscopic polarization density, we begin with a single molecule subject to an intense, non-resonant field and consider the induced electric dipole moment in that molecule

$$p_I = m_I + \alpha_{IJ}\mathcal{E}_J + \beta_{IJK}\mathcal{E}_J\mathcal{E}_K + \gamma_{IJKL}\mathcal{E}_J\mathcal{E}_K\mathcal{E}_L + \cdots, \tag{1}$$

where summation over repeated indices is implied. The terms contributing to the expansion in the dipole moment are the permanent moment, m_I, the polarizability, α_{IJ}, the hyperpolarizability, β_{IJK}, and the second hyperpolarizability, γ_{IJKL}, and higher order terms in the dipole moment have been suppressed. Throughout this review, we will provide estimates for all practical quantities to provide an appreciation for the experimental capabilities and limitations. Some typical numbers for these quantities for acetonitrile are: $m_I = 1.3 \times 10^{-29}$ C m, $\alpha_{IJ} = 5.0 \times 10^{-40}$ C V^{-1} m^2, $\beta_{IJK} = 1.4 \times 10^{-51}$ C V^{-2} m^3, $\gamma_{IJKL} = 2.9 \times 10^{-61}$ C V^{-3} m^4 [39]. The field that drives the induced dipole, $\mathcal{E}$, with units of V m^{-1}, is a real electric field that will generally be assumed to be a short laser pulse.

2.1.2. Conversion from the microscopic to the macroscopic nonlinear response

Conversion from the microscopic model, equation (1), to a macroscopic quantity takes into account the number density of molecules, N, the local field correction, f for each field, as well as the projection from the lab coordinates (*ijkl* indices) to the local tensor frame (*IJKL* indices) of the polarizabilities [40–45]. Due to our interest in the third-order response, we connect the microscopic dipole moment terms to the macroscopic polarization density through direction cosines, r_{aA}, obtained from the rotation matrix **R**, where upper case and lower indices denote molecular frame coordinates and the lab coordinates, respectively.

We focus on the third order nonlinear susceptibility due to its relevance to CRS, and in the laboratory frame, the macroscopic third order nonlinear susceptibility is

$$\chi^{(3)}_{ijkl} = \frac{N}{\varepsilon_0}\gamma_{IJKL} f_i f_j f_k f_l \int r_{iI}\, r_{jJ}\, r_{kK}\, r_{lL}\, G(\Omega)\, d\Omega := \frac{N}{\varepsilon_0}\langle\gamma\rangle_{ijkl}. \tag{2}$$

Note that we are suppressing the optical frequency arguments in the local field correction factors, $f_j = (n_j^2+2)/3$, the polarizability terms, and the nonlinear susceptibility for simplicity of notation. Using the refractive index (RI) of water, $n \sim 1.33$, we see that a typical local field correction factor is $f \sim 1.26$. $G(\Omega)$ is the orientational probability density of the molecules within the specimen [45].

The nonresonant nonlinear susceptibility plays a critical role in CRS, and to estimate the impact quantitatively, we provide estimates of this quantity for both neat acetonitrile and water. At room temperature the density of neat water is $N_{water} \sim 3.33 \times 10^{22}$ cm^{-3}, leading to an electronic-induced third order optical susceptibility of $\chi^{(3)}_{nr,H_2O} \sim 8.4 \times 10^{-22}\,(\text{m V}^{-1})^2$ by making use of the second hyperpolarizability of water of $\langle\gamma_{water}\rangle \sim 1.12 \times 10^{-61}$ C V^{-3} m^4 [46]. The subscript nr indicates the non-vibrationally-resonant electronic third order nonlinear contribution, which is frequently abbreviated at the nonresonant term. Similarly, using the second hyperpolarizablity of acetonitrile, and noting that the number density under neat conditions is $N_{CH_3CN} \sim 1.14 \times 10^{22}$ cm^{-3}, leads to an estimate of the electronic-induced third order optical susceptibility of $\chi^{(3)}_{nr,CH_3CN} \sim 9.29 \times 10^{-22}\,(\text{m V}^{-1})^2$. When the acetonitrile concentration drops to 1 mM, the nonresonant susceptibility drops accordingly to $\chi^{(3)}_{nr,CH_3CN} \sim 4.91 \times 10^{-26}\,(\text{m V}^{-1})^2$. As a result, under most conditions, we take the nonresonant susceptibility as that of the solvent, which is water in biological systems.

2.1.3. Time domain nonlinear polarization density

The coherent Raman response is determined by the Raman contribution to the second hyperpolarizability of the molecule that gives rise to a macroscopic third order polarization density. Within a semiclassical treatment the polarization density is the trace of the dipole moment operator, $\hat{p}_i$, acting on the equilibrium density matrix, ρ_0, providing the expression $\mathcal{P}_i = N\text{Tr}[\tilde{p}_i\,\rho_0]$, where we are using the interaction dipole operator for dipole moment $\tilde{p}_i(t) = U_0^{-1}(t)\,\hat{p}_i\,U_0(t)$, where $U_0(t) = \exp(-iH_0(t))$, and H_0 indicates the unperturbed Hamiltonian [38, 47]. We will adopt the expectation value notation of $\mathcal{P}_i = N\langle\hat{p}_i\rangle$.

The time-domain third-order polarization density can be written from the incident field that oscillates at frequency ω and of a time-domain response function, $\mathcal{S}^{(3)}$, [38, 47–49]

$$\mathcal{P}^{(3)}(t) = \varepsilon_0 \int_{-\infty}^{\infty} dt_3 \int_{-\infty}^{\infty} dt_2 \int_{-\infty}^{\infty} dt_1\, \mathcal{S}^{(3)}(t_3,t_2,t_1)\mathcal{E}(t-t_3)\mathcal{E}(t-t_2)\mathcal{E}(t-t_1), \tag{3}$$

with the real field denoted by $\mathcal{E}$. Invoking our approximation that the interacting light frequencies are far from the dipole resonances, we may neglect those interactions in the computed third order temporal response. In this approximation, two terms contribute the the third order polarization density: the electronic (nonresonant), $\mathcal{P}^{(3)}_{nr}$, and the vibrationally resonant, $\mathcal{P}^{(3)}_{VR}$, terms. These two terms appear in the total third order polarization density, $\mathcal{P}^{(3)} = \mathcal{P}^{(3)}_{nr} + \mathcal{P}^{(3)}_{VR}$. In the non-(electronic)-resonant BOA approximation, the time-domain response functions read for the nonresonant contribution

$$S_i^{(3)\,nr}(t) = \frac{N}{\varepsilon_0}\langle\gamma^{nr}\rangle_{ijkl}\,\delta(t-t_1)\,\delta(t_1-t_2)\,\delta(t_2-t_3) \tag{4}$$

and for the term that contributes to change in polarizability [50–52]

$$S^{(3)}_{VR}(t,s) = \frac{N}{\varepsilon_0}\frac{i}{2\hbar}\langle\langle[\tilde{\alpha}_{ij}(t),\tilde{\alpha}_{kl}(s)]\rangle\rangle\Theta(t-s), \tag{5}$$

where the commutator is $[A,B] = AB - BA$, $\tilde{\alpha}$ the polarizability operator and $\Theta(t)$ the Heavyside step function. With these expressions, the nonresonant polarization density simplifies to

$$\mathcal{P}_i^{(3)\,nr}(t) = \frac{N}{\varepsilon_0}\langle\gamma^{nr}\rangle_{ijkl}\,\mathcal{E}^3(t) \tag{6}$$

and the third order nonlinear response to the change in polarizability due to Raman-active vibrational modes reads

$$\mathcal{P}_i^{(3)\,VR}(t) = \frac{N}{\varepsilon_0}\frac{i}{2\hbar}\mathcal{E}(t)\int_{-\infty}^{\infty} ds\,\langle\langle[\tilde{\alpha}_{IJ}(t),\tilde{\alpha}_{KL}(s)]\rangle\rangle\mathcal{E}^2(s)\,\Theta(t-s). \tag{7}$$

Note that the double angle brackets includes the expected value of the interaction polarizability operator, and the orientational averaging to account for polarization effects.

2.1.4. Expansion polarizability operator into normal mode vibrations

To relate the polarizablity operator to the desired coherent vibrational spectrum, the correlation of the polarizability in this truncated expansion then is expressed as

$$\langle[\tilde{\alpha}_{IJ}(t),\tilde{\alpha}_{KL}(s)]\rangle = -2i\sum_{m,n} c_m \langle vm|\alpha_{ij}|vn\rangle\langle vn|\alpha_{kl}|vm\rangle\, e^{-\frac{1}{2}\Gamma_{v,mn}(t-s)}\,\sin[\Omega_{v,mn}(t-s)]. \tag{8}$$

Each vibrational mode v is expanded in the basis of vibrational states of $|vm\rangle$ with eigenenergy $E_m = \hbar\omega_m$ of the unperturbed ground state Hamiltonian. For the vth vibrational mode and statistical weight c_m that is usually given by Boltzmann statistics and nuclear statistical weighting set by the spin statistics [38]. The vibrational beat frequency is $\Omega_{v,mn} = (E_m - E_n)/\hbar$ and the dephasing has been included at the rate $\Gamma_{v,mn}$ [47].

Vibrations in a molecular or solid-state material may induce fluctuations in the polarizability. The standard approach for analyzing these molecular vibrations is to decompose the motions into a normal (approximately) set of displacements. These physical length displacements, R_v, are usually described in a mass-weighted coordinates $Q_v = \sqrt{m_v}R_v$, where m_v is the reduced mass of the vibrational coordinate. Under conditions of weak vibrational displacement, the Placzek expansion [53]

$$\alpha_{IJ} = \alpha^0_{IJ} + \sum_v \frac{\partial\alpha_{IJ}(Q_v=0)}{\partial Q_v}Q_v + \sum_{v,w}\frac{\partial^2\,\alpha_{IJ}(Q_v,Q_w=0)}{\partial Q_v\partial Q_w}Q_vQ_w + \cdots, \tag{9}$$

successfully describes the effects of Raman scattering. We will truncate the expansion at the first-order term and consider only a single vibrational mode, although expansion to multiple modes is trivial. We also adopt a simplified notation where we define the differential polarizability as $\alpha'_{IJ} \equiv \partial\alpha_{IJ}(Q_v=0)/\partial Q_v$ so that we expand the polarizability as $\alpha_{IJ} = \alpha^0_{IJ} + \alpha'_{IJ}Q_v$. The differential polarizability is related to the differential Raman scattering cross-section, $d\sigma/d\Omega$, through the relationship $(\partial\alpha_{IJ}/\partial Q_v)^2_0 = (16\pi^2 c^4\varepsilon_0^2)/(Q^2_{\rm ho})$ $(d\sigma/d\Omega)_R(1-\exp[-\hbar\Omega_v/k_B T])$. The subscript 0 denotes the differential polarizability for the equilibrium molecule structure. Here, c is the speed of light, ω_s is the scattered light optical frequency, T is the temperature in K, k_B is the Boltzmann constant, and $Q_{\rm ho} = \sqrt{\hbar/2\,\Omega_v}$ is the harmonic oscillator normal coordinate displacement. Taking the differential Raman scattering cross section for the 920.5 $\rm cm^{-1}$ C-C symmetric stretch vibrational mode in acetonitrile of $(d\sigma/d\Omega)_R = 5.6\ \times 10^{-29}$ $\rm cm^2/ster$ with spontaneous Raman scattering with an incident laser line of $\lambda = 532$ nm [54], we estimate a differential polarizability of $(\partial\alpha_{IJ}/\partial Q_v)_0 = 1.2\ \times 10^{-16}$ C m $\rm V^{-1}\sqrt{kg}$.

Upon making use of the Placzek expansion and accounting for the orthogonality of the vibrational eigenmodes, the polarizablity matrix elements for Raman scattering initial and final states, labeled n and m, respectively, become $\langle vm|Q_v|vn\rangle$, which allows an expression for the Raman contribution to the third-order polarization density through the term

$$\langle[\tilde{\alpha}_{IJ}(t),\tilde{\alpha}_{KL}(s)]\rangle = -2i\sum_{m,n} c_m A^{v,mn}_{ijkl}\, e^{-\frac{1}{2}\Gamma_{mn}(t-s)}\,\sin[\Omega_{v,mn}(t-s)] \tag{10}$$

and where we have defined the amplitude term $A^{v,mn}_{ijkl} = \langle\alpha'_v\rangle_{ij}\langle\alpha'_v\rangle_{kl}|\langle vm|Q_v|vn\rangle|^2$. Note that for a harmonic oscillator, the matrix elements simplify to $|\langle vm|Q_v|vn\rangle|^2 = \hbar/2\,\Omega_v$. Here we have defined the orientational averaging of the differential polarizabilty as $\langle\alpha'\rangle_{pq} = \langle f_p f_q r_{pP} r_{qQ}\alpha'_{PQ}G(\Omega)\rangle_\Omega$.

2.1.5. Time domain CRS response function

Now, we may obtain the time domain response function for the change in polarizability for stimulated Raman response

$$\mathcal{S}^{\rm VR}_{ijkl}(t) = \frac{N}{\varepsilon_0}\sum_{v,m,n} c_m \frac{\langle\alpha'_v\rangle_{ij}\langle\alpha'_v\rangle_{kl}}{\Omega_{v,mn}}\,h^{mn}_v(t), \tag{11}$$

where we have defined the vibrational impulse response, $h^{mn}_v(t)$, in appendix A. Note that if we consider a single vibrational mode transition energy between the ground and first vibrational levels that is well above the thermal energy (200 $\rm cm^{-1}$), then we have a simplified expression that takes the more common form of the damped impulse response of a simple harmonic oscillator $\propto e^{-\frac{1}{2}\Gamma_{v,mn}(t)}\,\sin[\Omega_{v,mn}t]\,\Theta(t)$.

For the case of vibrational frequencies with an energy well above thermal energies, the initial population at thermal equilibrium is confined to the lowest vibrational level with high probability, so that $c_{0m} = \delta_{0,m}$, the quantum beating driven by the excitation of the vibrational coherences can be described as a pure state. Furthermore, for weak vibrational excitation, the ground electronic state is well approximated by a harmonic

oscillator, so that the vibrational coherences are dominated by harmonic oscillator selection rules, i.e. $m - n = \pm 1$. In this high vibrational frequency limit, we may simplify our coherent vibrational response function to take the form of a sum of damped sinusoidal oscillations

$$\mathcal{S}^{\mathrm{CRS}}_{ijkl}(t) = \frac{N}{\varepsilon_0} \sum_{\nu} \langle \alpha'_{\nu} \rangle_{ij} \langle \alpha'_{\nu} \rangle_{kl} \frac{\sin[\Omega_{\nu} t]}{\Omega_{\nu}} e^{-\frac{1}{2}\Gamma_{\nu} t} \Theta(t). \tag{12}$$

In the harmonic oscillator approximation, the vibrational frequency between adjacent levels are the same, $\Omega_{\nu,mn} = \Omega_{\nu}$, and where we have made use of the harmonic order matrix element.

In the high frequency limit, it is sufficient to describe the coherent vibrational response as a driven classical oscillator, with the vibrational displacement following Newtonian mechanics, $m_{\nu}\ddot{R}_{\nu} + 2m_{\nu}\Gamma_{\nu}\dot{R}_{\nu} + m_{\nu}\Omega_{\nu}^2 R_{\nu} = F(t)$. The vibration displacement is driven by the force exerted by the induced electric dipole interacting with the applied electric field, giving the driving term $F(t) = \nabla[\mathbf{E}(\mathbf{t}) \cdot \alpha \cdot \mathbf{E}(\mathbf{t})]$. By applying the Placzek expansion and converting to mass-weighted coordinates, we obtain the harmonic oscillator model used for classical Raman calculations, $\ddot{Q}_{\nu} + 2\Gamma_{\nu}\dot{Q}_{\nu} + \Omega_{\nu}^2 Q_{\nu} = \frac{1}{2}\left\langle F(t)/\sqrt{m_{\nu}} \right\rangle_t$, where the brackets represent a time-average over the driving term. Excellent discussions of the high frequency limit description of the coherent Raman response can be found in a number of reviews and tutorials [36, 55].

In the region of low-frequency vibrations, which we define as vibrational modes with an energy at or below the thermal energy of $k_B T = 200\ \mathrm{cm}^{-1}$ at room temperature $T = 300$ K and where k_B is the Boltzmann constant, the initial state must be described as a mixed state because many initial vibrational levels will be occupied. As a consequence, the sum over m must be retained. Moreover, it is likely that the high vibrational levels will also sample the anharmonicity of the vibrational potential, which leads to a dispersion in the quantum beat frequencies. The aspects of the initial statistical distribution of excited energy levels and the effects of the anharmonicity of the the energy level spacing is well studied in the context of rotational wavepacket revivals [43, 56–60].

2.1.6. Third-order nonlinear polarization density

By assuming that the optical fields used in the coherent Raman response are far detuned from electronic absorption and by invoking the BOA, we obtain the time-domain third-order nonlinear response for CRS is given by

$$\mathcal{P}_i^{(3),\mathrm{CRS}}(t) = \varepsilon_0 \mathcal{E}(t) \int_{-\infty}^{\infty} ds \mathcal{S}^{\mathrm{CRS}}_{ijkl}(t-s) \mathcal{E}^2(s). \tag{13}$$

The non-resonant contribution is similarly

$$\mathcal{P}_i^{(3),\mathrm{nr}}(t) = \varepsilon_0 \mathcal{E}(t) \int_{-\infty}^{\infty} ds \mathcal{S}^{\mathrm{nr}}_{ijkl}(t-s) \mathcal{E}^2(s), \tag{14}$$

with the time-domain response function for the non-resonant response given by

$$\mathcal{S}^{\mathrm{nr}}_{ijkl}(t) = \frac{N}{\varepsilon_0} \langle \gamma^{\mathrm{nr}} \rangle_{ijkl} \delta(t). \tag{15}$$

2.1.7. Effective time-varying perturbation to the linear optical susceptibility

The total real polarization density driven in the medium by the third-order nonlinear response,

$$\mathcal{P}_i^{(3)}(t) = \mathcal{P}_i^{(3),\mathrm{nr}}(t) + \mathcal{P}_i^{(3),\mathrm{CRS}}(t) := \varepsilon_0 \delta\chi^{(1)}_{ij,\mathrm{eff}}(t) \mathcal{E}_j(t), \tag{16}$$

that arises from the combination of the electronic nonresonant response and the forced vibrational response may be treated as an effective time-varying perturbation to the linear optical susceptibility, $\delta\chi^{(1)}_{ij,\mathrm{eff}}(t)$. If we inject an optical field, $\mathcal{E}$, into the interaction, then as this field propagates the third-order polarization density terms described above modify the propagation of this field. The effective time-varying perturbation to the linear optical susceptibility, $\delta\chi^{(1)}_{\mathrm{eff}}(t)$ as experienced by the field $\mathcal{E}(t)$ has been reported in [49, 56, 61, 62]. The most common form of this effective linear susceptibility perturbation is self and cross phase modulation that arises from the nonresonant term [63].

In equation (16), we have introduced the time-varying effective linear optical susceptibility driven by a combination of the non-resonant term and the forced Raman response

$$\delta\chi^{(1)}_{\mathrm{eff}}(t) = \int_{-\infty}^{\infty} ds \left\{ \mathcal{S}^{\mathrm{nr}}_{ijkl}(t-s) + \mathcal{S}^{\mathrm{CRS}}_{ijkl}(t-s) \right\} \mathcal{E}^2(s). \tag{17}$$

This approach to effective time-varying susceptibility has also been extended to nonlinear optical processes [42, 44, 64, 65].

Up to now we have focused on a single field incident onto the material supporting vibrational levels. We will see in the next sections that when several incoming fields are considered the vibrational signature of matter can be clearly imprinted in some of the fields and easily isolated. In this framework, we will consider two incident optical fields at frequencies ω_1 and ω_2 that drive an oscillating nonlinear dipole that induces a third field incident at frequency ω_3 to scattering to the optical frequency ω_4 ($\omega_1 - \omega_2 + \omega_3 = \omega_4$). The complex representation of the induced nonlinear polarization density at ω_4 reads

$$\mathcal{P}_i(\mathbf{r},t) = \hat{e}_i P_i(\mathbf{r},t)\exp[-i\omega_4 t] + \text{c.c.}. \tag{18}$$

Note that the specific oscillation frequency of the polarization density will depend on the incident fields and the nonlinear interaction and $\hat{e}_i$ is the polarization direction of the nonlinear polarization density. To explicitly express the nonlinear polarization with the fields involved in the process, we write the total real field as a sum over incident polarizations, $\hat{e}_a$, and center optical frequency, ω_a ($\omega_a = \omega_{1,2,3,4}$), of the pulsed fields, which reads

$$\mathcal{E}(\mathbf{r},t) = \sum_a \hat{e}_a A_{a,0}\, u(\mathbf{r},t)\exp[i(k_a z - \omega_a t)] + \text{c.c.}. \tag{19}$$

Here we assume that z is our nominal direction of propagation and that all fields propagate along the same direction and that c.c. denotes the complex conjugate. The field component denoted by a ($a = 1,2,3,4$) possesses a peak amplitude of $A_{a,0}$, and the spatial and temporal field variation is accounted for by the complex envelope function $u(\mathbf{r},t)$ where we have set the normalization of this field such that $|u(\mathbf{r},t)| \leq 1$. The full complex envelope is written as $A_j(\mathbf{r},t) = A_{j,0}\, u(\mathbf{r},t)$. When possible, the field spatial and temporal arguments will be suppressed for brevity, but we will tacitly assume those dependencies.

The complex time-dependent polarization density for both the nonresonant and CRS processes takes on the form

$$P_i^{(3),\mathrm{p}}(t) = 6\varepsilon_0\, e^{-i\Delta_{\mathrm{rad}}t} A_{k,0} A_{l,0}^* A_j(t) \int_{-\infty}^{\infty} ds\, \mathcal{S}_{ijkl}^{\mathrm{p}}(t-s)\, e^{i\Delta_{\mathrm{pu}}s} |u(s)|^2, \tag{20}$$

where we assume that the jth field is distinguishable from the others. Here, we denote CRS by p = VR and the nonresonant response by p = nr. The detuning of center excitation frequencies of the driving fields is defined as $\Delta_{\mathrm{pu}} = \omega_2 - \omega_1$. These driving fields are responsible for the forced Raman response that imparts scattering from the incident probe field frequency at ω_3 to the signal field frequency at ω_4. We define also a difference scattering frequency difference as a detuning parameter $\Delta_{\mathrm{rad}} = \omega_4 - \omega_3$. We have further assumed the all of the normalized field envelopes are identical $u_j(t) \to u(t)$. As we will see later the fields at ω_1, ω_2 and ω_3 are usually referred as the pump, Stokes and probe fields, respectively, whereas the scattered fields at ω_4 is referred as coherent anti-Stokes scattering (CARS) (when $\omega_4 = \omega_1 - \omega_2 + \omega_3$) or coherent Stokes Raman scattering (when $\omega_4 = \omega_2 - \omega_1 + \omega_3$) [36].

2.2. Frequency domain response of low frequency CRS

The form of both the non-resonant and coherent, vibrationally resonant contributions to the third-order nonlinear optical susceptibility that produce the effective time-varying linear susceptibility both take the form of a convolution in the time domain. The frequency domain polarisation density is obtained by taking the Fourier transform of equation (20) leads to the expression [66]

$$\tilde{P}_i^{(3)}(\omega + \Delta_{\mathrm{rad}}) = 6\varepsilon_0 A_{k,0} A_{l,0}^* T_n \tilde{A}_j(\omega) * \left\{ \chi_{ijkl}^{(3)}(\omega) \cdot \tilde{D}(\omega - \Delta_{\mathrm{pu}}) \right\}. \tag{21}$$

Here, $\tilde{A}_j(\omega) = \mathcal{F}\{A_j(t)\}$ is the spectrum of the temporal field envelope and $*$ denotes the convolution operator. The driving term from the incident field is given by the convolution of the spectrum of the real driving field that describes the relative spectral density of the excitation strength of the vibrational mode [67]

$$\tilde{D}(\omega) = T_n^{-1} \int_{-\infty}^{\infty} dt\, |u(t)|^2 e^{-i\omega t} = T_n^{-1}\, \tilde{U}(\omega) \star \tilde{U}(\omega). \tag{22}$$

Here $\star$ denotes the correlation operator and the spectrum of the pulse envelope reads $\tilde{U}(\omega) = \mathcal{F}\{u(t)\}$. The mean pulse time is defined as $T_n = \int |u(t)|^2 dt$ and it follows from equation (22) that $\tilde{D}(0) = 1$. The

third-order nonlinear susceptibility is the Fourier transform of the third order temporal response function, and reads

$$\chi^{(3)}_{ijkl}(\omega) = \frac{1}{6}\mathcal{F}\{S^{(3)}_{ijkl}(t)\} = \frac{N}{6\varepsilon_0}\left(\langle\gamma^{\rm nr}\rangle_{ijkl}\,\delta_{k,l} + \sum_{v,m,n}\frac{c_m\,\langle\alpha'_v\rangle_{ij}\,\langle\alpha'_v\rangle_{kl}}{\Omega^2_{v,mn} - \omega^2 - i\Gamma_{v,mn}\,\omega}\right). \tag{23}$$

We identity the first term as the nonresonant nonlinear susceptibility, $\chi^{(3),{\rm nr}}_{ijkl}(\omega)$, and the second term as the CRS vibrationally-resonant term, $\chi^{(3),{\rm VR}}_{ijkl}(\omega)$. Using the differential polarizability number quoted above for the 920.5 $\rm cm^{-1}$ C–C symmetric stretch mode of acetonitrile, at typical liquid densities, the peak value of the nonlinear susceptibility on vibrational resonance is on the order of $\chi^{(3),{\rm VR}}(\Omega_v) \sim -i2.94\ \times 10^{-20}\ \rm m^2\ V^{-2}$. A primary impact of low frequency Raman is the potential of more states that are initially populated and more sampling of the dispersion in the beat frequencies, which will result in dephasing of wavepackets prepared by the initial excitation, as observed in rotational revivials in gas phase molecules [43, 56, 67, 68].

The effective perturbation to the linear optical susceptibility defined in equation (16) can now be written in terms of a forced Raman response that is developed in appendix A. The total effective linear polarizability is $\delta\chi^{(1)}_{ij,\rm eff}(t) = \delta\chi^{(1),{\rm nr}}_{ij,\rm eff}(t) + \delta\chi^{(1),{\rm VR}}_{ij,\rm eff}(t)$. Because the electronic response is assumed to respond instantaneously, the transient effective linear susceptibility adiabatically follows the incident pulse intensity, which is proportional to the temporal driving term, $d(t) = |u(t)|^2/T_n$, leading to the expression of the nonresonant contribution from the electronic Kerr nonlinearity

$$\delta\chi^{(1),{\rm nr}}_{ij,\rm eff}(t) = 6\,|A_{k,0}|^2\,\chi^{(3),{\rm nr}}_{ijkl}\,|u_j(t)|^2, \tag{24}$$

and where $\chi^{(3),{\rm nr}}_{ijkl} = (N/6\varepsilon_0)\langle\gamma^{\rm nr}\rangle_{ijkl}\,\delta_{k,l}$. The non-instantaneous time-domain response from the vibrational excitation is

$$\delta\chi^{(1),{\rm VR}}_{ij,\rm eff}(t) = 6\,|A_{k,0}|\,|A_{l,0}|\,T_n f_R(t), \tag{25}$$

where we have defined the forced Raman response,

$$f_R(t) = \sum_{v,m,n} f^{mn}_v(t) \tag{26}$$

as derived in appendix A.

Further, we note that the frequency domain representation of the effective linear optical susceptibility is

$$\tilde{\delta\chi}^{(1)}_{ij,\rm eff}(\omega) = \mathcal{F}\{\delta\chi^{(1)}_{\rm eff}(t)\} = 6\,|A_{k,0}|\,|A_{l,0}|\,T_n\,\tilde{F}_R(\omega). \tag{27}$$

Here we have identified the power spectral density of the forced Raman response as

$$\tilde{F}_R(\omega) = \chi^{(3),{\rm VR}}_{ijkl}(\omega)\cdot\tilde{D}(\omega - \Delta_{\rm pu}). \tag{28}$$

When the excitation pulses are at different center frequencies, the driving term, $\tilde{D}(\omega - \Delta_{\rm pu})$, shifts the excitation band of excited vibrational frequencies to a range that is centered on the beat frequency driven in the medium by the difference in the center frequency of the driving fields. The band of driven frequencies is set by the cross correlation of the spectral width.

We will make use of the impulsive approximation, which is known as impulsive stimulated Raman scattering (ISRS) [28], where we assume that we have a single pulse incident to excite the Raman-active medium so that $A_k(t) = A_l(t)$ and the incident frequencies are also the same $\omega_1 = \omega_2$, which means that $\Delta_{\rm pu} = 0$. The impulse response show in figure 1 represents the limit where the driving term, $d(t) \to \delta(t)$, is approximated by a temporal impulse; this relationship is shown in appendix A.

For the remainder of this review, we will refer to the single pump pulse that supplies both ω_1 and ω_2 (referred as the pump and Stokes frequencies, respectively) from within the bandwidth of the pump pulse as ISRS. Single pump pulse excitation also implies that $\Delta_{\rm pu} = 0$. ISRS may be driven by a transform-limited pulse or a shaped pump pulse, and will drive a sustained coherent Raman response provided that the pump pulse carries structure on the temporal intensity envelope that is shorter than vibrational period $T_v = 2\,\pi/\Omega_v$. In all cases analyzed for low frequency Raman spectroscopic detection below, we will assume ISRS excitation [69]. In many scenarios, a separate probe pulse is introduced and the Raman spectrum is deduced from spectral scattering imparted to the probe pulse by the third order polarization density [56]. Another powerful strategy uses a probe pulse that is extracted from the pump pulse with pulse shaping, and we will reserve the term single pulse Raman spectroscopy for this class of experiments [70, 71].

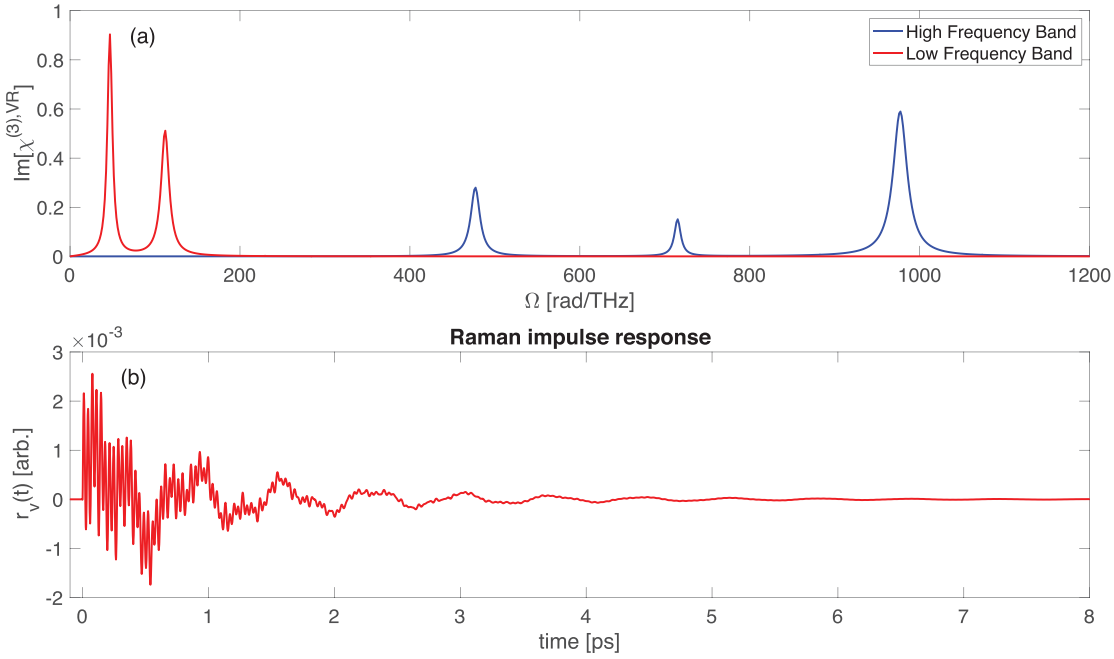

Figure 1. (a) Vibrationally resonant third order nonlinear optical susceptibility, the imaginary part of $\chi^{(3)}_{VR}(\Omega)$ is shown. (b) Raman impulse response for the vibrational spectrum in (a). The impulse response as shown in (b) is obtained from the inverse Fourier transform of the complex-valued vibrationally resonant third ororder susceptiblity, with a derivation provided in appendix A. The complex Raman susceptibility enforces causality through the relationship between the real and imaginary parts of $\chi^{(3,\mathrm{VR})}(\Omega)$ that is described by the Kramers–Kronig relations.

2.3. Forced Raman response

The forced vibrational response for each vibrational beat frequency is a convolution of the driving term $d(t)$ given by the pulse intensity envelope and the impulse response of the vibrational mode, $r_v^{mn}(t) = \Gamma_{v,mn}\, h_v^{mn}(t)$. The forced Raman response that produces the perturbation to the effective linear susceptibility in equation (25) dictates which vibrational modes are coherently excited and also determines the details of the experiments that can be established to measure the Raman spectrum. The temporal dependence of the forced Raman response depends on the particular properties of the driving fields, $A_k(t)$ and $A_l(t)$. We may consider two general cases. A common strategy in CRS is to set the $\Delta_{\mathrm{pu}} = \Omega_v$ to drive the coherent excitation of a particular vibrational frequency. This is the strategy taken with coherent anti-Stokes Raman scattering (CARS), coherent Stokes Raman scattering (CSRS), and stimulated Raman scattering (SRS). In the single pulse ISRS case, a single pulse drives forced vibrational excitation for any vibrational frequency for which the vibration frequency is within the bandwidth of the excitation pulse. Equivalently, in the time domain, the temporal duration of the exaction pulse is shorter than the vibrational period, $T_v = 2\,\pi/\Omega_v$.

Figure 2 shows a comparison of the two excitation regimes outlined above for the case of Gaussian pulses with $|u(t)|^2 = \exp(-2(t/\tau_p)^2)$, where we assume that all pulses have the same temporal duration. In the single pulse ISRS case, the driving term reads $d(t) = \sqrt{2}\exp(-2(t/\tau_p)^2)/\sqrt{\pi}\tau_p$ and the driving spectral density is $\tilde{D}(\omega) = \exp[-(\tau_p\omega/2)^2/2]$. If excitation pulse is half of the vibrational period, $\tau_p = \pi/\Omega_v$, then $\tilde{D}(\Omega_v) \sim 0.29$. We define the cutoff frequency as a vibrational mode with a period of $\tau_p = (3/4)\,T_v$ where the cutoff frequency is $\Omega_c = 3\,\pi/2\,\tau_p$ produces an excitation density of $\tilde{D}(\Omega_c) \sim 0.06$. For example, if we wish to excite a 750 cm^{-1} vibrational frequency, which has a vibrational period of $T_v \sim 44$ fs, then we require a pulse with a duration of order of ~ 20 fs or shorter to efficiently excite coherent vibrations. Here, we plot a pulse duration of $\tau_p = 42.5$ fs, which is a intensity full width half maximum (FWHM) pulse duration of $\tau_{\mathrm{FWHM}} = 50$ fs. The duration corresponds to a cutoff excitation frequency of $\Omega_c \sim 588$ cm^{-1}.

In the case with two distinct frequencies, it is conventional to call field A_k with frequency ω_2 the pump pulse, and to call the field A_l with frequency ω_1 the Stokes pulse. With the pump-Stokes pulse detuning of Δ_{pu}, and assuming no relative phase $\delta\phi_{\mathrm{pu}} = 0$, for a pair of identical Gaussian pulse envelopes, the driving term becomes, with the $d(t) = \sqrt{2}\exp(-2(t/\tau_p)^2)(1+\cos(\Delta_{\mathrm{pu}}t))/\sqrt{\pi}\tau_p$ and the driving spectral density is $\tilde{D}(\omega) = \exp[-(\tau_p\omega/2)^2/2] + \exp[-(\tau_p[\omega-\Delta_{\mathrm{pu}}]/2)^2/2]/2 + \exp[-(\tau_p[\omega+\Delta_{\mathrm{pu}}]/2)^2/2]/2$. Note that this driving term includes both the ISRS of both the pump and Stokes pulses, and the beat frequency that drives high frequency vibrational excitation over a band centered at Δ_{pu}.

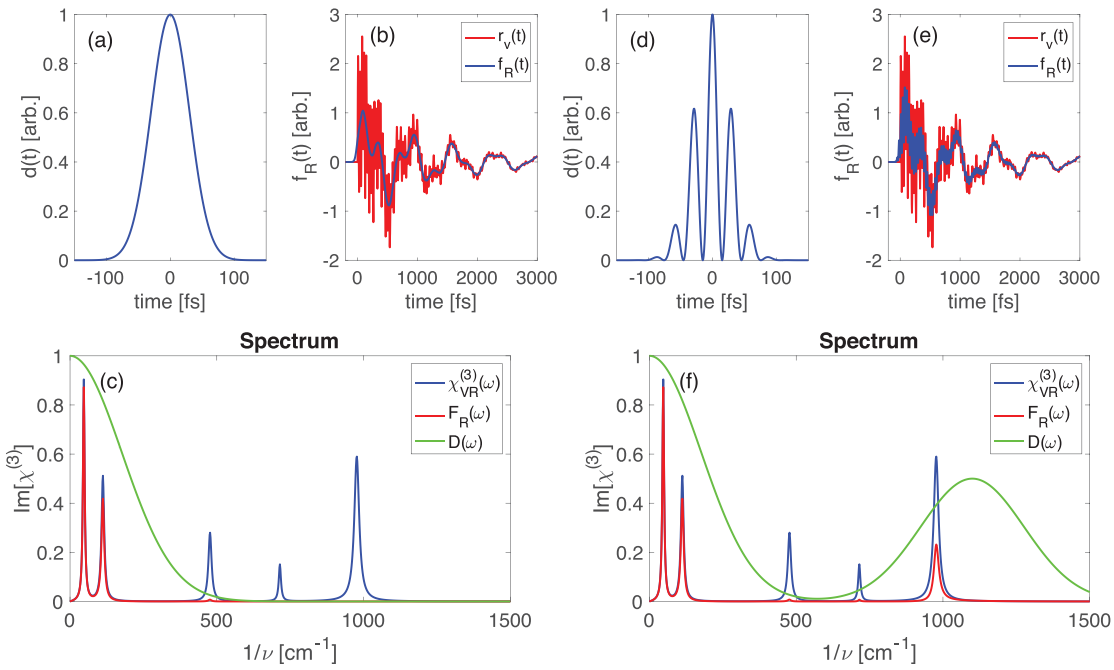

Figure 2. Forced Raman excitation driven by a single $\tau_p = 42.5$ fs pulse (a)–(c) and a pump and Stokes pulse pair with the same pulse duration, but with the Stokes field at detuned to a lower frequency by $\Delta_{pu} = 33$ THz (1100 cm^{-1}) (d)–(f). (a) ISRS driving term $d(t)$ that drives the forced Raman excitation (b) and excited the low-frequency portion of the Raman spectrum (c). When a detuned Stokes pulse is simultaneously present, the driving term $d(t)$ exhibits (d) a carrier modulation frequency of Δ_{pu} and with an envelope determined by the pulse intensity envelope, driving low and high vibrational frequencies (e) and (f). In subplots (b) and (e), the red curve is the full impulse response that would be excited by a sufficiently short pulse, and the blue curves represent the excited forced Raman response drived by the driving terms (a) and (d).

It is clear from figure 2 that pulsed excitation readily excites a low-frequency vibrational band. We may excite intermediate vibrational frequencies with a sufficiently short excitation pulse, however, in many scenarios, the dispersion management required to keep a pulse sufficiently short (and temporally clean) is quite challenging. The dual pulse strategy with a detuned center frequencies between the pulses is a simpler strategy for high vibrational frequency excitation. In the remainder of this topical review, we will focus on single pulse excited coherent scattering Raman processes, which naturally emphasizes low vibrational frequencies.

The linear shift invariant response for Raman excitation means that the excited vibrational frequencies are entirely dictated by the power spectrum of the driving term, and vibrational frequencies are driven by any temporal structure on the pulse that is shorter than a given vibrational period. By tailoring the driving pulse shape, particular vibrational modes can be preferentially excited and vibrational wavepackets can be sculpted through coherent control strategies [67, 69, 72, 73]. Additionally, this single pulse shaping can be used for specific spectral detection strategies, which we will evaluate in relevant sections below. In the simplest case, we may add quadratic spectral phase, with group delay dispersion φ_2, to a Gaussian pulse, which stretches the pulse to a duration $\tau_c = \tau_p \sqrt{1 + (2\varphi_2 \tau_p^{-2})^2}$. Chirping the pump pulse in this way is generally detrimental to the forced Raman excitation, as the power spectral density of the driving term, $\tilde{D}_c(\omega) = \exp[-(\tau_c\omega/2)^2/2]$, narrows spectrally, reducing the cutoff excitation spectrum to $\Omega_c = 3\pi/2\tau_c$. The increased pulse duration, however, will decrease the nonresonant spectral scattering, which can be beneficial for low frequency Raman spectroscopic detection [23] and which we illustrate in detail in the discussion section.

Before switching to detection strategies, we will discuss an extremely simple version of selective vibrational excitation with a single shaped pulse [67, 72]. Here, we will consider a pulse split into two identical chirped pulses. Figure 3 shows calculations for the same pulse bandwidth as in figure 2, but the pair of pulses are at the same center frequency. When a linear spectral chirp with a group delay dispersion of φ_2 stretches the duration of the pulses, each individual pulse fails to excite even the low frequency Raman spectral modes. However, the beat frequency between pair of chirped pulse drives a beat frequency given by $\Delta\omega_b = 4\varphi_2 T/(\tau_p \tau_c)^2 \approx T/\varphi_2$ for a delay between the pulse pair of T. The power spectral density of the forced Raman response driving term for spectral focusing is given by $\tilde{D}_{SF}(\omega) = \exp(-iT\omega/2)(2\tilde{D}_c(\omega)\cos(T\omega/2) + \exp(-(T/\tau_c)^2/2)[\tilde{D}_c(\omega - \Delta\omega_b) + \tilde{D}_c(\omega + \Delta\omega_b)])/4$. This strategy allows for broad bandwidth pulses to drive approximately a single vibrational frequency and goes by the name of spectral focusing. Thus

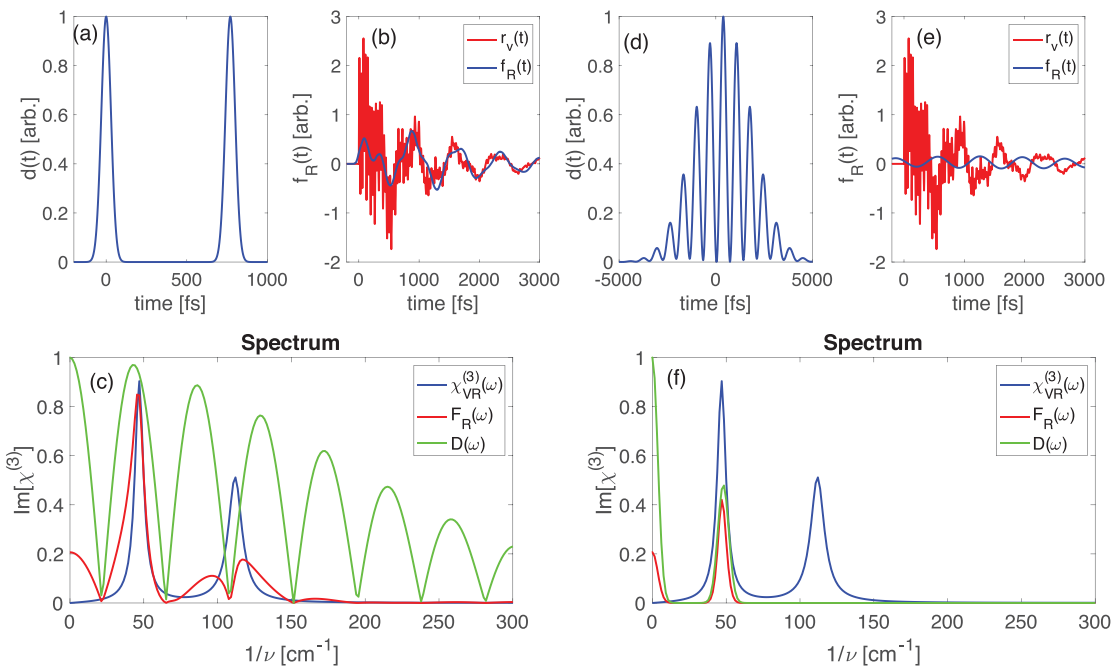

Figure 3. Forced Raman excitation driven by pairs of pulses at the same center optical frequency. For transform-limited pulse pair, (a)–(c), a periodic set of vibrational frequencies are excited (b, c). In the case of equally chirped pump and Stokes pulses (d), the driving term $d(t)$ exhibits a narrow band centered on the beat frequency, $\Delta\omega_b$. The later is directly related to the relative time delay, T, between the pump and Stokes pulses and can be easily tuned across the pump and Stokes bandwidth. In subplots (b) and (e), the red curve is the full impulse response that would be excited by a sufficiently short pulse, and the blue curves represent the excited forced Raman response drived by the driving terms (a) and (d).

by tuning the relative delay between the pump pulse pair, the excited vibrational frequency can be directly controlled.

In the remainder of this paper, we will consider forced Raman excitation in the impulsive limit where the power spectral density of the driving term, $\tilde{D}(\omega)$, is approximately constant in the neighborhood of a vibrational frequency, Ω_v, with a value of $\tilde{D}(\Omega_v)$. In the impulsive limit, $\tilde{D}(\Omega_v) = 1$, however for a finite, but approximately impulsive pulse duration, then $\tilde{D}(\Omega_v) < 1$. Earlier we noted that a Gaussian temporal pulse with the envelope $u(t) = \exp[-(t/\tau_p)^2]$, then $\tilde{D}(\Omega_v) = \exp[-(\tau_p\,\Omega_v/2)^2/2]$. As shown in appendix A, in the impulsive limit, the spectrum of the forced Raman response simplifies to

$$\tilde{F}_R(\omega) \approx \sum_{v,m,n} \chi^{(3),\mathrm{v,mn}}_{ijkl}(\Omega_{v,mn})\,\tilde{D}(\Omega_{v,mn})\,\tilde{R}^{mn}_n(\omega). \tag{29}$$

The impulsive excitation approximation simplifies the forced Raman response, to be written as

$$f_R(t) \approx \sum_{v,m,n} \chi^{(3),\mathrm{v,mn}}_{ijkl}(\Omega_{v,mn})\,\tilde{D}(\Omega_{v,mn})\,\Gamma_{v,mn}\,h^{mn}_v(t). \tag{30}$$

Thus, the relative strength of the excited vibrational modes is determined by the normalized power spectral density of the pump pulse intensity profile at the vibrational frequency.

2.4. Coherent Raman signal generation

In the remainder of this review, we will focus on the conditions under which the incident pulses admit the measurement of low frequency Raman spectra. As most relevant experiments are performed under high numerical aperture (NA) focusing conditions, the interaction lengths are short compared to the coherence length of the nonlinear interaction, and we may neglect effects such as dispersive pulse broadening during propagation. As a result, we may treat the polarization density as an invariant source term in the wave equation. Additionally, we assume the slowly varying amplitude approximation and that the integrated effect of the nonlinear wave mixing is inefficient enough that we may assume that the driving fields are constant in amplitude in the interaction region—invoking the undepleted pump approximation. In this interaction region, we may neglect the effect of phase matching and to ensure simple calculations, we consider focused beam within the interaction in a simple 'pill box' model, which is a cylinder with a length ℓ and a diameter of 2 w_0. In addition, we assume that all of the pulse envelopes are transform-limited, with a duration τ_p.

With all of these assumptions, we can consider the simple equation of motion for the field envelope, assumed to be a plane wave over the interaction region, at optical frequency ω_4 is given as

$$\frac{dA_i(z,t)}{dz} = -i\,\frac{\pi}{n_4\,\lambda_4}\,\delta\chi^{(1)}_{\rm eff}(t)\,A_j(z,t), \tag{31}$$

and $\lambda_4 = 2\,\pi\,c/\omega_4$. We are assuming the vibrational coherence excited by the driving laser pulses travels at the group velocity of those pulses, and that there is negligible difference in the group velocity, so that over the interaction length, ℓ, any relative slip between the driving pulse and pulse A_i may be safely ignored.

To perform Raman spectroscopy, we need to detect a signal that is generated by the pulse interacting with the forced Raman response. Two general scenarios arise. In this review, we will primarily look at the case where the time-dependent effective linear susceptibility perturbation drives a change to an incident probe pulse, so that $A_i = A_j \equiv A_{\rm pr}$ and $\omega_4 = \omega_3$. We will denote this field as the probe field. Under that condition, we admit solutions that perturb the plane wave field incident on the excited medium due to the time-varying phase modulation so that the probe field evolves as

$$A_{\rm pr}(z,t) = A_{\rm pr}(z)u(t)\exp\left[i\,\phi_m(t-\tau)\right]. \tag{32}$$

Here we have assumed that phase mismatch and temporal walkoff are negligible. The time-varying phase modulation reads

$$\phi_m(t-\tau) = \frac{\pi\,\ell}{n_{\rm pr}\,\lambda_{\rm pr}}\,\delta\chi^{(1)}_{\rm eff}(t-\tau), \tag{33}$$

where τ is the arrival time of the probe pulse relative to the pump pulses. Noting that the perturbation in the RI, $\delta n(t) = \delta\chi^{(1)}_{ij,\rm eff}(t)/2\,n_{\rm pr}$, and the wavenumber of the probe pulse is $k_{\rm pr} = 2\,\pi/\lambda_{\rm pr}$, the total phase modulation which be written as $\phi_m(t) = k_{\rm pr}\,\ell\,\delta n(t)$. The time-dependent phase modulation may be decomposed into the coherent Raman contribution, $\phi_R(t) = k_{\rm pr}\,\ell\,\delta n_R(t)$ and the non-resonant contribution, $\phi_{\rm nr}(t) = k_{\rm pr}\,\ell\,\delta n_{\rm nr}(t)$, where $\phi_m(t) = \phi_R(t) + \phi_{\rm nr}(t)$.

Even though these CRS signal are generated near a tight focus, we can use an approximate plane wave model for a finite interaction length, ℓ, near the focus. Some of the signal detection strategies make use of diffraction or spatial phase distortions of the incident probe field; however, given the weak phase perturbation imparted by the nonlinear interaction, these cases are quite effectively modeled with a spatially-varying phase transmission function $\phi_m(t) \to \phi_m(x,y,t)$.

It is convenient to present the laser parameters in terms of average power of the laser beams and the focus conditions. We assume that the field at the focus has a peak amplitude of $A_{j,0}$, a peak intensity of $I_{j,0}$, and a pulse duration of τ_p. For a focal beam radius of w_0, the focal length is estimated from the confocal parameter at $\ell = 2\,\pi\,w_0^2/\lambda_j$, and the cross section area is $\mathcal{A}_{\rm foc} = \pi\,w_0^2$. The beam fluence is then $U_j = \tau_p\,I_{j,0}$, and the energy per pulse is $\epsilon_j = \mathcal{A}_{\rm foc}\,U_j$. At this pulse energy for a mode-locked laser with a repetition rate of ν_R, the average power of the source is $\bar{p}_j = \nu_R\,\epsilon_j$. We may rearrange the formulae to relate the peak field strength to the average power, leading to $\left|A_{j,0}\right|^2 = 2\,\bar{p}_j/(n_i\,\varepsilon_0\,c\,\nu_R\,\tau_p\,\mathcal{A}_{\rm foc})$. For the case of a square pulse, the mean pulse time is simply the pulse duration $T_n = \tau_p$.

With these parameters in place, and assuming that the Raman response is driven by a single pump pulse, we may write the expression for the CRS contribution to the time dependent effective linear susceptibility for the plane wave propagation model as

$$\delta\chi^{(1),\rm VR}_{ij,\rm eff}(t) = \frac{12\,\bar{p}_{\rm pu,pu}}{n_{\rm pu}\,\varepsilon_0\,c\,\nu_R\,\mathcal{A}_{\rm foc}}\,f_R(t). \tag{34}$$

Now we may write the imputed phase modulation over that interaction length in terms of laser experimental parameters, giving us

$$\phi_R(t) = \frac{k_{\rm pr}\,\ell}{2\,n_{\rm pr}}\,\delta\chi^{(1),\rm VR}_{ij,\rm eff}(t) = g_{\rm pu}\,\bar{p}_{\rm pu}f_R(t). \tag{35}$$

In the impulsive limit, this expression simplifies to

$$\phi_R(t) = \sum_{\nu,m,n}\delta\phi_0^{\nu,mn}\,h_\nu^{mn}(t), \tag{36}$$

where the peak phase shift for each vibrational frequency in the impulsive limit is

$$\delta\phi_0^{\nu,mn} = g_{\rm pr,pu}\,\chi^{(3),\rm VR}_{ijlk}(\Omega_{\nu,mn})\,\Gamma_{\nu,mn}\,\tilde{D}(\Omega_{\nu,mn})\,\bar{p}_{\rm pu}, \tag{37}$$

and the factor accounting for focusing and propagation effects reads

$$g_{i,j} = \frac{12\,\pi}{n_i\, n_j\, \varepsilon_0\, c\, \nu_R\, \mathcal{A}_{\rm foc}} \left(\frac{\ell}{\lambda_j}\right). \tag{38}$$

The indices i,j will depend on which beams, pump or probe or both, drive the nonlinear interaction.

In addition to the coherent Raman response, the non-resonant response arising from the electronic Kerr nonlinearity also imparts a phase modulation. The non-resonant portion of the effective linear optical susceptibility perturbation can be written as

$$\phi_{\rm nr}(t) = \delta\phi_0^{\rm nr}\, \left|u_j(t)\right|^2 \tag{39}$$

where j can indicate either the pump or probe pulse, depending on the source of the nonresonant scattering, and we have defined the peak nonresonant phase shift of $\delta\phi_{0,j}^{\rm nr} = g_{i,j}\,\chi_{\rm nr}^{(3)}\,\tau_p^{-1}\,\bar{p}_j$.

To put these expressions into perspective, we consider some typical experimental numbers. We consider a laser pulse train producing $\tau_{\rm FWHM} = 20$ fs laser pulses at a repetition rate frequency of $\nu_R = 94$ MHz with a center wavelength of $\lambda = 1\,\mu$m. For a laser beam with average power $\bar{p} = 10$ mW focused to a beam diameter $2\,w_0 = 1\,\mu$m, the peak intensity is 800 GW cm^{-2}. With these conditions, the focal interaction parameter evaluates to $g \sim 0.17\ \times 10^8$ V^2 s m^{-2} W^{-1}. These conditions cause the pulses to drive a peak nonresonant perturbation to the RI of $\delta n_0^{\rm nr} \sim 0.011$, which leads to a peak phase shift of $\delta\phi_0^{\rm nr} = k\,\ell\,\delta n_0^{\rm nr} \sim 0.11$.

For vibrational modes, we need to consider a specific vibrational frequency. Absolute Raman scattering cross sections can be hard to come by, so we focus on the 920.5 cm^{-1} C-C stretch mode in acetonitrile for which we provided numbers earlier. We assume impulsive excitation due to the fact that the Gaussian pulse duration, $\tau_p = 17$ fs is approximately half of the vibrational mode period, $T_\nu \sim 36$ fs, leading to an ISRS excitation strength of $\tilde{D}(\Omega_\nu) \sim 0.34$. Assuming a $\Gamma_\nu = 4$ cm^{-1} linewidth, the peak amplitude of the forced Raman response is $f_\nu^{mn} \sim 7.48\ \times 10^{-9}$ m^2 V^{-2} s^{-1} for neat acertonitrile and $f_\nu^{mn} \sim 3.96\ \times 10^{-13}$ m^2 V^{-2} s^{-1} at a 1 mM concentration. This forced Raman response produces a perturbation in the RI of $\delta n_0^{\rm VR} \sim 0.0013$ and $\delta n_0^{\rm VR} \sim 6.84\ \times 10^{-8}$, leading to peak accumulated phase shifts of $\delta\phi_0^{\rm VR} \sim 0.013$ radians and $\delta\phi_0^{\rm VR} \sim 0.684\,\mu$radians, respectively for neat and 1 mM concentrations.

3. Coherent Raman spectral scattering

When a probe pulse propagates through the time-varying optical susceptibility perturbation that is established by the pump pulse, the probe pulse accumulates temporal phase modulation determined by equation (35). This phase modulation is imparted to a probe pulse that arrives at a time delay of τ after the pump pulse, equation (32), and we may write the modulated probe pulse as

$$A_{\rm pr}(t) = A_{\rm pr} u_{\rm pr}(t) e^{i\,\delta\phi_{nr}(t)}\, e^{i\,\delta\phi_R(t-\tau)}. \tag{40}$$

For the sake of clarity, we will consider one excited vibrational mode at frequency Ω_ν, however, the results are readily generalized to multiple excited vibrational modes. Moreover, as we are considering a short interaction length of a focused beam, the dispersion accumulated by the pulse is too low to change the pulse duration, so we assume that the temporal pulse shape remains unchanged through the focus. Further assuming that the unperturbed pulse is transform-limited at the focus, we are in a position to compute the effects of scattering of the pulse.

The nonresonant transient phase will also phase modulate the pulse, modifying the spectrum. The peak nonresonant phase shift is a small parameter, so it follows that we may estimate the modulated pulse as

$$u_{\rm ph}(t) \approx u_{\rm pr}(t) + i\,\delta\phi_0^{\rm nr}\, \left|u_{\rm pr}(t)\right|^2\, u_{\rm pr}(t). \tag{41}$$

The spectrum of the self phase modulated probe pulse follows from use of the Fourier transform, leading to

$$U_{\rm ph}(\Omega) \approx U_{\rm pr}(\Omega) + i\,\delta\phi_0^{\rm nr}\, U_b(\Omega). \tag{42}$$

In this weak phase perturbation limit, this broadened spectrum, $U_b(\Omega)$, of this pulse is the spectrum of the probe temporal envelope, $U_{\rm pr}(\Omega) = \mathcal{F}\{u_{\rm pr}(t)\}$, that is convolved with the spectrum of the pulse intensity, $\mathcal{F}\{|u_{\rm pr}(t)|^2\} = U_{\rm pr}(\Omega) \star U_{\rm pr}(\Omega)$. Thus, the full expression for the spectrum broadened by non-resonant phase modulation is given by $U_b(\Omega) = U_{\rm pr}(\Omega) * \{U_{\rm pr}(\Omega) \star U_{\rm pr}(\Omega)\}$. Here, $*$ and $\star$ denote the convolution and correlation operators, respectively.

First, we illustrate the time-dependent phase modulation that produces conventional CRS with long pulses used for CARS, CSRS, and SRS processes. In these methods, two pulses with distinct center

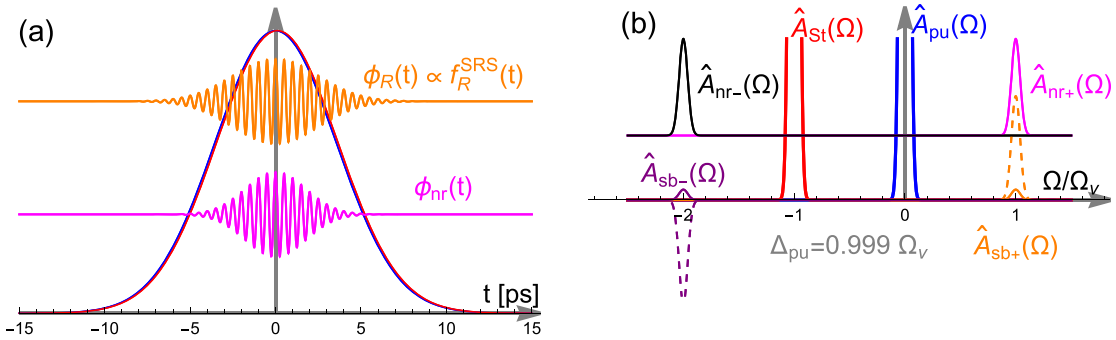

Figure 4. Spectral scattering driven by a pair of detuned pump and Stokes fields. (a) The envelopes of the pump (blue) and Stokes (red) fields are overlapped in time. The phase modulation from the forced Raman response (orange) oscillates at the frequency detuning, $\Delta_{pu} = 0.999\,\Omega_v$. The phase modulation from the nonresonant response (magenta) follows the envelope of the interfence between the pump and Stokes pulses that oscaillates at the frequency Δ_{rm}. (b) The spectral scattering induced by the phase modulation scatters some of the pulse energy to higher frequencies, anti-Stokes (AS), and lower frequencies, Stokes (S), to sidebands separated by Δ_{pu}. The nonresonant scattered spectra (magenta and black) are purely real. By contrast the spectra generated by CRS are complex because $\chi^{(3),VR}_{ijkl}(\Omega_v - \Delta_{pu})$ is complex. As a result, the CRS spectral content contains both real (solid) and imaginary (dashed) components in the anti-Stokes (orange) and Stokes (purple) scattered spectra. Interference between these scattered spectra dictate the optically detectable spectroscopic signals.

frequencies detuned to Δ_{pu}, result in the driving term, $\tilde{D}(\omega - \Delta_{pu})$. In CARS, CSRS, and SRS long pulses (several ps) are used and thus the PSD of the driving term is constant across narrow spectral width of the pulses, from which we compute a forced Raman response of

$$f_R^{SRS}(t) = d(t)\,\mathrm{Im}\{\chi^{(3),VR}_{ijkl}(\Omega_v - \Delta_{pu})\,\exp(i\Delta_{pu}\,t)\}. \tag{43}$$

The forced Raman response for this case is shown in figure 4(a) driven by a pump and Stokes pulse pair detuned to slightly below the resonance frequency to illustrate the complex amplitude of the field scattered to sidebands (sb±). The oscillating orange curve in figure 4(a), which has been offset for clarity, is the phase modulation driven by the forced Raman response established by the beat frequency between the pump and Stokes fields. The phase modulation of the pump pulse scatters energy from the pump pulse to spectral sidebands at $\Omega_{sc\pm} = \Omega_{pu} \pm (\Omega_v - \Delta_{pu})$. Scattering from the pump spectrum to the frequency higher scattered frequency, $\Omega_{sc+} = \Omega_{pu} + (\Omega_v - \Delta_{pu})$, populates the positive sideband, $\hat{A}_{sb+}(\Omega)$, which is the CARS spectrum. The field scattered to a lower frequency, $\Omega_{sc-} = \Omega_{pu} - (\Omega_v - \Delta_{pu})$, interferes with the input Stokes spectrum, and is the source of Stimulated Raman gain in SRS for the Stokes pulse. Similarly, spectrum is scattered from the Stokes field to the scattered frequencies $\Omega_{sc\pm} = \Omega_{St} \pm (\Omega_v - \Delta_{pu})$. Here, the positive scattered frequency, $\Omega_{sc+} = \Omega_{St} = (\Omega_v - \Delta_{pu})$, interferes with the input pump spectrum, serving as the is the source of Stimulated Raman loss in SRS for the pump pulse. Finally, the scattering form the Stokes spectrum to the lower frequency, $\Omega_{sc-} = \Omega_{St} - (\Omega_v - \Delta_{pu})$, is the CSRS spectrum that populates the the negative CSRS spectral sideband, $\hat{A}_{sb-}(\Omega)$. These spectral sidebands are shown in figure 4(b), where the solid and dashed lines indicate the real and imaginary components of the spectral sidebands, respectively. The magenta curves in figure 4(a) is the nonresonant phase modulation that produces the nonresonant spectral sidebands at ±nr indicated in figure 4(b). The nonresonant sidebands are purely real as denoted by the solid magenta line. Notice also that the real parts of the sideband scattering have opposite sign, which is the origin of stimulated Raman gain and loss.

In the ISRS limit, and for a single vibrational excited mode, the forced sinusoidal Raman phase modulation centered at the time delay τ becomes

$$\phi_R(t-\tau) = \delta\phi_0^v\, e^{-\frac{1}{2}\Gamma_v(t-\tau)}\,\sin(\Omega_v[t-\tau]), \tag{44}$$

and which is illustrated in figure 5(a). The nonresonant phase modulation is applied directly to the pump pulse as self phase modulated, equation (41), is illustrated by the solid magenta curve in figure 5(a).

The spectral scattering imparted to a time-delayed probe pulse can be computed by making use of the Jacobi–Anger expansion and truncating to first order expansion terms, we may write the spectrum of the probe pulse as

$$\hat{A}_{pr}(\Omega) = A_{pr}\left[a_0\,U_{pr}(\Omega) + \hat{A}_{nr}(\Omega) + \hat{A}_{sb+}(\Omega) + \hat{A}_{sb-}(\Omega)\right], \tag{45}$$

where the scattered spectral sidebands are $\hat{A}_{sb\pm}(\Omega) = \mp a_\tau^v\,U_{pr}(\Omega \mp \Omega_v)$ and we have introduced the coefficients $a_0 = J_0(z_s)J_0(z_c)$, $a_\tau^v = J_0(z_c)J_1(z_s) + iJ_0(z_s)J_1(z_c)$, where J_n is the nth order Bessel function of the

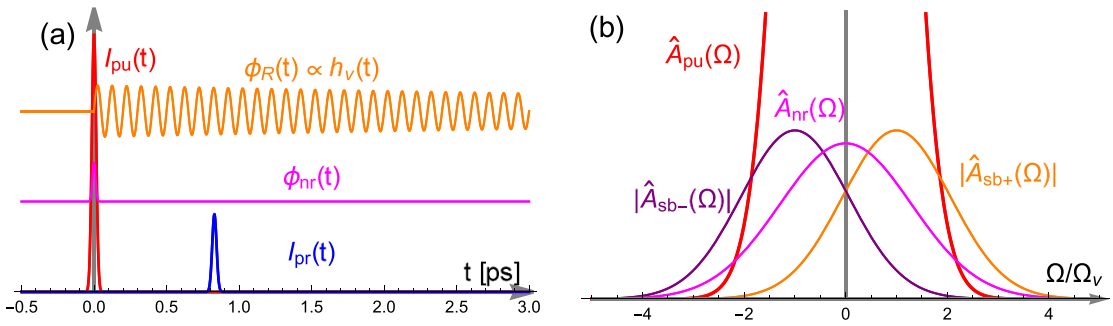

Figure 5. Spectral scattering imparted to a short probe pulse due to impulsive Raman excitation by a short pump pulse. (a) The pump pulse (red) excited a time-varying impulsive forced Raman response (orange) that imparts spectral scattering to a time-delayed probe pulse (blue) that arrives in the excited medium at a delay τ after the pump pulse. Nonresonant scattering (magenta) is assumed to be dominated by the pump pulse because the probe pulse is substantially weaker, except when the pump and probe pulses overlap in time when the pump pulse drives a cross phase modulation process. (b) Some of the incident probe pulse energy is scattered to Stokes (purple, $\hat{A}_{sb-}(\Omega)$) and to anti-Stokes (orange, $\hat{A}_{sb+}(\Omega)$) spectral sidebands. Only the magnitude of the scattered S (purple) and AS (orange) sidebands are displayed, and the impact of the complex magnitudes will be discussed below. The nonresonant spectral scattering magnitude (magenta) is purely imaginary.

first kind, and the delay-dependent phase modulation depth coefficients are $z_s = \delta\phi_0^v \exp(-\Gamma_v\tau/2)\cos\phi_\tau$ and $z_c = \delta\phi_0^v \exp(-\Gamma_v\tau/2)\sin\phi_\tau$, where we have defined a vibrational phase delay as $\phi_\tau = \Omega_v\tau$. The nonresonant spectral scattering is given by $\hat{A}_{nr}(\Omega) = i a_0\,\delta\phi_0^{nr}\,U_b(\Omega)$.

An example of spectral scattering of a time-delayed short probe pulse due to impulsive excitation by a short pump pulse is illustrated in figure 5. The magnitude of the spectral sidebands, denoted by subscript sb, are shown in figure 5(b), where the sb+ is the portion of the probe spectrum scattered to a frequency increased by the vibrational frequency and the sb− has been shifted down in frequency by the same amount. The complex amplitude of these sidebands, a_τ, evolves with pump-probe delay τ and leads to a reshaping of the probe pulse spectrum, as is discussed in more detail below. Note that with a short probe, no spectra may be resolved at a particular pump-probe time delay τ. Spectral resolution at a fixed delay is possible with a long probe pulse. This is illustrated in figure 6.

For the sake of computing signal and noise models, we will employ a Gaussian pulse with a temporal envelope given by $u(t) = \exp[-(t/\tau_p)^2]$ and a corresponding spectral envelope of $U(\Omega) = \sqrt{\pi}\,\tau_p \exp[-(\tau_p\,\Omega/2)^2]$. It follows that the pulse scattered by nonresonant broadening follows a temporal envelope of $u_b(t) = \exp[-3(t/\tau_p)^2]$ with a corresponding spectral envelope of $U_b(\Omega) = \sqrt{\pi/3}\,\tau_p \exp[-(\tau_p\,\Omega/2)^2/3]$. The spectral scattering from the coherent forced Raman response retains the spectral field distribution, but are centered on the vibrational frequency, so that for the Gaussian model, we use $U_R(\Omega) = \sqrt{\pi}\,\tau_p \exp[-(\tau_p\,[\Omega \pm \Omega_v]/2)^2]$.

Many coherent Raman detection strategies rely on the detection of the filtered spectral power. To that end, we may write the power spectrum of the probe pulse. Expanding the terms gives us a power spectral density of the form

$$S_{mod}(\Omega) = S_{sb}(\Omega) + S_{sh}(\Omega) + S_i(\Omega) - S_{2i}(\Omega). \tag{46}$$

The sideband spectrum, $S_{sb}(\Omega)$, is given by the spectrum of each independent term,

$$S_{sb}(\Omega) = |a_0|^2\,S_{pr}(\Omega) + |a_0\,\delta\phi_0^{nr}|^2\,S_b(\Omega) + |a_\tau|^2\,S_{pr}(\Omega-\Omega_v) + |a_\tau|^2\,S_{pr}(\Omega+\Omega_v), \tag{47}$$

where the power spectral density for the probe and self phase modulated pulse are $S_{pr} = |U_{pr}(\Omega)|^2$ and $S_b = |U_b(\Omega)|^2$, respectively.

When the probe pulse is both distinct (that is it can be separated from the pump pulse either spectrally, with polarisation, or propagation direction) from the input pulse and the pulse is long enough to span many vibrational periods, as illustrated in figure 6(a), then the spectral sidebands $\hat{A}_{\pm sb}(\Omega)$ do not overlap with the input probe pulse spectrum, the Raman spectrum can be obtained directed from the measured probe pulse spectrum, as shown in figure 6(b).

The remaining power spectral density terms arise from interference between the spectral field sidebands. The first-order interference of the Raman-scattered sidebands and the depleted input probe spectrum reads

$$S_{sh}(\Omega) = 2\,a_0\,\left(\mathrm{Re}\{a_\tau\,U_{pr}^*(\Omega)\,U_{pr}(\Omega+\Omega_v)\} - \mathrm{Re}\{a_\tau\,U_{pr}^*(\Omega)\,U_{pr}(\Omega-\Omega_v)\}\right), \tag{48}$$

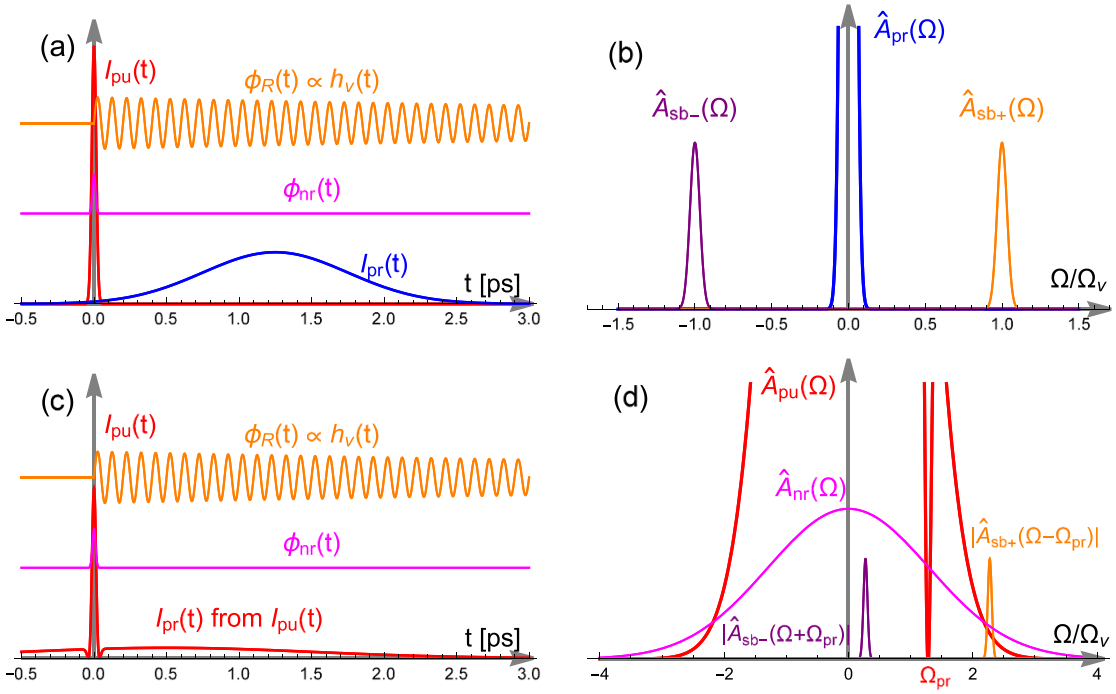

Figure 6. Spectral scattering imparted to a long probe pulse due to impulsive Raman excitation by a short pump pulse. (a) A pump pulse (red) excites a forced Raman response that produces a time-varying phase modulation (orange). The pump pulse also experiences nonresonant phase modulation (magenta). The probe pulse (blue) is time delayed from the pump pulse, and has a low enough peak intensity that the nonresonant phase modulation may be neglected. (b) The long probe pulse has a relatively narrow spectrum, so that the positive (sb+, orange, anti-Stokes) and negative (sb−, purple, Stokes) spectral sidebands directly display the Raman spectrum. (c) Spectral resolution in CRS may also be obtained by shaping the pump pulse to produce a long probe pulse (red). The temporally narrow region of the pump pulse near time zero produces impulsive excitation in the medium, leading to a time-dependent phase modulation from the forced Raman response (orange). This narrow intense pump pulse region also experiences nonresonant phase modulation (magenta), which plays a critical role in Raman spectral detection. The probe pulse obtained from the pump pulse is shown as the temporally stretched, low intensity portion of the pump pulse (also in red). (d) The magnitude of the pump pulse spectrum (red) is saturated to show the notch removed from the spectrum that produces the probe pulse that is centered at a frequency Ω_{pr}. The nonresonant scattered spectrum (magenta) is able to interfere with both the input pulse spectrum and the spectral sidebands (orange, sb+, purple sb−). The magnitude of these sidebands are shown here for clarity in the figure, but specific experimental configurations will be discussed later that exploit interference for sensitive Raman detection.

whereas the interference spectrum, $S_i(\Omega)$, between the remaining input probe spectral field and the field scattered into the broadened self phase modulation (SPM) spectrum is given by

$$S_i(\Omega) = 2\,|a_0|^2\,\delta\phi_0^{nr}\,\mathrm{Im}\{a_\tau\,U_{pr}(\Omega)\,U_b^*(\Omega)\}. \tag{49}$$

Due to the weak magnitude of the phase, the following second order terms may generally be neglected, but for completeness, we present them here. The second order spectral sideband interference gives the term

$$S_{2,sh}(\Omega) = |a_\tau|^2\,\left[U_{pr}^*(\Omega-\Omega_v)\,U_{pr}(\Omega+\Omega_v) + U_{pr}(\Omega-\Omega_v)\,U_{pr}^*(\Omega+\Omega_v)\right], \tag{50}$$

and the interference spectrum, $S_{2i}(\Omega)$, between the self phase modulation spectrum and the Raman sidebands reads

$$S_{2i}(\Omega) = 2\,a_0\,\delta\phi_0^{nr}\,\mathrm{Im}\{a_\tau^*\,U_b(\Omega)\,U_{pr}^*(\Omega-\Omega_v) + a_\tau\,U_b^*(\Omega)\,U_{pr}(\Omega+\Omega_v)\}. \tag{51}$$

Finally, we note that for the common case where the probe pulse is unchirped, the two interference terms vanish, i.e. $S_i(\Omega) = 0$ and $S_{2i}(\Omega) = 0$.

Interference between the sideband spectra, the pump pulse spectrum, and the nonresonant scattered spectrum occurs primarily for two cases. The first case is when we have a short probe pulse with a spectral width larger than the vibrational frequency (figure 5(b)). The complex amplitudes of the scattered sideband spectra evolves with a change of pump-probe delay—producing a modulation of the spectrum that is discussed in the next section. The second case is illustrated in figure 6(d) where a spectrally narrow, temporally long probe pulse is extracted from the short input pump pulse and the scattered sidebands can interfere with the remainder of the pump pulse spectrum and with the nonresonant scattering.

While the details of the detected signal depend on the experimental arrangement and the vibrational frequency, we can get an estimate of the power scattered by the time-dependent phase modulation imparted by the nonresonant and vibrationally resonant excitations. The total power scattered by the nonresonant scattering process is $\bar{p}_{\rm nr} = (\delta\phi_0^{\rm nr})^2\,\bar{p}_j$, where j may denote either the pump or probe pulse. For the Gaussian model, the nonresonantly scattered pulse energy, $\mathcal{E}_{\rm nr} = \bar{p}_{\rm nr}/\nu_R$, is distributed across the spectral amplitude of a broadened spectral amplitude $\hat{U}_b(\Omega)$. For the example experimental parameters discussed here, the fraction of the pump or probe power that is scattered by the nonresonant response is $(\delta\phi_0^{\rm nr})^2 \sim 1.1$ %, so that the 10 mW average power scatters to a power of $\bar{p}_{\rm nr} \sim 111\,\mu$W and a pulse energy of $\mathcal{E}_{\rm nr} \sim 1.18$ pJ.

The power and energy of the scattered coherent forced Raman response depends on the strength of the excited vibrational coherence and the interaction length. Typically in coherent Raman spectroscopy, the phase modulation imparted by the Raman excitation is weak. In this limit, we may approximate the CRS as producing only two sidebands at the Stokes and anti-Stokes frequencies. This allows us to approximate the scattering amplitudes defined above as $a_0 = J_0(z_s)\,J_0(z_c) \approx 1$ and $a_\tau^\nu \approx (\delta\phi_0^\nu/2)\,\exp(-\Gamma_\nu\tau/2)\,\exp(i\phi_\tau)$. The power scattered to a single sideband by the CRS scattering process is $\bar{p}_{\rm CRS} = (\delta\phi_0^\nu/2)^2\,\bar{p}_{\rm pr}$ is only ~ 0.016 % for neat acetonitrile for our example experimental conditions. The fraction of scattered power corresponds to an average probe power scattered to each sideband of $\bar{p}_{\rm CRS} \sim 1.63\ \mu$W and a pulse energy of $\mathcal{E}_{\rm CRS} \sim 0.017$ fJ. For a 1mM concentration of acetonitrile, these numbers plummet to $\bar{p}_{\rm CRS} \sim 4.46$ fW and a pulse energy of $\mathcal{E}_{\rm CRS} \sim 4.85\ \times 10^{-11}$ fJ.

The extremely low levels of power scattered by the excited forced Raman response mean that for all but the highest concentrations and largest Raman cross sections, the field scattered by the Raman response needs to be interfered with either the input probe or pump pulse field, or the nonresonantly broadened field to exploit homodyne amplification to make the signal detectable. In the next section, practical mechanisms for signal enhancement and detection are discussed and quantitatively compared.

3.1. Frequency shifting of the probe pulse

The time-varying susceptibility imparts a phase modulation to an impulsive time-delayed pulse that is centered at the pump-probe delay τ. As the pulse duration, τ_p, is substantially shorter than the vibrational period of the vibrations, the phase modulation can be approximated by a first-order Taylor expansion, which reads

$$\delta\phi_R(t-\tau) \approx \delta\phi_0\,e^{-\Gamma_\nu\tau/2}\left\{\sin(\Omega_\nu\tau) + \Omega_\nu\cos(\Omega_\nu\tau)\,[t-\tau]\right\}. \tag{52}$$

The linearized phase modulation about the center of the probe pulse may more compactly be written as

$$\delta\phi_R(t-\tau) \approx \delta\phi_R(\tau) + \delta\omega_R(\tau)\,(t-\tau) \tag{53}$$

where we write the Raman-induced phase shift at the delay τ in the form

$$\delta\phi_R(\tau) = \delta\phi_0\,e^{-\Gamma_\nu\tau/2}\,\sin(\Omega_\nu\tau) \tag{54}$$

and the delay-dependent frequency shift as

$$\delta\omega_R(\tau) = -\delta\omega_0\,e^{-\Gamma_\nu\tau/2}\,\cos(\Omega_\nu\tau) \tag{55}$$

and we have identified the peak frequency shift at zero delay, $\tau = 0$, as $\delta\omega_0 = \Omega_\nu\delta\phi_0$.

While this analysis offers a simple approach to illustrating the frequency shift, more physical insight is obtained by analysing the interference of the terms that arise in the power spectrum of the probe pulse that has propagated through the medium in which a Raman coherence has been excited. The shift in the centroid of the probe pulse spectrum is computed with the first spectral moment, defined as $\langle\Omega\rangle \equiv \langle\Omega\,S_{\rm mod}(\Omega)\rangle$. Because the spectra are shifted symmetrically by the vibrational frequency, and for an unchirped spectrum, the only non-vanishing term is

$$\langle\Omega\rangle = \langle\Omega\,S_{\rm sh}(\Omega)\rangle = -2\,f_{\delta\omega}\,a_0\,{\rm Re}\{a_\tau\}\,\Omega_\nu \tag{56}$$

where the spectral overlap factor $f_{\delta\omega}$ has a functional form that is determined by the field spectral distribution. In the weak scattering limit, i.e. $\delta\phi_0 \ll 1$, in which our derivation is valid, then $2a_0\,{\rm Re}\{a_\tau\} \approx \delta\omega_0\,e^{-\Gamma_\nu\tau/2}\,\cos(\Omega_\nu\tau)$, then we find that

$$\langle\Omega\rangle = -f_{\delta\omega}\,\delta\omega_0\,e^{-\Gamma_\nu\tau/2}\,\cos(\Omega_\nu\tau). \tag{57}$$

We see that the delay dependent frequency shift of the probe pulse clearly arises from interference between the unshifted probe pulse field spectrum and the spectral sidebands. Further insight can be gleaned by

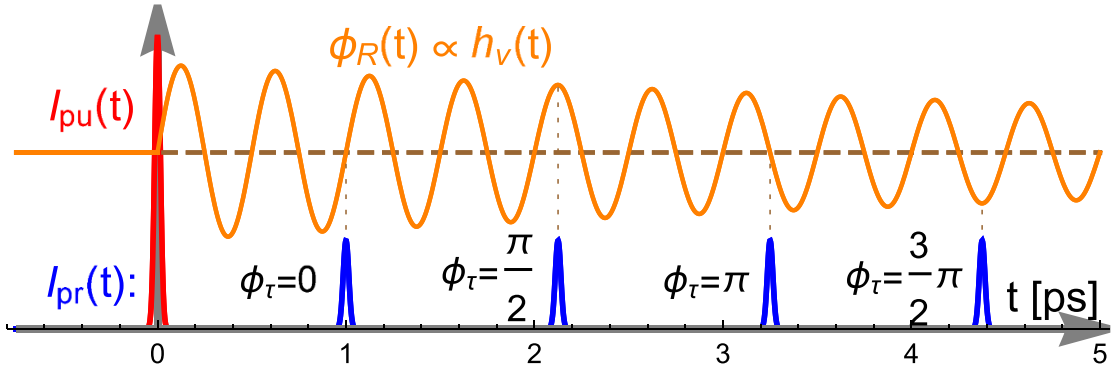

Figure 7. Role of interference between the incident probe pulse spectrum and scattering to spectral sidebands. We consider impulsive excitation by the pump pulse (red), followed by the probe pulse (blue) delayed by four different times so that the vibrational phase, $\phi\tau = \{0, 1/2, 1, 3/2\}\,\pi$ at our example probe pulse time delays. These time-delays are chosen to illustrate the interference process that produces a varying shift in the probe pulse power spectral density center of mass (COM) as a function of probe pulse delay τ that are shown in figure 8.

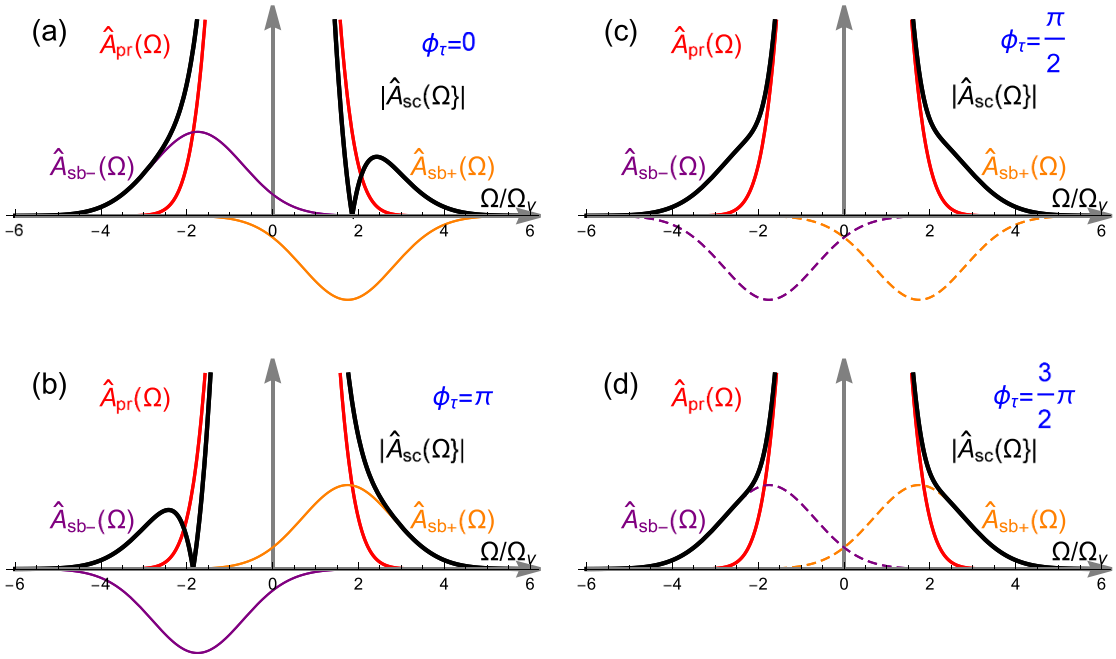

Figure 8. Examples of spectral sideband interference that depend on the vibrational phase $\phi_\tau = \Omega_v \tau$. (a), (b) For $\mathrm{mod}_{2\,\pi}[\phi_\tau] = \{0, \pi\}$, the scattered sidebands are purely real and directly interfere with incident probe pulse spectrum. (a) When $\mathrm{mod}_{2\,\pi}[\phi_\tau] = 0$, the positive sideband is negative valued, whereas the the negative sideband is positive valued—producing a spectral center of mass shift to positive values: $\langle\Omega\rangle > 0$. (b) At $\mathrm{mod}_{2\,\pi}[\phi_\tau] = \pi$, the signs of the sidebands reverse, leading to $\langle\Omega\rangle < 0$. (c), (d) By contrast, at time delays that produce $\mathrm{mod}_{2\,\pi}[\phi_\tau] = \{\pi/2, 3\,\pi/2\}$, the sidebands are completely imaginary, preventing interference so that all three spectral distributions add in quadrature—producing symmetric spectral broadening and $\langle\Omega\rangle = 0$. All other time delays drive spectral scattered sidebands that are complex, leading to an intermediate shift in the spectral center of mass.

considering a model for a Gaussian probe pulse given by $u_{\mathrm{pr}} = \exp(-(t/\tau_p)^2)$. The spectral overlap function for this Gaussian pulse model is $f_{\delta\omega} = \exp(-(\tau_p\,\Omega_v)^2/8)$. This overlap function quantifies the decrease in the overlap of the interference between the sidebands and the input probe spectrum. The vibrational frequency and vanishes when the vibrational period becomes sufficiently shorter than the probe pulse duration. We see that in the Gaussian pulse model that the interference overlap function takes the same form as the ISRS excitation efficiency. The spectral shifting is illustrated in figures 7 and 8.

Continuing with our example numbers, we find that the simple model based on a Taylor expansion of the local phase modulation from the forced Raman response gives a frequency shift of $\Omega_v/2\,\pi \sim 353$ GHz and $\Omega_v/2\,\pi \sim 18.6$ MHz for neat and 1 mM of acetonitrile, respectively. With the full model that accounts for the spectral overlap model, the estimated frequency shifts drop to $\Omega_v/2\,\pi \sim 119$ GHz and $\Omega_v/2\,\pi \sim 6.30$ MHz for neat and 1 mM of acetonitrile, respectively.

3.2. Scattering of the probe pulse to distinct new frequencies

When the probe pulse temporal duration is long compared to the vibrational period of the excited vibrational coherence, the interference of between the sidebands and the input probe pulse spectrum vanishes, leading to a considerably simplified transmitted probe power spectrum given by

$$S_{\mathrm{mod}}(\Omega) = |a_0|^2\, S_{\mathrm{ph}}(\Omega) + |a_\tau|^2\, S_{\mathrm{ph}}(\Omega - \Omega_v) + |a_\tau|^2\, S_{\mathrm{ph}}(\Omega + \Omega_v). \tag{58}$$

Under these conditions, the nonlinear Raman scattering generates a well-separated frequency from incident probe pulse as shown in figure 6(b). The un-shifted spectral term is a stimulated Raman scattering (SRS) term that is detected by recording the power in that unshifted spectrum. While the upshifted and downshifted spectral sidebands are the anti-Stokes and Stokes frequencies, respectively. We assume that the probe pulse arrives after the impulsive pump pulse, and the self phase modulation is weak so that it is likely that $U_{\mathrm{ph}}(\Omega) \approx U_{\mathrm{pr}}(\Omega)$. Note that for impulsive excitation followed by a long probe pulse, when multiple frequencies are present, there will be a sum of sideband terms that will report the spectrum of the impulsively excited vibrational modes.

The scattered power in the sidebands is independent of the pump-probe delay, except for the exponential decay due to dephasing and population decay. The un-shifted term has an amplitude of $|a_0|^2 = J_0^2(z_s) J_0^2(z_c) \approx 1 - (\delta\phi_0\ \exp(-\Gamma_v \tau/2))^2/2$, whereas the sideband amplitudes are given by $|a_\tau|^2 = J_0^2(z_c) J_1^2(z_s) + J_0^2(z_s) J_1^2(z_c) \approx (\delta\phi_0\ \exp(-\Gamma_v \tau/2))^2/4$.

In the case of a short probe pulse, spectral broadening from self phase modulation will spectrally overlap with the spectrally shifted sidebands. While the sidebands and the phase modulated probe pulse will still likely overlap with the input probe spectrum, it is common to clip the high-frequency side of the spectrum to enable isolated detection of new spectral components for detection of a coherent anti-Stokes Raman scattering (CARS) signal. While an identical signal can be collected from the low-frequency side of the spectrum to record a coherent Stokes Raman scattering (CSRS) signal, this is less common due to the possibility of corruption of the signal from fluorescent light emission.

Consider a CARS scenario where we are able to cleanly separate only probe frequencies that have been scattered to frequencies outside of the input (clipped) probe pulse spectrum, which can be accomplished with a modification of the pump (red) spectrum in figure 6(d), and is illustrated in figure 9(f). In this experimental configuration, we only retain two of the terms in equation (45), and the isolated high-frequency content of the probe pulse spectrum is then

$$\hat{A}_{\mathrm{high}}(\Omega) = A_{\mathrm{pr}} \left[i a_0\, \delta\phi_0^{\mathrm{nr}}\, U_b(\Omega) - a_\tau^v\, U_{\mathrm{pr}}(\Omega - \Omega_v) \right]. \tag{59}$$

By noting that in weak probe phase limit, $a_\tau \approx \delta\phi_0^v \exp(-\Gamma_v \tau/2) \exp(i\Omega_v \tau)/2$, we see that we obtain the more conventional form for the spectrum that is scattered to high frequencies,

$$\hat{A}_{\mathrm{high}}(\Omega) = A_{\mathrm{pr}}\, U_{\mathrm{pr}}(\Omega) * \left[\tilde{\phi}_{\mathrm{nr}}(\Omega) + \tilde{\phi}_R(\Omega) \right]. \tag{60}$$

The spectra of the phase modulation terms are $\tilde{\phi}_R(\Omega) = g_{\mathrm{pr,pu}}\, \bar{p}_{\mathrm{pu}}\, \tilde{F}_R(\Omega)$, for $\Omega > 0$, and $\tilde{\phi}_{\mathrm{nr}}(\Omega) = \delta\phi_0^{\mathrm{nr}} \left\{ U_{\mathrm{pr}}(\Omega) \star U_{\mathrm{pr}}(\Omega) \right\}$, and where we $\tilde{F}_R(\Omega)$ is the forced Raman response defined earlier in equation (29).

4. Low frequency CRS signal-to-noise models

In order to compare various CRS methods, we will consider the signal and noise limits for two forms of ISRS: time domain measurements and frequency domain measurements. In the case of time-domain measurements, we will consider the signal that is collected on a single-element detector such as a photodiode. Detected signals will seek to observe either changes in the effective RI or a shift in the center frequency of a probe pulse. To obtain a spectrum from a time domain measurement requires scanning of the pump-probe pulse relative time delay, τ. In frequency domain measurements, the signal spectrum will be resolved spatially with a spectrometer and generally be recorded with an array detector. In all cases, we will evaluate the signal-to-noise ratio (SNR) that limits CRS signal detection. A detailed presentation of noise processes in CRS measurements is provided in [74].

The dominant noise process that limits the SNR depends on the average incident power on the detector and the noise properties of the laser source. For each ISRS CRS method discussed here, typical signal power levels are computed for our example experimental parameters, and the relevant noise limits will be analyzed. Because the signal power scales with the concentration of the target analyte, the dominant noise process depend on the concentration of the analyte. At low power levels, the SNR is dominated by Johnson noise, and the SNR scales linearly with optical power. At higher power levels, the noise contributions are dominated

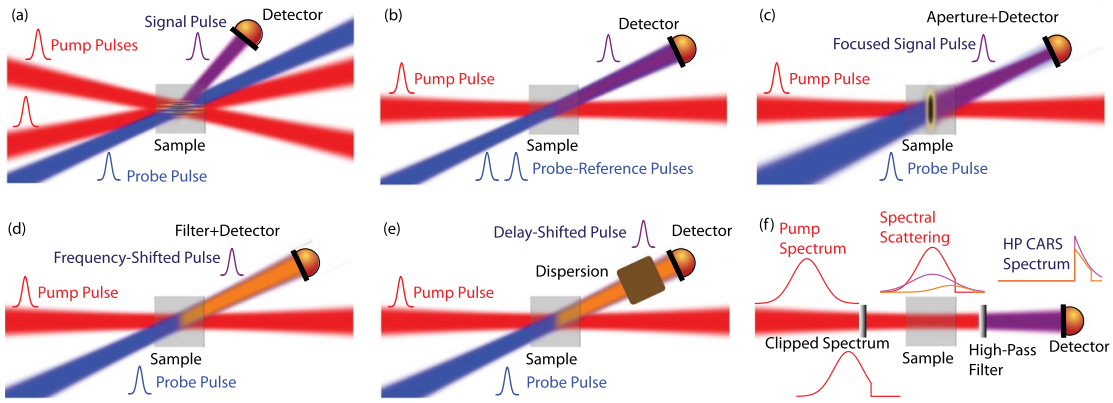

Figure 9. Experimental configurations for time-domain ISRS spectroscopy that is obtained by recording a signal as a function of relative arrival time, τ, of the probe pulse following the pump pulse. (a) In Transient grating (TG), two pump pulses arrive simultaneously and produce a phase grating due to the forced Raman response that persists for some time until the arrival of the probe pulse at a time-delay τ. The probe pulse is diffracted by the transient phase grating to a unique spatial location where the power of the diffracted signal is recorded. (b) In interferometric methods (INT), the phase perturbation, $\delta\phi_m(\tau)$, acquired by the probe pulse as a function of pump-probe delay τ as illustrated in figure 5(a) can be converted into a modulation in detected power by the introduction of a reference field that is also referred to as a local oscillator. (c) The spatial variation of the focused pump pulse produces a forced Raman response that acquires the spatial profile of the pump intensity—leading to a spatial variation in phase modulation imparted by the forced Raman response. For a probe pulse propagating on axis with the pump, the spatial variation in the coherent Raman phase acts as a weak Kerr lens (KL), and the lensing effect can be converted into a change in power transmission with an aperture placed in the probe beam. If the probe and pump beams are slightly displaced, the probe beam will sample the phase gradient from the edge of the spatial variation in the phase perturbation induced by the pump pulse. This will lead to Kerr steering (KS) that can be converted into a signal power change with a knife edge in the probe beam. (d) Frequency shifting ($\delta\omega$) makes use of the change in the probe power spectral density center of mass. A spectral edge filter can be used to convert the frequency shift into a change in power transmitted through the spectral filter. (e) Improved SNR in the detection of the generalized Doppler Raman-induced frequency shift can be obtained by converting the frequency shift, $\delta\omega$, into a time delay, $\Delta\tau = \varphi_2\,\delta\omega$ by passing the probe pulse through an optically dispersive system. We analyze the detection of the time delay change through RF phase detection, and thus this method is labeled (RF). (f) The probe pulse can be obtained from a shaped pump pulse (making a pulse train, or a pair of pulses). To detect a signal, the input pulse spectrum is clipped with a low pass filter, then the power of newly generated spectral components is detected with a complementary high pass filter. This class of methods is labeled FT-CARS (FT). Note that interference between the coherent vibrational and nonresonant scattering is critical in these measurements.

by shot noise, where the SNR scales as the square root of the average power, or relative intensity noise (RIN) that produces an SNR scaling that is independent of incident power. Details of this scaling for several standard detectors used in CRS experiments are provided in appendix B.

At low powers electronic noise, including Johnson noise, is the dominant contribution to noise in photodetection. The minimum detectable power is characterized by the noise equivalent power (NEP) of the photodetector. The NEP of a typical detector is NEP = 50 fW $\mathrm{Hz}^{-1/2}$, which means that in a 10 μs integration time, an incident average power of $\bar{p} \sim 11.2$ pW will produce an SNR = 1. Some of the detection modes explored below will be subject to electronic noise at low concentrations due to low signal powers, and we remark on those constraints where it is relevant. At intermediate powers, SNR is dominated by shot noise, which is the regime that we focus on here. At higher power levels, the relative intensity noise (RIN) begins to play a significant limiting role. The focus on the shot noise limit is justified in a range of detected power levels because RIN is a technical noise that can be mitigated by strategies such as lock-in detection or balanced detection, which can extend the range of shot-noise limited detection. While these two strategies are burdened with experimental difficulties, they are routinely implemented, and in many cases the effects of RIN can be largely eliminated. Notably, RIN can not be avoided when detecting CRS signals with a spectrometer, and in those cases, the signal is usually dominated by RIN.

In all cases when we detect the optical power in a beam, we will assume that we make use of a detector with a responsivity of $\mathcal{R}$. We will assume a measurement bandwidth of $\Delta f = 1/2\ \Delta t$, where Δt is the measurement time. With this assumption, a beam with an average power of $\bar{p}$ incident on the detector will produce a rms shot noise current of $i_{\mathrm{sn}}^2 = e\mathcal{R}\bar{p}/\Delta t$, and e is the elementary charge.

For compactness of comparison of techniques, we will express the SNR in the form

$$\mathrm{SNR} \equiv \kappa\sqrt{\Delta t}, \tag{61}$$

where the SNR coefficient, κ, removes the impact of the detector integration time Δt. The result is that we may compare κ for experimental techniques to directly compare differences in the performance of CRS detection methods.

We further decompose the shot-noise limited SNR coefficient as

$$\kappa = W\delta\phi_0^v \Upsilon_{\mathrm{SH,j}}. \tag{62}$$

Here, we have isolated a factor that depends on the average power used in detection and the detector responsivity: $\Upsilon_{\mathrm{SH,j}} = \sqrt{\mathcal{R}\bar{p}_j/e}$, where we will indicate which average power belongs on this coefficient, the pump, $j = \mathrm{pu}$, or probe power, $j = \mathrm{pr}$. The term W is a weighting factor emerges for each experimental technique.

Similarly in the RIN limit, we decompose the SNR coefficient into

$$\kappa = Y\delta\phi_0^v \Upsilon_{\mathrm{RIN}}. \tag{63}$$

$\Upsilon_{\mathrm{RIN}} = \sqrt{2}\,10^{-\sigma_{\mathrm{RIN}}/20}$ sets the limits of SNR when RIN can not be mitigated at high probe power levels. The weighting factor, Y, for RIN displays a different functional dependence than for the shot noise limit.

For very low power levels where Johnson noise dominates, the SNR coefficient will be

$$\kappa = V\delta\phi_0^v \Upsilon_{\mathrm{J}}, \tag{64}$$

where $\Upsilon_{\mathrm{J}} = \bar{p}_{\mathrm{rp}}\mathcal{R}\sqrt{R_T/(2k_BT)}$, and again the weighting coefficient, V, depends on the CRS method. Here, k_B is the Boltzmann constant and T is the temperature in Kelvin.

Details of experimental conditions could potentially reduce these weighting factors, but in order to facilitate models where we can compare the relative performance of low frequency Raman methods, we assume Gaussian spatial beams and Gaussian temporal and spectral envelopes. We will consider only idealized experimental configurations, driven at the peak resonant Raman vibrational frequency, and with an experimental configuration that optimizes SNR. An interesting consequence of considering the shot noise limited SNR expressions, is that even for cases there the CRS signal is not linear in the forced Raman response, quantified by $\delta\phi_0^{v,mn}$, the SNR is indeed linear in $\delta\phi_0^{v,mn}$. To simplify the description and allow for direct comparison of experimental techniques, we will consider only a single impulsively excited vibrational frequency, so that we will write $\Omega_{v,mn} \to \Omega_v$ and we will use $c_m = 1$, so that we have a maximum accumulated probe phase shift of $\delta\phi_0^{v,mn} \to \delta\phi_0^v$.

We will continue with our example experimental numbers for both the neat and 1 mM concentration level of acetonitrile. The SNR coefficients for these two cases will be provided for each experimental configuration. Moreover, a detection time required to reach an SNR of 3 will be provided for each case. For these example experimental conditions, and an average power (pump or probe, depending on the experiment) of the factor $\Upsilon_{\mathrm{SNR,pr}}$. For an average probe power of 10 mW, $\Upsilon_{\mathrm{SNR,pr}} \sim 1.77 \times 10^8\,\sqrt{\mathrm{Hz}}$ for a simple photodiode. The largest value of $\Upsilon_{\mathrm{SNR,j}}$ is limited by either the saturation power of the photodiode, given by $p_{\mathrm{sat}} = (V_{\mathrm{bias}} + V_{\mathrm{bi}})/[(R_T + R_s)\mathcal{R}]$, or the RIN of the probe pulse laser source. Here V_{bias} is the bias voltage. V_{bi} and R_s are the built in voltage and the photodiode resistance from the photodiode equivalent circuit model. The saturation power can be moderately improved, and thus the shot noise SNR limit, by increasing the load resistance, R_T, and the bias voltage, V_{bias}, provided that the bias voltage does not exceed the breakdown voltage. When RIN can not be mitigated, the SNR is quite limited as Υ_{RIN} is on the order of the strength of shot noise ($\sim 10^8$) for a low RIN of $\sigma_{\mathrm{RIN}} = -160$ dBc Hz^{-1} and drops to $\sim 10^5$ for a high RIN of $\sigma_{\mathrm{RIN}} = -120$ dBc Hz^{-1}. Thus, RIN should be avoided with lock-in amplifier detection and balanced detectors whenever possible.

4.1. Raman spectral detection through transient RI changes

In CRS experiments, a forced Raman response is driven by pump pulses, then a probe pulse is used to convert this phase perturbation into a CRS signal. In low frequency Raman spectroscopy, usually a single pulse is used to impulsively drive the Raman response, producing a perturbation in the effective linear [28] and nonlinear [64, 65] susceptibilities, and thus the RI, which is detected by a probe pulse. The perturbation in the RI may be directly interrogated when the probe pulse is sufficiently short, and the relative arrival time of the pump and probe pulses must be varied in order to extract the Raman temporal response. In cases where the pulses are not resonant with electronic transitions, the RI perturbation is purely real and the Raman vibrational coherence is prepared solely on the ground electronic state, leading to only scattering and phase shifts. Whereas, under resonant excitation conditions, the RI is complex and the Raman vibrational coherence involve both ground and excited state vibrational modes [75]. For this resonant excitation, the imaginary component of the RI perturbation imparts time-varying absorption as well.

The change in RI may be converted to a measurable signal in a number of ways. At an abrupt boundary, the RI perturbation can be detected through a perturbation of Fresnel reflection and transmission coefficients [64, 65, 76]. Other methods for reading out the RI perturbation include interferometry

[49, 77–79], polarization rotation [72, 80, 81], and transient lensing [25]. In addition, the pump pulse can be used to establish a transient grating for detection of the RI perturbation. Below, we estimate the SNR coefficient for some of the most common low frequency Raman spectroscopy techniques that exploit a measurement of the RI perturbation. While not a comprehensive list, the SNR values are quite similar for other, less common, measurement techniques.

4.1.1. Transient grating (TG)

Low frequency Raman ISRS spectra can be recorded in a transient grating geometry [82, 83]. Figure 9(a) shows the experimental scenario, where the excitation of the coherent Raman response produces a grating in the perturbed RI distribution from a pair of impulsive pump pulses crossing non-collinearly. The pump pulse pair produces a phase grating that may be described as

$$\delta\phi_{\mathrm{TG}}(\tau, x) = \delta\phi_m(\tau)\cos(\Delta k_{\mathrm{pu,x}}\, x), \tag{65}$$

where the amplitude of the phase grating is determined by the RI perturbation induced by the pump pulses. The transient phase grating will diffract the probe pulse, incident non-collinearly with either pump pulse, to induce a probe signal. Assuming that the probe pulse is also short enough in time to be considered impulsive, then the probe pulse field amplitude diffracted to the first order is

$$A_{\mathrm{TG}}^{+1}(\tau) = iJ_1[\delta\phi_m(\tau)]A_{\mathrm{pr}}. \tag{66}$$

The Raman spectrum is then recorded by measuring the diffracted power with respect to pump-probe arrival time delay, τ. The average diffracted power reads

$$\bar{p}_{\mathrm{TG}}^{+1}(\tau) = J_1^2[\delta\phi_m(\tau)]\bar{p}_{\mathrm{pr}}. \tag{67}$$

Note that for the weak phase grating, we may make the approximation $J_1(z) \approx x/2$.

With this approximation, we may write the maximum SNR weighting factor in the SNR coefficients of the diffracted beam detection as $W_{\mathrm{TG}} = 1/2$ in the shot-noise limit in equation (62), $Y_{\mathrm{TG}} = \delta\phi_0^v/4$ in the RIN limit in equation (63), and $V_{\mathrm{TG}} = \delta\phi_0^v/4$ in the Johnson noise limit in in equation (64). Our experimental examples lead to quantitative shot-noise limited values of $\kappa_{\mathrm{TG}} \sim 1.13 \times 10^6\sqrt{\mathrm{Hz}}$ and $\kappa_{\mathrm{TG}} \sim 59.7\sqrt{\mathrm{Hz}}$ for neat and 1 mM acetonitrile, respectively. These cases require $\Delta t_{\mathrm{TG}} \sim 7.08$ ps and $\Delta t_{\mathrm{TG}} \sim 2.53$ ms to attain an SNR value of 3. While the theoretically derived integration time to reach in SNR is in the ps range here, we emphasize that this is a formal, rather than a practical number, and in an experiment a integration time of order μs or higher will typically be used. Moreover, the quadratic dependence of the TG signal power on the concentration means that in many scenarios, TG detection is Johnson-noise limited and the detection of low concentrations is difficult.

An advantage of TG experiments is that since the beams propagate along distinct directions complete polarization control of all beams is possible, thus enabling the probing of all of the tensor elements of the Raman and the nonresonant response. However, the quadratic dependence of the TG signal on $\delta\phi_0^v$ leads to both weak signals and distortion of the spectrum. These distortions and weak signal strength can be mitigated by introducing a local oscillator field to perform heterodyne transient grating spectroscopy [84].

4.1.2. Interferometric (INT)

The change in RI induced through ISRS driven by the pump pulse can be interferometrically detected [43, 49, 78, 79, 85]. In our model, we consider a pair of identical probe and reference pulses with the same total average power as the probe power used in other methods. That is, the average power of the probe pulse and the reference pulse are each half of the total probe power used other experimental techniques. The probe pulse is set to arrive after the pump pulse so that it accumulates a phase shift from the ISRS excitation. In addition, we assume that an additional phase shift of ϕ_r can be imparted to the reference pulse relative to the probe pulse. Under these conditions, the average power incident on a detector is $\bar{p}_{\mathrm{INT}} = \bar{p}_{\mathrm{pr}}(1 + \cos[\delta\phi_m(\tau) - \phi_r])$. To maximize the detected signal, we adjust the small relative phase to be in quadrature, $\phi_r = \pi/2$, and the shot noise is driven by the $\bar{p}_{\mathrm{pr}}$.

Because interferometric detection makes uses of a small signal power perturbation relative to the probe background power, under typical experimental conditions, the noise is limited either by shot noise, where the maximum SNR weighting factor in the SNR coefficient is $W_{\mathrm{INT}} = 1$ in equation (62), or RIN for higher power levels, where the RIN weighting factor in equation (63) is also unity $Y_{\mathrm{INT}} = 1$. Whenever possible, balance detection should be used to suppress RIN. The SNR can be significantly improved by the use of chirped pump, probe, and reference pulses due to a combination of the reduction of the nonresonant background and selective Raman excitation from spectral focusing [49].

Our experimental examples lead to quantitative shot-noise limited values of $\kappa_{\rm INT} \sim 3.19 \times 10^6 \sqrt{\rm Hz}$ and $\kappa_{\rm INT} \sim 169 \sqrt{\rm Hz}$ for neat and 1 mM acetonitrile, respectively. These cases require $\Delta t_{\rm int} \sim 0.885$ ps and $\Delta t_{\rm int} \sim 0.316$ ms to attain an SNR value of 3. When the SNR is RIN-limited, the SNR coefficients drop to $\kappa_{\rm INT} \sim 5.71 \times 10^5 \sqrt{\rm Hz}$ and $\kappa_{\rm INT} \sim 30.2 \sqrt{\rm Hz}$ for neat and 1 mM acetonitrile for a RIN of $\sigma_{\rm RIN} = -150$ dBc Hz^{-1}.

4.1.3. Kerr lensing (KL)

In a recent experiment, the spatial variation of the transient perturbation to the RI was exploited for an ISRS KL measurement of low frequency Raman spectra [25]. We model this process by considering a spatial beam profile of the pump and probe pulses to be Gaussian with a $1/e$ beam radius of w_0. The spatial variation in the peak RI then follows the relationship $\delta\phi_0(\rho) = \delta\phi_0 \exp(-2(\rho/w_0)^2)$ and $\rho = \sqrt{x^2+y^2}$ is the the transverse radial coordinate in the $(x-y)$ plane that is transverse to the direction of propagation, z. An analytic model of the KL ISRS is obtained by truncating the Gaussian phase perturbation with a quadratic phase to approximate the spatial phase perturbation as a thin lens that is induced by the phase of the impulsively excited forced Raman response. To convert this transient Kerr lens into a detectable change in probe power, the phase modulated beam is propagated through a 2f optical system, where the sample interaction plane is in the front focal plane and a circular aperture with a radius of $w_{\rm ap}$ and a detector are placed at a distance z away from the back focal plane of a collection lens with focal length f.

The transient phase perturbation produces a change in beam size in the back focal plane of the objective. For the Gaussian beam model, the perturbed probe beam propagating in the vicinity of the back focal plane is also Gaussian, with a beam 1/e field radius, $w_{\delta\phi_0^\nu}$, of the perturbed probe beam at a position $z = \zeta z_R$ that is given by

$$w_{\delta\phi_0^\nu} = w_b \sqrt{1 + (2\,\delta\phi_0^\nu + \zeta)^2}. \tag{68}$$

Here $w_b = \lambda f/(\pi w_0)$ is the unperturbed Gaussian beam size at the back focal plane of the unperturbed probe beam (i.e. for $\zeta = 0$ and $\delta\phi_0^\nu = 0$) and $\zeta = z/z_R$ is a normalized propagation distance relative to the Rayleigh length of the unperturbed Gaussian beam in the back focal plane, $z_R = \pi w_b^2/\lambda$.

The KL coherent Raman signal is obtained by measuring the fluctuations in power obtained from the beam transmitted through an aperture with a radius of $w_{\rm ap}(a,\zeta) = a\,w_b\sqrt{1+\zeta^2}$, so that a is the aperture radius relative to the unperturbed Gaussian beam in at a defocused plane $z = \zeta z_R$ relative to the back focal plane.

The efficiency of probe power transmission through the aperture with normalized radius $a = w_{\rm ap}(a,\zeta)/w_b(\zeta)$ as defined above is $\eta_{\delta\phi_0}(a,\zeta) = 1 - \exp\{-(2a^2(1+\zeta^2))/(1+(2\,\delta\phi_0+\zeta)^2)\}$. The signal power from KL is due to the change of the probe pulse power transmission as a result of the spatial variation of the Raman phase modulation, giving a value of $\bar{p}_{\rm KL} = \Delta\eta(a,\zeta)\,\bar{p}_{\rm pr}$. Here the differential change in transmission efficiency is simply $\Delta\eta(a,\zeta) = \eta_{\delta\phi_0}(a,\zeta) - \eta_{\delta\phi_0=0}(a,\zeta)$. Making a Taylor expansion of this differential transmission efficiency by relying on the weak phase perturbation, gives the first order signal term in phase modulation of $\Delta\eta(a,\zeta) \approx -P(a,\zeta)\,\delta\phi_0^\nu$, and where $P(a,\zeta) = 8\zeta a^2 \exp(-2a^2)/(1+\zeta^2)$. These signal power fluctuations are against a background power of $\bar{p}_{\rm bkg} = \eta_{\delta\phi_0=0}(a,\zeta)\,\bar{p}_{\rm pr}$. Optimal discrimination of the ISRS signal power occurs when the normalized radius of a circular aperture transmission aperture is set to $a = 1/\sqrt{2}$ and the defocus distance $|\zeta| = 1$, leading to an optimal signal power of $\bar{p}_{\rm KL} \approx 0.736\,\bar{p}_{\rm pr}\,\delta\phi_0^\nu$ and a mean background power of $\bar{p}_{\rm bkg} \approx 0.632\,\bar{p}_{\rm pr}$.

Due to the high background power, KL operates in only the shot and RIN limited noise regimes. The SNR factor for KL in the shot noise limit is given by $W_{\rm KL} = \left[P(a,\zeta)/\sqrt{\eta_{\delta\phi_0=0}(a)}\right]$, leading to

$$W_{\rm KL} = \frac{8\zeta a^2 e^{-2a^2}}{(1+\zeta^2)\sqrt{1-e^{-2a^2}}}. \tag{69}$$

The SNR is optimized for a value of $|a| \approx 0.567$ and for $|\zeta| = 1$, so that we may approximate the maximum value $W_{\rm KL} \approx 0.982$. When RIN is relevant, we make use of the RIN limit SNR factor of

$$Y_{\rm KL} = \frac{8\zeta a^2 e^{-2a^2}}{(1+\zeta^2)(1-e^{-2a^2})}, \tag{70}$$

which evaluates to $Y_{\rm KL} \approx 2$ for the optimal experimental configuration.

Our experimental examples lead to quantitative values in the shot-noise limit of $\kappa_{\rm KL} \sim 2.21 \times 10^6 \sqrt{\rm Hz}$ and $\kappa_{\rm KL} \sim 117 \sqrt{\rm Hz}$ for neat and 1 mM acetonitrile, respectively, and corresponding to integration times of $\Delta t_{\rm KL} \sim 1.84$ ps and $\Delta t_{\rm KL} \sim 656\,\mu$s to attain an SNR value of 3. In the RIN limit, the SNR coefficients change

to $\kappa_{\mathrm{KL}} \sim 1.14 \times 10^6 \sqrt{\mathrm{Hz}}$ and $\kappa_{\mathrm{KL}} \sim 60.4 \sqrt{\mathrm{Hz}}$ for neat and 1 mM acetonitrile, respectively for a RIN of $\sigma_{\mathrm{RIN}} = -150$ dBc Hz^{-1}, and drop rapidly for large RIN values.

4.1.4. Kerr steering

In the same report where KL was introduced [25], the pump beam was steered to the edge of the probe beam so that the probe beam experienced an approximate linear slope in the perturbation to the RI that is induced by the pump pulse. In this regime, we consider the phase perturbation as a transient Kerr prism that steers the probe beam. By using a knife edge (or a photodiode edge), the beam steering may be converted into a change in power the Raman time-domain spectroscopic signal is recorded by measuring the KS power as the pump-probe time delay is varied.

In the experimental configuration for KS, the pump beam is displaced by a distance along the x-direction. For the sake of argument, consider a displacement distance of $\Delta x = \Delta\beta\, w_0$ that is scaled by the focal beam size of the pump and probe, w_0, and $\Delta\beta$ is the normalised beam displacement. Now the phase perturbation acquired by the probe pulse is offset and the probe pulse will the shifted laterally along the x-direction in the back focal plane of a 2f optical system where we place a detector. When we convert the shift into a change in transmitted power by a knife edge that is aligned with the y direction and translated in x by $x_{\mathrm{BFP}} = b\, w_b$ and b is the normalized edge filer displacement, then the probe pulse power transmission is

$$\eta_{\delta\phi_0}(b) = \frac{1}{2}\left[\mathrm{erf}\left(\frac{\sqrt{2}(b + \Delta\beta\,\delta\phi_0^{\nu})}{\sqrt{1 + 4\,(\delta\phi_0^{\nu})^2}}\right) + 1\right]. \tag{71}$$

As with KL, the signal due to the Raman excitation arises from changes in the transmitted probe pulse power due to a change in transmission efficiency defined in the same way as with KL, $\bar{p}_{\mathrm{KS}} = \Delta\eta(b)\,\bar{p}_{\mathrm{pr}}$. The first-order Taylor expansion of the change in transmission efficiency is written as $\Delta\eta(b) = P(b)\,\delta\phi_0^{\nu}$, where $P(b) = \sqrt{2/\pi}\,\exp(-2b^2)\,\Delta\beta$, which is clearly peaked for $b = 0$.

The SNR coefficient for KS follows from the signal power, with noise dominated by the average transmitted probe power, $\bar{p}_{\mathrm{bkg}} = \eta_{\delta\phi_0=0}(b)\,\bar{p}_{\mathrm{pr}}$. The SNR factor for KS in the shot noise limit is then found to be $W_{\mathrm{KS}} = P(b)/\sqrt{\eta_{\delta\phi_0=0}(b)} = 2\,\Delta\beta\,\exp(-2\,b^2)/\sqrt{\pi\,(1 + \mathrm{Erf}(\sqrt{2}\,b)}$. When RIN is relevant, we make use of the RIN limit SNR factor of $Y_{\mathrm{KS}} = 2\sqrt{2/\pi}\,\Delta\beta\,\exp(-2\,b^2)/(1 + \mathrm{Erf}(\sqrt{2}\,b))$, which evaluates to $Y_{\mathrm{KS}} \approx 1.60\,\Delta\beta$ for the optimal experimental configuration.

The SNR is optimized for a value of $a \approx -0.306$, so that we may approximate the maximum value $W_{\mathrm{KS}} \approx 1.27\,\Delta\beta$. Our experimental examples lead to quantitative values in the shot-noise limit of $\kappa_{\mathrm{KS}} \sim 1.43 \times 10^6 \sqrt{\mathrm{Hz}}$ and $\kappa_{\mathrm{KS}} \sim 75.8 \sqrt{\mathrm{Hz}}$ for neat and 1 mM acetonitrile, respectively, and corresponding to integration times of $\Delta t_{\mathrm{KS}} \sim 4.39$ ps and $\Delta t_{\mathrm{KS}} \sim 1.57$ ms to attain an SNR value of 3 for neat acetonitrile at the two concentration values. In the RIN limit, the SNR coefficients change to $\kappa_{\mathrm{KS}} \sim 8.71 \times 10^5 \sqrt{\mathrm{Hz}}$ and $\kappa_{\mathrm{KS}} \sim 46.1 \sqrt{\mathrm{Hz}}$ for neat and 1 mM acetonitrile, respectively for a RIN of $\sigma_{\mathrm{RIN}} = -150$ dBc Hz^{-1}.

4.2. Raman spectral detection through a probe spectral shift ($\delta\omega$)

The shift of the centroid of the probe pulse, $\delta\omega_R(\tau)$, described in the previous section can be used to detect low-frequency Raman signals [22, 24, 27, 28, 56, 67, 86], which can be detected on a spectrometer or with spectral filtering. For purpose of SNR calculations, we will use the peak frequency shift of $\delta\omega_0^{\nu} = \Omega_{\nu}\,\delta\phi_0^{\nu}$. Assuming a Gaussian temporal pulse with a profile $\exp[-(t/\tau_p)^2]$, the frequency shifted Gaussian pulse power spectral density reads

$$S_{\mathrm{pr}}(\Omega) = \frac{\bar{p}_{\mathrm{pr}}}{\sqrt{2\,\pi}}\,\frac{\tau_p}{\nu_R}\,\exp\left[-2\,\left(\frac{\tau_p}{2}\{\Omega - \delta\omega_0^{\nu}\}\right)^2\right]. \tag{72}$$

When the frequency shifted probe beam is transmitted through a spectral filter, the frequency shift is converted to a change in transmitted optical power. Assuming a high-pass optical filter with a cutoff frequency of Ω_c, the power transmitted through the filter is given by $\eta(x_c)\,\bar{p}_{\mathrm{pr}}$, with the transmission efficiency $\eta(x_c) = (1 + \mathrm{erf}[(x_c + \tau_p\,\delta\omega_0^{\nu})/\sqrt{2}])/2$ for the normalized cutoff frequency $x_c = \tau_p\,\Omega_c$. This leads to a background power of $\bar{p}_{\mathrm{bkg}} \approx \eta_{\delta\omega=0}(x_c) = (1 + \mathrm{erf}[x_c/\sqrt{2}])/2$. The signal power comes from the change in transmission efficiency with frequency shift, $\bar{p}_{\mathrm{sig}} = \Delta\eta(x_c)\bar{p}_{\mathrm{pr}}$, where $\Delta\eta(x_c) = \eta(x_c) - \eta_{\delta\omega=0}(x_c)$. Taking a first order Taylor expansion with respect to small frequency shifts, we obtain a signal power of $\bar{p}_{\mathrm{sig}} \approx -P_{\delta\omega}(x_c)\,\delta\phi_0^{\nu}\,\bar{p}_{\mathrm{pr}}$, where $P_{\delta\omega}(x_c) = \tau_p\,\Omega_{\nu}\,\exp(-x_c^2/2)/\sqrt{2\,\pi}$.

Here again, the noise is dominated by the average background power that is much larger than the small signal power fluctuations, leading to an SNR coefficient for frequency shifting in the shot noise limit of $W_{\delta\omega} = P(x_c)/\sqrt{\eta_{\delta\phi_0=0}(x_c)} = \tau_p\,\Omega_{\nu}\,\exp(-x_c^2/2)/\sqrt{\pi[1 + \mathrm{erf}(x_c/\sqrt{2})]}$. In the shot noise limit, SNR is optimized when $x_c \approx -0.6$, leading to $W_{\delta\omega} \approx 0.636\,\tau_p\,\Omega_{\nu} \approx 4\,(\tau_p/T_{\nu})$, where $T_{\nu} = 2\,\pi/\Omega_{\nu}$ is the vibrational

period. When RIN is relevant, we make use of the RIN limit SNR factor of $Y_{\delta\omega} = \sqrt{2/\pi}\,\tau_p\,\Omega_v\,\exp(-x_c^2/2)/(1+\mathrm{erf}[x_c/\sqrt{2}])$, which evaluates to $Y_{\delta\omega} \approx 1.22\,\tau_p\,\Omega_v \approx 7.63\,(\tau_p/T_v)$.

Our experimental examples lead to quantitative values in the shot-noise limit of $\kappa_{\delta\omega} \sim 4.23\ \times 10^6\,\sqrt{\mathrm{Hz}}$ and $\kappa_{\delta\omega} \sim 234\,\sqrt{\mathrm{Hz}}$ for neat and 1 mM acetonitrile, respectively. These cases require $\Delta t_{\delta\omega} \sim 2.0$ ps and $\Delta t_{\delta\omega} \sim 718\,\mu$s to attain an SNR value of 3. In the RIN limit, the SNR coefficients change to $\kappa_{\delta\omega} \sim 2.04\ \times 10^6\,\sqrt{\mathrm{Hz}}$ and $\kappa_{\delta\omega} \sim 108\,\sqrt{\mathrm{Hz}}$ for neat and 1 mM acetonitrile, respectively for a RIN of $\sigma_{\mathrm{RIN}} = -150$ dBc Hz^{-1}.

4.3. Raman spectral detection through transforming a probe spectral shift into a probe pulse time delay (RF)

For low concentrations of target molecules, the phase shift, and thus the frequency shift imparted by CRS becomes quite small, preventing the detection of small frequency shifts, $\delta\omega$. High resolution spectrometers are still limited to resolving a spectral resolution of the order of $\Delta\lambda \sim 0.05$ nm or an optical spectral resolution of $\Delta\nu \sim 15$ GHz (at a center wavelength of 1000 nm). Frequency shift detection based on the change in the centroid of the power spectrum produces improved sensitivity to small frequency shifts. Rewriting our expression above, for the SNR coefficient in the shot noise limit leads to $\kappa_{\delta\omega} \approx 2\,\tau_p\,\delta\nu\,\Upsilon_{\mathrm{SH,pr}}$. With this technique, in a 10 μs integration time, we can detect a frequency shift of $\delta\nu \sim 52$ MHz, and if we wait for 10 ms, this frequency shift drops to $\delta\nu \sim 1.67$ MHz. However, this still corresponds to a molecular concentration in the mM range.

More sensitive detection of small frequency shifts is possible by converting the frequency shift, $\delta\omega$ into a change in transit time, $\Delta\tau$, through a dispersive system [87, 88]. For a second-order limited dispersive system with a group delay dispersion (GDD) φ_2, the change in transit time is $\Delta\tau = \varphi_2\,\delta\omega$. This strategy enables amplification of the coherent Raman signal outside of the interaction region. Considering our example experimental parameters, the frequency shifts of $\delta\nu_0 \sim 119$ GHz and $\delta\nu_0 \sim 6.3$ MHz for neat and 1 mM of acetonitrile produces transit time changes of $\Delta\tau \sim 25.1$ ps and $\Delta\tau \sim 1.33$ fs, for a dispersive system with a GDD of $\varphi_2 = 33.5$ ps^2. These values of transit time delay are many orders of magnitude higher than the rms timing jitter from mode-locked solid state oscillators [89–92].

Detection of coherent Raman signals by converting a frequency shift into a transit time change has been implemented by adapting RF phase methods used for precision timing jitter metrology measurements. In this strategy, the shot noise comes from RF power within the harmonic of the laser pulse repetition rate frequency used for detection, which exhibits a timing jitter PSD of $S_{\delta\tau} = h\nu_{\mathrm{laser}}/[p_{\mathrm{RF}}\,(2\,\pi\,\nu_R)^2]$. Assuming detection of the mth harmonic of the laser repetition rate frequency ν_R for the average probe pulse power in mth harmonic p_{RF} incident in the photodetector, we have an SNR coefficient of $\kappa_{\mathrm{RF}} = W_{\mathrm{RF}}\,\delta\phi_0^{\nu}\,\Upsilon_{\mathrm{RF}}$, where the RF detection weighting coefficient is $W_{\mathrm{RF}} = 2\,\pi\,m\,\nu_R\,\Omega_v\,\exp[-(\tau_p\,\Omega_v/2)^2/2]\,\varphi_2$ and $\Upsilon_{\mathrm{RF}} = \sqrt{p_{\mathrm{RF}}/h\nu}$. Assuming an RF power of $p_{\mathrm{RF}} = 6.07$ mW, the $m = 5$ harmonic order of the laser, and the GDD stated above, we obtain $\Upsilon_{\mathrm{RF}} \approx 1.74\ \times 10^8\,\sqrt{\mathrm{Hz}}$ and the weighting factor is $W_{\mathrm{RF}} \sim 5.80$. This leads to values of $\kappa_{\mathrm{RF}} \approx 1.29\ \times 10^7\,\sqrt{\mathrm{Hz}}$ and $\kappa_{\mathrm{RF}} \approx 684\,\sqrt{\mathrm{Hz}}$ for neat and 1 mM acetonitrile, respectively. These cases require $\Delta t_{\mathrm{RF}} \approx 53.8$ fs and $\Delta t_{\mathrm{RF}} \approx 19.2\,\mu$s to attain an SNR value of 3. To first order, RIN is not a limiting factor because amplitude fluctuations are rejected in the RF phase detection circuitry.

4.4. Single pulse CARS with power detection (FT)

In the previous section, ISRS signals were detected through a frequency shift imparted by a time-varying perturbation to the effective linear optical susceptibility in a Raman-active sample that was prepared by a pump pulse with temporal structure shorter than the vibrational period of the excited modes. We demonstrated that the spectral shift arises from the interference from the overlap of the incident probe pulse spectrum and the sidebands scattered by the nominally sinusoidal phase modulation imparted by the forced Raman response. If we isolate only those spectral components that are scattered to distinct new frequencies that are at a higher frequency than any spectral components within the input probe spectrum, we may detect a coherent anti-Stokes Raman scattering (CARS) signal [34]. The spectral features are some of the very same spectral components that are detected in frequency-shifting ISRS. In CARS, however, only newly scattered spectral components are passed along to the detector. We also note that the same analysis could be applied to coherent Stokes Raman scattering (CSRS) by isolating new frequencies that have scattered to a lower frequency. CSRS is much less common because of excess noise from fluorescent light emission that reduces the SNR.

For the reasons discussed previously, low frequency Raman components are effectively driven only by single pulse excitation. Broadly, single pulse CARS methods can use pulse shaping [93–95], or even just a pair of pulses [96, 97] that are sent into the medium and act as both pump and probe pulses. In the case of pulse shaping, a shaped laser pulse can impulsively excite a molecular vibration with a strength up to that of

a transform-limited pulse, but with the ability to selectively excite only desired spectral modes. Selective vibrational excitation is readily enabled by a pulse shaper with sinusoidal phase modulation, or even simply a pair of time-delayed probe pulses [69]. These cases provide a concrete scenario for computing the capabilities for low frequency vibrational mode spectroscopy and for obtaining an expression for the SNR.

Fourier transform CARS (FT-CARS) will be specifically analyzed here where we consider pulses spaced by a relative delay τ. We note, however, that the application of a sinusoidal phase modulation is functionally similar, in that a pulse train with a delay spacing inversely proportional to the spectral phase modulation period. Thus, the same arguments that we will use for FT-CARS apply, but the resultant expressions are considerably more unwieldy, making it more difficult to provide clear physical interpretations.

In FT-CARS, a pair of equal energy pulses is focused into specimen to drive a forced Raman response that is detected by recording the average power of light scattered to new high-frequency spectral components. By resolving this scattered power as a function of relative delay, τ, between the two pulses, the Raman spectrum may be obtained through a Fourier transform of the recorded data. In order to isolate the new high frequency spectral components, the pulses are spectrally clipped on the high-frequency side of the input pulse spectrum with a low-pass edge spectral filter with a cutoff frequency of $\Omega_{\rm lp}$. After the sample, the pulses are passed through a second complementary high-pass spectral edge filter (HPF) with a cutoff spectral frequency of $\Omega_{\rm hp} = \Omega_{\rm lp} + \Delta$. The gap in frequency, Δ, is necessary to ensure that only newly scattered frequencies are detected. Unfortunately, the spectral gap impedes our ability to detect low frequency Raman vibrational features. Moreover, we will show that the CARS signal itself is biased against low frequency Raman detection.

For the sake of quantitative comparison to other CRS techniques, we will consider a total average power of the input FT CARS that is equal to the pump pulse average power, $\bar{p}_{\rm pu}$. As the high pass filter only passes spectral content that is not present in the incident pulses, for a single excited vibrational mode, we consider only the high frequency spectra given in equation (59). Assuming that the total pulse energy is split equally between each FT-CARS pulse, the power spectral density (PSD) that is transmitted through the high-pass filter can be decomposed into four terms,

$$S_{\rm CARS}(\Omega) = S_{\rm nr}(\Omega) + S_{\rm sb+}(\Omega) + S_{m1}(\Omega) + S_{m2}(\Omega). \tag{73}$$

For our model, we assume a weak phase perturbation for the SPM and forced Raman phase modulation terms. This model takes into account that in impulsive excitation the pump pulse experiences only a red shift upon vibrational excitation, which does not appear in the high-frequency CARS spectrum.

The first power spectral density term arises from the self phase modulation applied to the pulses that produces a non-resonant scattered spectrum that passes through the HPF, given by $S_{\rm nr}(\Omega) = (\delta\phi_0^{\rm nr})^2$ $S_b(\Omega)\, H_f(\Omega)/2$. Here $S_b(\omega) = |U_b(\Omega)|^2$ is the power spectrum of the nonresonant scattered portion of the pulse. We model the HPF as a Heavyside step function with $H_f(\Omega) = \Theta(\Omega - \Omega_{\rm hp})$. The second term is the positive frequency sideband, $S_{\rm sb+}(\Omega) = (\delta\phi_0^{\nu})^2 \exp(-\Gamma_\nu \tau)\, S_{\rm pr}(\Omega - \Omega_\nu)\, H_f(\Omega)/32$. The final two terms arise from interference from between the spectral overlap of the SPM broadened spectrum and the high frequency sideband scattered by the forced Raman response. Defining a power spectrum of the interference term, $S_{\rm int}(\Omega) = \delta\phi_0^{\rm nr}\, \delta\phi_0^{\nu} \exp(-\Gamma_\nu \tau/2)\, U_b(\Omega)\, U_{\rm pr}(\Omega - \Omega_\nu)\, H_f(\Omega)$, the PSD from interference of the SPM and vibrational spectra is $S_{m1}(\Omega) = S_{\rm int}(\Omega)\, \sin(\Omega_\nu \tau)$. The final PSD term arises from interference of the SPM spectrum from the first pulse and the Raman scattering of the second pulse, $S_{m2}(\Omega) = S_{\rm int}(\Omega)\, \sin([\Omega_\nu - \Omega]\tau)$.

The collected power for each PSD term incident on the detector is obtained by applying the appropriate integral bounds. The FT-CARS signal is obtained from the oscillatory component of the power detected that depends on the relative delay, τ, that is provided by the third PSD term. The signal background arises from the terms that are independent of τ. Upon evaluation of the integrals, we find that the approximate shot-noise limited SNR factor is given by

$$W_{\rm FT} \approx \frac{\operatorname{erf}\left(\frac{\tau_p\left(\Omega_{\rm lp} + \frac{\Omega_\nu}{4}\right)}{\sqrt{3}}\right) - \operatorname{erf}\left(\frac{\tau_p\left(\Omega_{\rm lp} + \Delta - \frac{3}{4}\Omega_\nu\right)}{\sqrt{3}}\right)}{2\sqrt{2r^2\left(\operatorname{erf}\left(\frac{\Omega_{\rm lp}\tau_p}{\sqrt{2}}\right) - \operatorname{erf}\left(\frac{\tau_p\left(\Omega_{\rm lp} + \Delta - \Omega_\nu\right)}{\sqrt{2}}\right)\right) + \frac{32}{\sqrt{3}}\operatorname{erfc}\left(\frac{\tau_p\left(\Omega_{\rm lp} + \Delta\right)}{\sqrt{6}}\right)}}. \tag{74}$$

Here, we have defined the ratio of the vibrational to non-resonant phase modulation as $r = \delta\phi_0^{\nu}/\delta\phi_0^{\rm nr}$. The functions erf and erfc are the error and complementary error functions, respectively. In the RIN limited case, the SNR scaling factor becomes

$$Y_{\mathrm{FT}} \approx \frac{4\sqrt{2}\left[\mathrm{erf}\left(\frac{\tau_p\left(\Omega_{\mathrm{lp}}+\frac{\Omega_v}{4}\right)}{\sqrt{3}}\right)-\mathrm{erf}\left(\frac{\tau_p\left(\Omega_{\mathrm{lp}}+\Delta-\frac{3}{4}\Omega_v\right)}{\sqrt{3}}\right)\right]}{\delta\phi_0^{\mathrm{nr}}\left[r^2\left(\mathrm{erf}\left(\frac{\Omega_{\mathrm{lp}}\tau_p}{\sqrt{2}}\right)-\mathrm{erf}\left(\frac{\tau_p\left(\Omega_{\mathrm{lp}}+\Delta-\Omega_v\right)}{\sqrt{2}}\right)\right)+\frac{16}{\sqrt{3}}\,\mathrm{erfc}\left(\frac{\tau_p\left(\Omega_{\mathrm{lp}}+\Delta\right)}{\sqrt{6}}\right)\right]}. \tag{75}$$

The SNR depends on more parameters for the FT and single pulse CARS experiments. These additional factors are accounted for in the weighting functions. We set the low pass filter to clip the spectral edge of the pulse to $\Omega_{\mathrm{lp}} = 2/\tau_p$ and the high pass filters that admits the new scattered frequencies onto the detector as $\Omega_{\mathrm{hp}} = \Omega_{\mathrm{lp}} + \Delta$, where we set $\Delta = 0.1/\tau_p$. At the example experimental conditions, $r \sim 0.121$ and $r \sim 6.40\ \times 10^{-6}$ for neat and 1 mM acetonitrile, respectively. Despite the discrepancy in r, the weighting function is approximately the same, $W_{\mathrm{FT}} \approx 0.040\,\tau_p\,\Omega_v$, or $W_{\mathrm{FT}} \approx 0.255$ for the 920.5 cm^{-1} mode excited by the short 17 fs pulse. In the RIN limit, we need to account for the fact that the carrier frequency of the FT interferogram sets the effective offset frequency and thus the RIN. Taking a value of $\sigma_{\mathrm{RIN}} = -120$ dBc Hz^{-1}, $Y_{\mathrm{FT}} \approx 9.04\,\tau_p\,\Omega_v$, or $Y_{\mathrm{FT}} \approx 27.0$ for the 920.5 cm^{-1} mode excited by the short 17 fs pulse.

Our experimental examples lead to quantitative values of $\kappa_{\mathrm{FT}} \sim 5.75\ \times 10^5\ \sqrt{\mathrm{Hz}}$ and $\kappa_{\mathrm{FT}} \sim 30.6\,\sqrt{\mathrm{Hz}}$ for neat and 1 mM acetonitrile, respectively. These cases require $\Delta t_{\mathrm{FT}} \sim 27.2$ ps and $\Delta t_{\mathrm{FT}} \sim 9.62$ ms to attain an SNR value of 3. Whereas in a RIN-limited case, the SNR coefficients are $\kappa_{\mathrm{FT}} \sim 4.81\ \times 10^5\ \sqrt{\mathrm{Hz}}$ and $\kappa_{\mathrm{FT}} \sim 25.7\,\sqrt{\mathrm{Hz}}$ for neat and 1 mM acetonitrile, respectively

Only vibrational frequencies that are greater than the gap between clipped frequencies and the HPF frequency are detected, i.e. $\Omega_v > \Delta$. Still at those low frequencies, the amplitude increases approximately linearly with increasing vibrational frequencies in order to increase the overlap between the SPM spectra and the vibrationally scattered sideband. Thus, FT-CARS and other single pulse CARS spectroscopes struggle to detect low vibrational frequencies. We note that for typical experimental conditions, $W_{\mathrm{FT}} < 1/10$, which means that the SNR will be lower than other techniques discussed, however, the lack of a need to isolate the probe pulse from the pump affords considerable experimental simplification.

5. Frequency-domain coherent Raman spectroscopy techniques

In the previous section, we discussed low frequency Raman detection modalities where the probe beam power is detected through spatial and spectral integration of the signal beam and Raman spectrum is obtained with a Fourier transform of the signal with respect to the pump probe delay τ. By contrast, frequency-domain methods record spectrally resolved signal power. The spectrum of the probe signal can generally be written as [66]

$$\hat{A}_{\mathrm{pr}}(\Omega) = A_{\mathrm{pr}}\,U_{\mathrm{pr}}(\Omega) * \left\{\delta(\Omega) + i\left[\tilde{\phi}_{\mathrm{nr}}(\Omega) + \tilde{\phi}_v(\Omega)\right]\right\}. \tag{76}$$

The probe spectrum is convolved with each term in brackets. The first Dirac delta function is simply the input spectrum, which is rejected with a spectral filter in a CARS experiment. The remaining two terms are the non-resonant term and the forced Raman excitation. In both cases for the latter terms, we will consider an impulsive pump pulse with a corresponding broad spectrum. This gives a non-resonant spectrum in terms of pump pulse driving term power spectral density as

$$\tilde{\phi}_{\mathrm{nr}}(\Omega) = \delta\phi_0^{\mathrm{nr}}\,T_n\,\tilde{D}_{\mathrm{pu}}(\Omega), \tag{77}$$

which provides a broad spectral background that will interfere with the forced Raman scattered spectrum. The forced Raman spectrum for a single vibrational resonance may be written as

$$\tilde{\phi}_v(\Omega) = \delta\phi_0^v\,\Gamma_v^{-1}\,R_v(\Omega)\tilde{D}_{\mathrm{pu}}(\Omega). \tag{78}$$

Note that we are restricting our discussion to a simplified Raman spectrum to facilitate the comparison of measurement SNR with the previous section.

Inspection of equation (76) immediately reveals that a short probe pulse, with a correspondingly broad spectrum, will blur the narrow Raman spectral features that we wish to resolve. As a consequence, when using short pulses, one uses strategies outlined in the previous section. The alternate approach that we explore in this section is to use a long probe pulse, in which case the probe spectrum is spectrally narrow and the Raman spectrum can be obtained by spectrally resolving the scattered probe spectrum, equation (76), with a spectrometer. Note that if the probe pulse is delayed in time, the cross phase modulation term is eliminated, further simplifying the spectral interpretation.

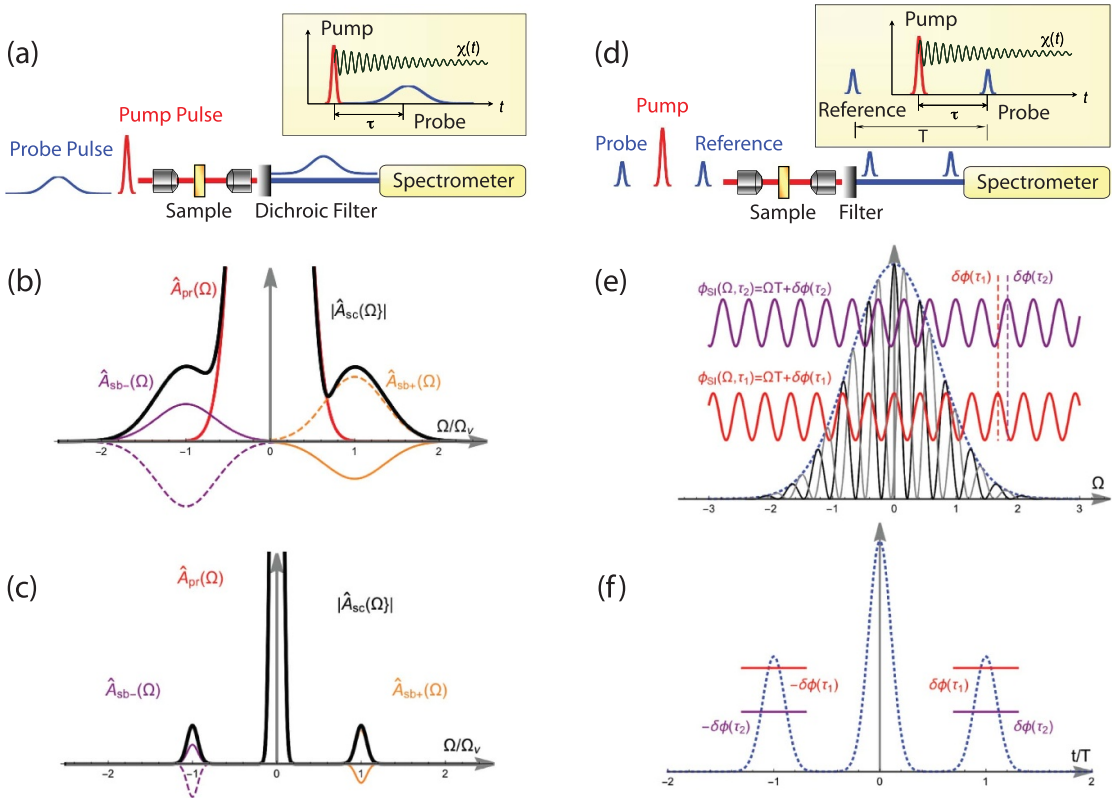

Figure 10. Two methods of spectral detection based on probe pulses that can be separated from the pump pulse by a filter (dichroic, polarization, spatial). (a) In the case of a long time-delayed probe pulse (IPS), nonresonant scattering by the probe is negligible and the spectrum can be resolved by isolating the probe pulse and sending it into a spectrometer. (b) When the probe pulse is insufficiently long, there is still partial overlap between the input probe pulse spectrum and the spectral sidebands. As the vibrational period of low frequency Raman modes is quite long, the probe pulse duration must be carefully chosen. (c) For a sufficiently long probe pulse, the spectral sidebands are well separated and the spectrum can be easily extracted. (d) In spectral interferometry (SI), a probe and reference pulse pair are sent into the Raman medium. After rejection of the pump pulse the spectral interferomgram between the probe and reference pulses is recorded (e), where the period of the spacing of spectral fringes is inversely proportional to the reference-probe pulse separation. The sinusoidal spectral phase is a combination of the linear phase ramp from the difference in pulse spacing and the Raman-induced phase shift imparted onto the probe pulse. (f) The Raman-induced phase may be extracted from the peak of the time-delay sidebands obtained form the Fourier transform of the measured spectral data.

5.1. Long and distinguishable probe pulse (IPS)

The forced Raman spectrum can be easily recorded with use of a long probe pulse that can be separated from the pump pulse when the probe pulse, or its scattered spectral content, is not spectrally overlapped with the pump [56, 57, 59, 69, 98, 99]. As illustrated in figure 10(a), the probe pulse can be isolated with a filter and then directed into a spectrometer. Other methods of probe isolation include the introduction of a narrow spectral phase perturbation [100] or the creation of orthogonally polarized probe pulse [71] that can be isolated with polarization optics. When the probe pulse arrives at a time delay after the short impulsive pump pulse, the spectrum is considerably simplified when we have a long pulse, taking for form of equation (58). Cross phase modulation from nonresonant scattering is eliminated because the probe pulse does not overlap in time with the pump. However, excited forced Raman vibrations apply a sinusoidal phase modulation that oscillates over many vibrational periods across the probe pulse temporal profile. If the probe pulse duration is not sufficiently long, the separation of the spectral sidebands from the incident probe spectrum is incomplete, as illustrated in figure 10(b). However, for a long enough pulse, e.g. $\tau_{pr} \sim 4\,\tau_{pu}$ or larger, the energy is scattered from the narrow input spectrum and scattered to sidebands shifted by the vibrational frequency is well-isolated from the input spectrum (see figure 10(c)). The lack of interference produces a clean Raman spectrum that is determined by the imaginary portion of the third-order Raman susceptibility, and thus is quite easy to interpret from these isolated probe pulse spectra (IPS).

To estimate the SNR, we assume that we detect the full scattered sideband spectrum on a single pixel of the spectrometer. The probe power scattered by the sinusoidal temporal phase grating is the same as the power scattered by the transient sinusoidal spatial phase grating, including the spectrometer efficiency, η_s, we obtain a sideband signal power of $\bar{p}_{sig} = \eta_s\,(\delta\phi_0^v/2)^2\,\bar{p}_{pr}$. IPS is the spectral scattering analog to TG, where we are able to detect the isolated scattering from a sinusoidal phase modulation applied to the probe pulse. Again

the total power detected is this scattered power, which is also the background power. As a result, the peak SNR factor in the shot noise limit is $W_{\mathrm{IPS}} = \sqrt{\eta_s}/2$. Whereas when RIN limits the SNR, the SNR factor is $Y_{\mathrm{IPS}} = 1$.

Assuming a spectrometer efficiency of 80% and that the spectral resolution matches the probe pulse spectral width, using the example parameters in the shot noise limit, we obtain quantitative values of $\kappa_{\mathrm{IPS}} \sim 1.01 \times 10^6 \sqrt{\mathrm{Hz}}$ and $\kappa_{\mathrm{IPS}} \sim 53.4 \sqrt{\mathrm{Hz}}$ for neat and 1 mM acetonitrile, respectively. These cases require $\Delta t_{\mathrm{IPS}} \sim 8.85$ ps and $\Delta t_{\mathrm{IPS}} \sim 3.16$ ms to attain an SNR value of 3. However, attaining the shot noise limit will be difficult due to the limited integration time of the spectrometer. As a result, the RIN in the measurement will be contributed from low offset frequencies and thereby be subject to a high value of RIN. Assuming a RIN of $\sigma_{\mathrm{RIN}} = -110$ dBc HZ^{-1}, the SNR coefficients drop to $\kappa_{\mathrm{IPS}} \sim 1.81 \times 10^4 \sqrt{\mathrm{Hz}}$ and $\kappa_{\mathrm{IPS}} \sim 1 \sqrt{\mathrm{Hz}}$ for neat and 1 mM acetonitrile, respectively

5.2. Probe spectral interferometry (SI)

A notable exception to the aforementioned moratorium on the use of a short probe pulse of the frequency-domain detection of coherent Raman spectrum is to use SI [43, 49, 59, 78, 79]. In a SI experiment, a reference pulse is sent into the specimen along with a probe pulse; this experimental setup is illustrated in figure 10(d). Each of these pulses is temporally short, generally roughly the same duration as the pump pulse and with intensity and energy lower than the pump pulse so as not to perturb the excited vibrations. The short temporal duration allows the pulses to directly probe the phase shift induced by the forced Raman response. The recorded spectrum produces a spectral interferomgram that is shown in figure 10(e). The periodic modulation across the spectrum (period of $2\pi/T$) arises from a sinusoidal phase that scales with the probe-reference pulse temporal separation, T. The sinusoidal spectral phase translates when the relative phase of the probe and reference pulses changes. As the reference pulse arrives before the probe, the phase difference is simply the perturbation induced to due to the forced Raman response. Nonresonant scattering is avoided due to lack of time overlap with the pump pulse. The phase is extracted from the mean phase at the time-delay sidebands obtained by Fourier transforming the SI data (figure 10(f)).

To record Raman spectrum, the arrival time of the probe-reference pulse pair is scanned with respect to the pump pulse in order to record the phase difference imparted due to the impulsive Raman excitation by the pump pulse. This SI approach offers a favorable strategy for low-frequency Raman detection because the time-varying perturbation of the effective optical susceptibility is directly probed, which offers a substantial advantage for low frequency Raman signals. The SNR can be improved by the use of chirped pump and probe pulses to both reduce the nonresonant background and isolate the signal from residual noise [49].

In SI measurements, the probe-reference pulse pair is sent into a spectrometer. Assuming a spectrometer detection efficiency of η_s and the fraction of the power on a single detector array with a spectral width of $\Delta\Omega = 2\pi\Delta\nu$ is $\eta_{\mathrm{pixel}} = \Delta\Omega S(\Omega)/\int S(\Omega) d\Omega$. For Gaussian pulse $u(t) = \exp(-t^2/\tau_p^2)$, this pixel efficiency is $\eta_{\mathrm{pixel}} = \sqrt{2}\Delta\nu\tau_p$. The estimated signal power on a single pixel is $p_{\mathrm{sig}} = \delta\phi_0^{\nu}\bar{p}_{\mathrm{bkg}}$, is proportional to the background power, $\bar{p}_{\mathrm{bkg}} = \eta_s\eta_{\mathrm{pixel}}\bar{p}_{\mathrm{pr}}$, that dominates the shot noise. The shot noise varies across the recorded spectral interferogram, which makes the extracted phase SNR vary across the spectrum.

A more favorable strategy for extracting the phase from spectral interferometry is to take the phase of the time-delayed sidebands after performing an inverse fast Fourier transform. The phase is extracted from the arc tangent of the ratio of the imaginary and real components of the peak time-delayed sidebands, with the mean value of $\delta\phi_0^{\nu}$. The standard deviation of the phase fluctuations is given by $\sigma_{\delta\phi} = (W_{\mathrm{SI}}\Upsilon_{\mathrm{pr}}\sqrt{\Delta t})^{-1}$, where the SNR weighting factor in the shot noise limit is $W_{\mathrm{SI}} = \sqrt{2\pi\eta_s}$. Making use of the shot noise limited phase and phase noise variance estimates, we obtain the peak SNR relationship of the same form as equation (62). In the RIN limit, we find that $Y_{\mathrm{RIN}} = 1$.

Assuming a spectrometer efficiency of 80% and a spectral resolution of $\Delta\lambda = 0.4$ nm, which corresponds to $\Delta\nu \sim 0.12$ THz or, equivalently $\Delta\nu \sim 4\ \mathrm{cm}^{-1}$, the spectral interferometry weighting factor then reads $W_{\mathrm{SI}} \sim 2.24$. Combining this with the example parameters leads to quantitative values in the shot noise limit of $\kappa_{\mathrm{SI}} \sim 5.01 \times 10^6 \sqrt{\mathrm{Hz}}$ and $\kappa_{\mathrm{SI}} \sim 267 \sqrt{\mathrm{Hz}}$ for neat and 1 mM acetonitrile, respectively. These cases require $\Delta t_{\mathrm{SI}} \sim 0.352$ ps and $\Delta t_{\mathrm{SI}} \sim 0.126$ ms to attain an SNR value of 3. Unfortunately the slow integration time of spectrometers prevents the direct access to this shot noise limit and with spectrometer detection, the relatively high RIN leads to $\kappa_{\mathrm{SI}} \sim 1.81 \times 10^4 \sqrt{\mathrm{Hz}}$ and $\kappa_{\mathrm{SI}} \sim 1 \sqrt{\mathrm{Hz}}$ for neat and 1 mM acetonitrile, respectively

5.3. Single pulse with pulse shaping for probe selection (SPi, SPn)

An elegant strategy for producing a long probe pulse is to directly carve that probe pulse out of the impulsive pump pulse [70]. Multiple strategies have been developed to produce this long probe pulse through amplitude or phase spectral shaping [70, 101], polarization shaping [71], or with resonant optical filters [26, 102, 103]. In these configurations, we may write the reshaped pump pulse as a superposition of the

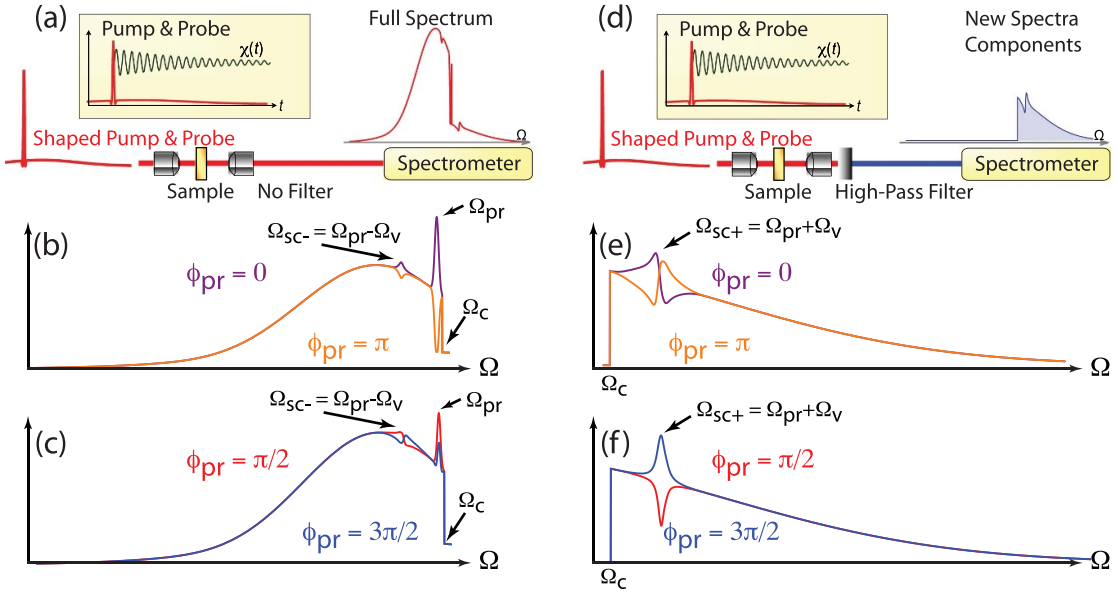

Figure 11. The probe pulse can be obtained by shaping the pump pulse to create a combination of a short pump pulse for impulsive Raman excitation as well as a long probe pulse to probe the forced Raman response with high spectral resolution. The challenge is then obtaining a Raman spectrum from the scattered spectrum. The spectral overlap of the input pulse spectrum, the Raman scattering, and the nonresonant scattering leads to a rich set of experimental strategies. To facilitate the extraction of the Raman spectrum, the high frequencies of the shaped pump pulse spectral field are clipped with a low-pass filter. In addition, we note that the Raman scattered spectral field is in phase with the nonresonant scattered spectrum, whereas the scattered Raman spectrum is in quadrature with the input spectrum. As a result, the positive sideband interferes with the nonresonant spectrum—enabling access to the real part of the complex Raman susceptibility, whereas the negative sideband interferes with the input pulse spectrum, revealing the imaginary portion of spectrum. The relative phase of the probe, $\phi_{\rm pr}$, may be manipulated to change this interference. These spectral differences can be seen in spectral inset in (a). Two measurement strategies are possible: (a)–(c) measure the interference with the input spectrum (SPi) and (d)–(f) measure the new scattered frequencies above the input spectrum cutoff (SPn). (a) In an experiment measuring the interference between the input spectrum the scattered spectrum, the interference is dominated by the Raman scattering of the input pulse, as the nonresonant scattering of the pump is much weaker than the input pulse spectrum. By contrast, when the probe pulse is in ($\phi_{\rm pr} = 0$) or out ($\phi_{\rm pr} = \pi$) of phase with the pump pulse, the magnitude of the imaginary part of the Raman susceptibility is added to or subtracted from the input pulse spectrum (b). By contrast, when the probe phase is in quadrature ($\phi_{\rm pr} = \pi/3, 2\pi/2$), the real (dispersive) part of the Raman susceptibility is added to or subtracted from the input spectrum (c). The newly generated spectra (coherent anti-Stokes Raman scattering, CARS) can be isolated from the input spectrum with a high pass optical filter that is complementary to the low pass cufoff frequency filter (d). This CARS spectrum is complementary to the spectrum that interferes with the input spectrum. Here, however, the scattered Raman sideband interferes with the nonresonant scattering from the pump pulse, leading to the emergence of the real part of $\chi^{(3),\rm VR}(\Omega)$ when ($\phi_{\rm pr} = 0, \pi$) as shown in (e) and the imaginary part of $\chi^{(3),\rm VR}(\Omega)$ when ($\phi_{\rm pr} = \pi/3, 2\pi/2$) as shown in (f).

unperturbed pump pulse and long probe pulse. As it is not possible to separate the pump and probe pulses with dichroic optics, the spectrum contains the full compliment of terms expressed in equation (76).

The temporally short (broad spectrum) pump probe pulse is negligibly perturbed by the removal of the temporally long long (spectrally narrow) probe pulse from the pump pulse spectral bandwidth [70, 71]. Part of the pump pulse is spectrally broadened due to scattering by the nonresonant temporal phase modulation. Some of the probe pulse energy is scattered to narrow spectral sidebands as a result of the fact that the long temporal pulse overlaps with many oscillations of the sinusoidal Raman phase modulation, as illustrated in figure 11. Moreover, the relative phase between the pump and probe pulses may be altered with an ultrafast pulse shaper [70, 101] allowing control over interference between spectral scattering from the probe pulse and the input pump pulse spectrum and the pump pulse spectrum scattered by the nonresonant response.

To derive analytic expressions, we assume that we have transform-limited Gaussian pump pulses with an average power of $\bar{p}_{\rm pu}$ and a pulse duration of $\tau_{\rm pu}$ with the temporal envelope of $u_{\rm pu}(t) = \exp(-(t/\tau_{\rm pu})^2)$. The spectral amplitude of the field of this pulse is $\hat{A}_{\rm pu}(\Omega) = A_{0,\rm pu}\sqrt{\pi}\,\tau_{\rm pu}\exp(-(\tau_{\rm pu}\,\Omega/2)^2)$, so that a probe pulse extracted from a center frequency of $\Omega_{\rm pr}$ with have a peak spectral amplitude of $\hat{A}_{\rm pu}(\Omega_{\rm pr})$. Assuming that the probe pulse is also Gaussian with a pulse duration of $\tau_{\rm pr}$, then the average power of the probe pulse is $\bar{p}_{\rm pr} = (\tau_{\rm pr}/\tau_{\rm pu})\,\exp(-(\tau_{\rm pu}\,\Omega_{\rm pr}/2)^2)\bar{p}_{\rm pu}$.

We consider two cases for signal generation, where the probe pulse spectral scattering either interferes with the input probe pulse spectrum (SPi, figures 11 (a)–(c)) or with new generated nonresonant scattered spectrum in a region where the input pump pulse has been clipped with a spectral filter (SPn, figures 11 (d)–(f)). In the first case, the pump and probe spectral components are in quadrature, and thus a $\pi/2$ phase shift is required for them to interfere with the input pump pulse spectrum at the scattered frequency $\Omega_{\rm sc\pm} = \Omega_{\rm pr} \pm \Omega_v$ [70]. In the second case, the spectrum of only newly scattered spectral components need be

considered, and thus the probe pulse scattered to the vibrational sideband interferes with the nonresonantly scattered pump pulse. As both scattering processes impart a $\pi/2$ phase shift, these signals interfere without modification of the relative phases.

To estimate the SNR, we assume that the spectrometer resolution matches the probe pulse spectrum and that we have a spectrometer efficiency of η_s. With these assumptions, in the first detection scenario (self interference with the input pump pulse spectrum, i.e. SPi), we obtain an average background power of $\bar{p}_{\rm bkg} = \eta_s(\tau_{\rm pu}/\tau_{\rm pu})\exp(-(\tau_{\rm pu}\,\Omega_{\rm sc\pm})^2/2)$ directly from the input pump pulse. The input pulse spectrum acts as a strong reference field that boosts the signal, leading to an input signal average power of $\bar{p}_{\rm sig} = \eta_s(\tau_{\rm pu}/\tau_{\rm pu})\,\delta\phi_0^{\nu}\exp(-(\tau_{\rm pu}\,\Omega_{\rm pr}/2)^2)\exp(-(\tau_{\rm pu}\,\Omega_{\rm sc\pm}/2)^2)$.

Similarly, for the second scenario, where we only admit newly scattered spectral contents into the measurement, i.e. SPn, and the power scattered into the CARS spectral band contains contributions from nonresonant electronic and vibrational scattering. The total scattered power into this spectral band serves as the background power,

$$\bar{p}_{\rm CARS} \approx \frac{\eta_s}{3}(\delta\phi_0^{\rm nr})^2\frac{\tau_{\rm pu}}{\tau_{\rm pr}}\left(e^{-\frac{2}{3}(\frac{1}{2}\tau_{\rm pu}\,\Omega_{\rm sc\pm})^2} + \sqrt{3}\,r\,e^{-(\frac{1}{2}\tau_{\rm pu}\,\Omega_{\rm pr})^2}\,e^{-\frac{1}{3}(\frac{1}{2}\tau_{\rm pu}\,\Omega_{\rm sc\pm})^2} + \frac{3}{4}r^2\,e^{-2(\frac{1}{2}\tau_{\rm pu}\,\Omega_{\rm pr})^2}\right)\bar{p}_{\rm pu}, \quad (79)$$

where we again use the ratio $r = \delta\phi_0^{\nu}/\delta\phi_0^{\rm nr}$. Generally, in experiments, $r \ll 1$, so that we may approximate our background power as

$$\bar{p}_{\rm bkg} \approx \frac{\eta_s}{3}(\delta\phi_0^{\rm nr})^2\frac{\tau_{\rm pu}}{\tau_{\rm pr}}\,e^{-\frac{2}{3}(\frac{1}{2}\tau_{\rm pu}\,\Omega_{\rm sc\pm})^2}\,\bar{p}_{\rm pu}. \quad (80)$$

The signal power is dominated by the middle term,

$$\bar{p}_{\rm sig} = \sqrt{\frac{1}{3}}\,\eta_s(\tau_{\rm pu}/\tau_{\rm pu})\,\delta\phi_0^{\nu}\,\delta\phi_0^{\rm nr}\,e^{-(\frac{1}{2}\tau_{\rm pu}\,\Omega_{\rm pr})^2}\,e^{-\frac{1}{3}(\frac{1}{2}\tau_{\rm pu}\,\Omega_{\rm sc\pm})^2}\,\bar{p}_{\rm pu}. \quad (81)$$

Remarkably in the shot noise limit, the homodyne detection in both scenarios (SPi and SPn) leads to an identical expression for the SNR, with an SNR weighting factor for SP detection becomes $W_{\rm SP} = \sqrt{\eta_s\tau_{\rm pu}/\tau_{\rm pr}}\exp(-(\tau_{\rm pu}\,\Omega_{\rm pr}/2)^2)$. In the RIN limit, however, the SNR factors are distinct for the two cases. When the scattered probe spectrum interferes with the input probe spectrum, the RIN-limited SNR weight for SPi is $Y_{\rm RIN} = \exp(-(\tau_{\rm pu}\,\Omega_{\rm pr}/2)^2)\exp(-(\tau_{\rm pu}\,\Omega_{\rm sc\pm}/2)^2)$. In contrast, when the scattered probe field interferes with the nonresonant scattering, all at new spectral components above the low pass filter cutoff, then the SNR weight for SPn is $Y_{\rm RIN} = (\sqrt{3}/\delta\phi_0^{\rm nr})\exp(-(\tau_{\rm pu}\,\Omega_{\rm pr}/2)^2)\exp((\tau_{\rm pu}\,\Omega_{\rm sc\pm}/2)^2/3)$.

With a spectrometer efficiency of 80 % and a probe pulse spectral width of $\Delta\nu \sim 1.2$ THz, which corresponds to a probe pulse duration of $\tau_{\rm pr} \sim 2.6$ ps, the single pulse CARS weighting factor evaluates to $W_{\rm SP} \sim 0.072$. Then, using the example parameters, in the shot noise limit we obtain quantitative values of $\kappa_{\rm SP} \sim 1.62\ \times 10^5\sqrt{\rm Hz}$ and $\kappa_{\rm SP} \sim 8.60\sqrt{\rm Hz}$ for neat and 1 mM acetonitrile, respectively. These cases require $\Delta t_{\rm SP} \sim 341$ ps and $\Delta t_{\rm SP} \sim 122$ ms to attain an SNR value of 3.

In the RIN limit, there is a clear advantage for the new (CARS) spectral detection. Again, assuming that the probe is derived from the center of the pulse spectrum ($\Omega_{\rm pr} = 0$) and a RIN value of $\sigma_{\rm RIN} = -120$ dBc Hz^{-1}, the values of the RIN weighting coefficient are $Y_{\rm RIN} = 8.77$ and $Y_{\rm RIN} = 33.8$ for SPi and SPn, respectively. This leads to SNR coefficients for the signal derived from interference with the input pump pulse spectrum, SPi, of $\kappa_{\rm SPi} \sim 1.58\ \times 10^5\sqrt{\rm Hz}$ and $\kappa_{\rm SPi} \sim 8.38\sqrt{\rm Hz}$ for neat and 1 mM acetonitrile, respectively. Whereas for the CARS spectrum obtained completely from newly scattered spectral components, the SNR coefficients are $\kappa_{\rm SPn} \sim 6.11\ \times 10^5\sqrt{\rm Hz}$ and $\kappa_{\rm SPi} \sim 32.3\sqrt{\rm Hz}$. The nonresonant background that distorts the recovered Raman spectrum can be reduced by using a chirped pulses from which a single or double narrow spectral notch is removed, enabling improved signal-to-noise on the Raman contrast [23, 26].

5.4. SNR for stimulated Raman scattering (SRS)

To further put these low-frequency Raman spectroscopy techniques into perspective we now consider stimulated Raman spectroscopy [104]. As noted earlier, SRS spectroscopy relies on two separate pulses, pump and Stokes, that exhibit no spectral overlap. When used for coherent Raman spectroscopy, these two pulses are detuned so that their frequency difference matches the vibrational frequency that we wish to excite, $\Delta_{\rm pu} = \Omega_{\nu}$. Under these conditions the beat frequency between these pulses drives a strong forced Raman response as shown in figure 4. Generally, the pulse durations are set to be long enough that the third order nonlinear susceptibility is approximately constant across the vibrational resonance.

For purposes of a calculation, we consider pump and Stokes pulses with a duration of $\tau_{\rm SRS}$ that are longer than the vibrational lifetime, which implies that we meet the criterion $\tau_{\rm SRS}\,\Gamma_{\nu} \gg 1$. Under these conditions,

we may approximate the forced Raman response driven by the beating between the pump and Stokes pulses as

$$\tilde{F}_R(\omega) \approx \frac{i}{2}\chi^{(3),\mathrm{v,mn}}_{ijkl}(\Omega_v)\left[e^{(\tau_{\mathrm{SRS}}[\omega+\Omega_v]/2)^2/2} - e^{(\tau_{\mathrm{SRS}}[\omega-\Omega_v]/2)^2/2}\right]. \tag{82}$$

The time domain forced Raman response for SRS is then

$$f_R(t) \approx \frac{2}{\pi\,\tau_{\mathrm{SRS}}}\chi^{(3),\mathrm{v,mn}}_{ijkl}(\Omega_v)\,e^{-2(t/\tau_{\mathrm{SRS}})^2}\,\sin(\Omega_v t), \tag{83}$$

from which we extract the peak SRS phase shift of

$$\delta\phi_0^{\mathrm{SRS}} = g_{\mathrm{pu,St}} f_{\mathrm{R,SRS,max}}\bar{p}_{\mathrm{pu}}, \tag{84}$$

where

$$f_{\mathrm{R,SRS,max}} = \frac{2}{\pi\,\tau_{\mathrm{SRS}}}\chi^{(3),\mathrm{v,mn}}_{ijkl}(\Omega_v). \tag{85}$$

By inspection, we may relate the SRS peak forced Raman phase shift, that leads to spectral scattering and thereby produces stimulated Raman loss and gain, to the ISRS phase shift. This produces the relationship

$$\delta\phi_0^{\mathrm{SRS}} = \frac{2}{\pi}\frac{1}{\tilde{D}(\Omega_v,\tau_p)}\frac{1}{\tau_{\mathrm{SRS}}\,\Gamma_v}\delta\phi_0^{v}. \tag{86}$$

With the peak phase shift for SRS related to the ISRS peak phase shift, we are in a position to directly compare the SNR for SRS spectroscopic detection to ISRS methods that we discussed in previous sections. We find that the SNR coefficient for SRS in the stimulated Raman gain case is $\kappa_{\mathrm{SRS}} = W_{\mathrm{SRS}}\,\delta\phi_0^{v}\,\Upsilon_{\mathrm{SH,St}}$, where the subscript $j = \mathrm{St}$ means that we use the Stokes power in $\Upsilon_{\mathrm{SH,j}}$. The weighting factor for SRS detection is $W_{\mathrm{SRS}} = \left(\tilde{D}(\Omega_v,\tau_p)\,\tau_{\mathrm{SRS}}\,\Gamma_v\right)^{-1}$. In the RIN limit, $Y_{\mathrm{SRS}} = \left(\tilde{D}(\Omega_v,\tau_p)\,\tau_{\mathrm{SRS}}\,\Gamma_v\right)^{-1}$.

Assuming a pump and Stokes pulse duration of $\tau_{\mathrm{SRS}} = 6$ ps, then the SRS weighting factor is $W_{\mathrm{SRS}} \sim 0.655$. Then, using the example parameters, in the shot noisei limit, we obtain quantitative values of $\kappa_{\mathrm{SRS}} \sim 1.48\ \times 10^6\sqrt{\mathrm{Hz}}$ and $\kappa_{\mathrm{SRS}} \sim 78\sqrt{\mathrm{Hz}}$ for neat and 1 mM acetonitrile, respectively. These cases require $\Delta t_{\mathrm{SRS}} \sim 4.13$ ps and $\Delta t_{\mathrm{SRS}} \sim 1.48$ ms to attain an SNR value of 3. In the RIN limit, the SRN factor SRS becomes $Y_{\mathrm{SRS}} = W_{\mathrm{SRS}}$. However, even for a relatively low value of RIN, $\sigma_{\mathrm{RIN}} = -150$ dBc Hz^{-1}, the SNR coefficients drop to $\kappa_{\mathrm{SRS}} \sim 3.74\ \times 10^5\sqrt{\mathrm{Hz}}$ and $\kappa_{\mathrm{SRS}} \sim 19.8\sqrt{\mathrm{Hz}}$ for neat and 1 mM acetonitrile, respectively.

SRS is commonly used for relatively high vibrational frequencies. Here, we see that as compared to many of the ISRS-based methods, SRS will perform better at higher frequencies due to the $\tilde{D}(\omega)$ term in the denominator of the SNR coefficient in ISRS. Moreover, performing SRS spectroscopy requires stable and tunable ps duration laser pulses, which are less common that stable fs laser pulse oscillators.

6. Discussion

The fact that all coherent Raman techniques can be described in the context of the coherent phase modulation that is driven by the forced Raman response that leads to spectral scattering permits facile comparison of the quantitative detection capabilities of these methods. In this review, we focus our discussion on the dependence of the signal and the SNR on the detected vibrational frequency. The signal power dependence on impulsive Raman excitation, $\delta\phi_0^2$, the vibrational frequency, Ω_v, for the optimal experimental configuration is summarized in table 1. Then representative relative values of the SNR in the shot noise limit for single pixel detection is shown in table 2 and for detection with a spectrometer in the RIN limit in table 3.

Our interest here is particularly concerned with the spectroscopy of low frequency vibrational modes. As a result, we consider solely impulsive Raman excitation for driving the forced Raman response. This produces a peak phase modulation of $\delta\phi_0^{v}$, with a relative excitation efficiency for Raman vibrational modes of $D(\Omega_v) = \exp\left[-(\tau_p\,\Omega_v/2)^2/2\right]$. The vibrational frequency dependence of impulse Raman excitation establishes the maximum frequency that may be efficiently excited in the ISRS scattering processes. The vibrational frequency dependence and the relevant highest (cutfoff) vibrational frequency are considered for each technique are summarized in table 1, and we consider each technique in the list. However, the filtering of coherent excitation that produces the signal power is not uniform among the detection modes and it is important to consider separately both the signal and the signal-to-noise ratio (SNR).

Table 1. Comparison of the experimental modalities (modes) with the signal power (or strength) and the dependence of that signal on the vibrational frequency Ω_v and the molecular concentration, N. We note that dependence of the peak forced Raman response phase modulation is $\delta\phi_0^v \propto \exp[-(\tau_p\Omega_v/2)^2/2]$. The cutoff vibrational frequency is also given for each mode where the signal strength is equal to the impulsive excitation efficiency for a pulse duration with $\tau_p = 3\ T_v/4$. The modes are described in detail in the text, and we use the following labels: TG = transient grating, INT = interferometric, KL = Kerr lens, KS = Kerr steering, $\delta\omega$ = frequency shift, RF = radio frequency detection of the frequency shift, FT = Fourier transform or single pulse CARS, SI = spectral interferometry, IPS = isolated pulse spectrum, SP = single pulse (SPi and SPn), as described in the text.

Signal power dependence on Ω_v		
Mode	Signal power	Signal $\Omega_{v,\max}$
TG	$(\delta\phi_0^v/2)^2\,\bar{p}_{\rm pr} \sim N^2$	$(3\pi\sqrt{2}/4)\,\tau_p^{-1}$
INT	$\delta\phi_0^v\,\bar{p}_{\rm pr} \sim N$	$(3\pi/2)\,\tau_p^{-1}$
KL	$0.736\,\delta\phi_0^v\,\bar{p}_{\rm pr} \sim N$	$(3\pi/2)\,\tau_p^{-1}$
KS	$0.21\,\delta\phi_0^v\,\bar{p}_{\rm pr} \sim N$	$(3\pi/2)\,\tau_p^{-1}$
$\delta\omega$	$0.33\,\tau_p\,\Omega_v\,\delta\phi_0^v\,\bar{p}_{\rm pr} \sim N$	$6.05\,\tau_p^{-1}$
RF	$\Delta\tau = \varphi_2\,\Omega_v\,\delta\phi_0^v \sim N$	$6.05\,\tau_p^{-1}$
FT	$0.029\,\tau_p\,\delta\phi_0^{\rm nr}\,\Omega_v\,\delta\phi_0^v\,\bar{p}_{\rm pr} \sim N$	$6.05\,\tau_p^{-1}$
SI	$(\eta_s/2)\,\delta\phi_0^v\,\bar{p}_{\rm pr} \sim N$	$(3\pi/2)\,\tau_p^{-1}$
IPS	$\eta_s\,(\delta\phi_0^v/2)^2\,\bar{p}_{\rm pr} \sim N^2$	$(3\pi\sqrt{2}/4)\,\tau_p^{-1}$
SPi	$\eta_s\,(\tau_{\rm pu}/\tau_{\rm pr})\,\delta\phi_0^v\,e^{-(\tau_{\rm pu}\,\Omega_{\rm pr}/2)^2}\,e^{-(\tau_{\rm pu}\,\Omega_{\rm sc\pm}/2)^2}\,\bar{p}_{\rm pu} \sim N$	$(\sqrt{3}\pi/2)\,\tau_p^{-1}$
SPn	$\eta_s\,(\tau_{\rm pu}/\sqrt{3}\,\tau_{\rm pr})\,\delta\phi_0^{\rm nr}\,\delta\phi_0^v\,e^{-(\tau_{\rm pu}\,\Omega_{\rm pr}/2)^2}\,e^{-(\tau_{\rm pu}\,\Omega_{\rm sc\pm}/2)^2/3}\,\bar{p}_{\rm pu} \sim N$	$(3\pi/2)\,\sqrt{3/5}\,\tau_p^{-1}$

Table 2. SNR values in the shot noise limit for two different impulsive experimental Raman spectroscopy modes that use a single detector. Performance for vibrational frequencies of 920.5 $\rm cm^{-1}$ and 150 $\rm cm^{-1}$. A high and a low frequency vibrational mode are compared for both short pump pulse excitation ($\tau_p = 17$ fs) and long pump pulse excitation ($\tau_p = 42.5$ fs) are compared. An integration time of 10 μs is considered. The modes are described in detail in the text, and we use the following labels: TG = transient grating, INT = interferometric, KL = Kerr lens, KS = Kerr steering, $\delta\omega$ = frequency shift, RF = radio frequency detection of the frequency shift, FT = Fourier transform or single pulse CARS, SI = spectral interferometry, IPS = isolated pulse spectrum, SP = single pulse (SPi and SPn), as described in the text.

Single pixel detection: SNR = signal/noise values comparison (unitless)				
Mode	Low frequency, 150 $\rm cm^{-1}$		High frequency, 920 $\rm cm^{-1}$	
$\tau_{\rm pu}$	Short (17 fs)	Long (42.5 fs)	Short (17 fs)	Long (42.5 fs)
TG	10 300	8820	3570	11.8
INT	20 500	17 600	7130	23.6
KL	20 200	17 300	7000	23.2
KS	13 000	11 200	4530	15.0
$\delta\omega$	6270	5390	13 400	42.2
RF	55 200	41 700	40 900	0.447
FT	361	110	1820	11.5

Table 3. SNR values in the RIN limit for spectroscopic detection modes that are not able to use RIN mitigation strategies and require much longer integration times. An integration time of 1 ms is used here to compare the performance of two different impulsively excited Raman spectroscopy frequencies of 920.5 $\rm cm^{-1}$ and 150 $\rm cm^{-1}$. A high and a low frequency vibrational mode are compared for both short pump pulse excitation ($\tau_p = 17$ fs) and long pump pulse excitation ($\tau_p = 42.5$ fs) are compared. ND indicated not detected. The modes are described in detail in the text, and we use the following labels: TG = transient grating, INT = interferometric, KL = Kerr lens, KS = Kerr steering, $\delta\omega$ = frequency shift, RF = radio frequency detection of the frequency shift, FT = Fourier transform or single pulse CARS, SI = spectral interferometry, IPS = isolated pulse spectrum, SP = single pulse (SPi and SPn), as described in the text.

Spectrometer pixel detection: SNR = Signal/Noise values comparison (unitless)				
Mode	Low frequency, 150 $\rm cm^{-1}$		High frequency, 920 $\rm cm^{-1}$	
$\tau_{\rm pu}$	Short (17 fs)	Long (42.5 fs)	Short (17 fs)	Long (42.5 fs)
SI	1640	1110	1820	1.90
IPS	1640	1110	1820	1.90
SPi	1740	2025	5010	ND
SPn	27 500	65 400	19 300	ND

In addition, we will revisit our experimental example numbers, with the same Raman derived polarizability and vibrational resonance linewidth, but now considering a vibrational frequency of 150 $\rm cm^{-1}$ in addition to the 920.5 $\rm cm^{-1}$ mode of acetonitrile. We also consider the effects of a long pulse, $\tau_p = 42.5$ fs, and a short pulse, $\tau_p = 17$ fs, on the excitation efficiency. Here we obtain for the short pulse, the ISRS excitation efficiency is $\tilde{D}(150\ \rm cm^{-1}) \sim 0.972$ and $\tilde{D}(920.5\ \rm cm^{-1}) \sim 0.338$ for the low and high frequencies, respectively. These numbers drop to $\tilde{D}(150\ \rm cm^{-1}) \sim 0.835$ and $\tilde{D}(920.5\ \rm cm^{-1}) \sim 0.001$ for impulsive

excitation by the long pump pulse. Clearly, low frequency Raman spectroscopy is readily accessible even with relatively long pump pulses. The change in impulsive excitation efficiency also changes the peak forced Raman phase shift, which impacts signal generation. In the case of the 920.5 cm^{-1} mode, the peak phase shift for a neat concentration is $\delta\phi_0^v = 12.8$ mrad and $\delta\phi_0^v = 42.2\,\mu$rad, for short and long pulses, respectively. This precipitous drop does not occur for the 150 cm^{-1} mode, where the peak forced Raman phase shifts for short and long pump pulses are $\delta\phi_0^v = 36.7$ mrad and $\delta\phi_0^v = 31.6$ mrad.

The transient grating (TG) detection mode records the probe pulse power diffracted by a transient phase grating established by a pair of non-co-linear pump pulses. The power incident on the single pixel detector, $\bar{p}_{\rm TG} = (\delta\omega_0^v/2)^2\,\bar{p}_{pr}$, is proportional to the square of the peak forced Raman phase modulation amplitude, and thus the functional dependence on the vibrational frequency is determined by $[\tilde{D}^2(\Omega_v)]^2$, which reduces the cutoff frequency $\Omega_{\rm max,TG} \approx 4.71\,\tau_p^{-1}$. The cutoff frequencies for TG detection are 1040 cm^{-1} for the short (17 fs) pulse and 416 cm^{-1} for the long (42.5 fs) pulse.

The scattered powers at neat concentration to be detected are $\bar{p}_{\rm TG} \sim 0.41\,\mu$W and $\bar{p}_{\rm TG} \sim 4.46$ pW for the short and long pulses and the 920.5 cm^{-1}; the signal drop for the long pulse reflects the fact that this mode exceeds the TG cutoff frequency for the long pulse. Whereas the 150 cm^{-1} mode produces TG signal powers of $\bar{p}_{\rm TG} \sim 3.37\,\mu$W and $\bar{p}_{\rm TG} \sim 2.49\,\mu$W, respectively. The NEP for a typical detector quoted earlier means that pW power levels are readily detectable within a 10 μs integration time, so the scattered power here are readily detectable. However, the quadratic dependence of the signal on concentration N, i.e. $\bar{p}_{\rm TG} \propto N^2$, means that a drop in concentration rapidly drops the signal power out of the shot noise range, and makes low concentration detection exceedingly difficult. In the shot noise limit, the noise PSD is driven by the average incident detected power, so that the SNR scales linearly with the peak forced Raman phase, but this should not be confused with detectability. At neat concentration, the SNR is in the shot noise limit, however at a 1mM concentration, the TG signal is Johnson noise limited, with a drop in SNR on the order of 100.

By contrast, interferometric detection when the phase of the probe and reference are in quadrature, the interferometric signal power is approximately $\bar{p}_{\rm INT} \approx \delta\omega_0^v\,\bar{p}_{pr}$. As a consequence, the interferometric method is capable of detecting higher frequency vibrations than TG as the spectral dependence of the signal is linear in the impulsive excitation efficiency, $\tilde{D}(\Omega_v)$ and thus linear in molecular concentration. These differences produce significantly higher signal powers, with $\bar{p}_{\rm INT} \sim 128\,\mu$W and $\bar{p}_{\rm INT} \sim 0.422\,\mu$W for the short and long pulses and the 920.5 cm^{-1}. Whereas the 150 cm^{-1} mode produces INT signal powers of $\bar{p}_{\rm INT} \sim 367\,\mu$W and $\bar{p}_{\rm INT} \sim 316\,\mu$W, respectively. The cutoff frequencies for INT detection are 1470 cm^{-1} for the short (17 fs) pulse and 588 cm^{-1} for the long (42.5 fs) pulse. Again, the 920.5 cm^{-1} mode is very weakly excited because it is well above the cutoff frequency for the long pulse. While these powers are all well above the detector NEP limit for reasonable integration times, the background power is determined by the combined average power of the probe and reference pulse pair, the total of which is set to the average power used for single probe pulses, as in TG. As a result, the SNR is also linear in molecular concentration.

Another strategy that we have analyzed for exploiting the transient change in RI produced by the pump pulse is to take advantage of the spatially varying RI profile that acts as a lens for the probe pulse. This transient Kerr lens modifies the probe pulse propagation, and the Raman-induced changes can be converted to a change in signal power by use of a simple aperture. The model experiment for this detection mode is based on placing the aperture and detector defocused from the back focal plane of a 2f optical system to record the signal power. The signal power is produced from the fact the transmission efficiency through the aperture depends on the Raman-induced spatial phase variation accumulated by the probe pulse. Two different spatial discrimination approaches lead to KL and KS ISRS spectroscopy methods. Note that the spectrum of this method is dependent on $\delta\phi_0^v$, and thus exhibits the same cutoff frequency as the interferometric method.

For the weak phase modulation levels encountered in CRS, the KL signal power may be approximated by $\bar{p}_{\rm KL} \approx -P(a,\zeta)\,\delta\omega_0^v\,\bar{p}_{\rm pr}$, with $P(a,\zeta) = 8\zeta\,a^2\exp(-2\,a^2)/(1+\zeta^2)$, and for which the optimum SNR value occurs when $a = 0.57$ and $|\zeta| = 1$. Under this condition, the signal power is $\bar{p}_{\rm KL} \approx -0.736\,\delta\omega_0^v\,\bar{p}_{\rm pr}$. This signal rides on a large background power that passes through the aperture then $\delta\omega_0^v = 0$, given by $\bar{p}_{\rm bkg} = \eta_{\delta\phi_0^v=0}(a)\,\bar{p}_{\rm pr}$, and where $\eta_{\delta\phi_0^v=0}(a) = 1-\exp(-2\,a^2)$. For our example experimental conditions, the background power is $\bar{p}_{\rm bkg} \sim 4.74$ mW, or roughly half of the incident probe power. This background power is larger than the signal powers of with $\bar{p}_{\rm KL} \sim 86.3\,\mu$W and $\bar{p}_{\rm KL} \sim 0.285\,\mu$W for the short and long pulses at the 920.5 cm^{-1} mode, and powers for the 150 cm^{-1} mode of $\bar{p}_{\rm KL} \sim 248\,\mu$W and $\bar{p}_{\rm KL} \sim 213\,\mu$W, for the short and long pump pulse, respectively. Similar to the interferometric method, KL is dominated by shot noise or RIN, and in either case, the SNR is also linear in molecular concentration.

KS exploits the spatial variation of the Raman-induced phase is to displace the pump and probe beams spatially so that the probe pulse is propagating along the edge of the pump beam. This scenario imparts an approximately linear phase ramp across the probe pulse beam. Using the same 2f optical system as with KL, the probe beam is now steered by the excited phase perturbation, and thus we call this KS. In the experiment,

a knife edge, rather than an iris is used to convert the steering of the probe beam into a signal power. The signal power is approximately linear in the phase perturbation, where it is given by $\bar{p}_{\mathrm{KS}} \approx P(b)\,\delta\phi_0^{\nu}\bar{p}_{\mathrm{pr}}$, where $P(b)$ for KS was defined earlier. As with KL, these signal powers ride a rather large background power, which in this case is $\bar{p}_{\mathrm{bkg}} \sim 8.72$ mW. For the b parameter yielding the optimal SNR, the signal powers for our example experimental conditions are $\bar{p}_{\mathrm{KL}} \sim 26.8\,\mu$W and $\bar{p}_{\mathrm{KL}} \sim 88.6$ nW for the short and long pulses and the 920.5 cm^{-1} and powers for the 150 cm^{-1} mode of $\bar{p}_{\mathrm{KS}} \sim 77.0\,\mu$W and $\bar{p}_{\mathrm{KL}} \sim 66.2\,\mu$W, for the short and long pump pulse, respectively.

The next class of detection modes are based on single pixel detection, that is a total power measurement, for the probe signal that has passed through a spectral filter ($\delta\omega$ and FT-CARS), or some other method of spectral discrimination as is employed in RF Doppler Raman. For the spectral filter, we consider a high pass filter that transmits probe pulse spectral components above a cutoff spectral frequency, Ω_c. We will consider normalized versions of this cutoff frequency, $x_c = \tau_p\,\Omega_c$. These methods detect modulations of transmitted probe power that are dominated by the anti-Stokes scattering from the time-domain phase modulation that gives rise to a shift in the COM of the probe spectrum. All of these detection modes suppress low frequency Raman detection, but are still subject to the limitations of impulsive excitation, and thus are best for mid-band vibrational frequencies.

In the case of a frequency shift detection, we rely on a probe pulse that can be isolated from the pump pulse. This isolated pulse is passed through a high pass spectral filter to convert shifts in spectral COM into a change in probe pulse power. As in the case of KS, the fluctuations in power transmitted through the spectral filter ride a large background power that serves as the dominant contributor to the noise. This background power is $\bar{p}_{\mathrm{bkg}} = \eta_{\delta\phi_0^{\nu}=0}(x_c)\,\bar{p}_{\mathrm{pr}}$, where $\eta_{\delta\phi_0^{\nu}=0}(x_c) = [1 + \mathrm{erf}(x_c/\sqrt{2})]/2$. The SNR is optimized for $x_c \sim -0.6$ For our example experimental parameters, the background power is $\bar{p}_{\mathrm{bkg}} \sim 2.74$ mW. The dependence on the vibrational frequency is quite evident in the signal power levels, scaling with $\bar{p}_{\mathrm{sig}} \approx 0.33\,\tau_p\,\Omega_{\nu}\,\delta\phi_0^{\nu}\bar{p}_{\mathrm{pr}}$. With our example experimental conditions are $\bar{p}_{\delta\omega} \sim 125\,\mu$W and $\bar{p}_{\delta\omega} \sim 415$ nW for the short and long pulses and the 920.5 cm^{-1} and powers for the 150 cm^{-1} mode of $\bar{p}_{\delta\omega} \sim 58.8\,\mu$W and $\bar{p}_{\delta\omega} \sim 50.5\,\mu$W, for the short and long pump pulse, respectively. The cutoff frequencies for frequency shifting are in a spectral band because the spectral dependence follows $\Omega_{\nu}\tilde{D}(\Omega_{\nu})$. The high frequency detection cutoff frequencies are 1890 cm^{-1} for the short (17 fs) pulse and 755 cm^{-1} for the long (42.5 fs) pulse. The low cutoff frequencies are correspondingly 18 cm^{-1} for the short pulse and 7.1 cm^{-1} for the long pulse. The low cutoff frequency of the long pulse accounts for the significant signal power reduction for the 920.5 cm^{-1} mode.

The FT-CARS detection mode is distinct from these other methods discussed so far in that the probe pulse is not isolated from the pump, and they are, in-fact, one and the same. To extract a signal, the pump/probe pulse spectrum is first clipped with a low-pass spectral filter and then only new spectral content is detected through a high-pass spectral filter. The unavoidable gap between the high- and low-pass filter cutoff frequencies sets a minimum detectable vibrational frequency. In addition, the nonresonant background is more important due to the presence of the pump pulse scattered frequencies, which can be avoided in the other techniques discussed so far due to the ability to separate the probe pulse from the pump pulse with a time delay. However, the spectral filter eliminates all of the input optical power, allowing only newly generated spectral components to pass through the filter. The signal arises from interference between the vibrationally resonant scattering and the nonresonant scattering, conferring linearity in $\delta\phi_0^{\nu}$ on the signal strength. However, both nonresonant and vibrationally resonant scattered fields are weak, leading to weak scattered signal powers. Considering the example experimental conditions, we estimate signal powers of $\bar{p}_{\mathrm{FT}} \sim 635$ nW and $\bar{p}_{\mathrm{FT}} \sim 2.10$ nW for the short and long pulses and the 920.5 cm^{-1} and powers for the 150 cm^{-1} mode of $\bar{p}_{\mathrm{FT}} \sim 449$ nW and $\bar{p}_{\mathrm{FT}} \sim 386$ nW, for the short and long pump pulse, respectively. By contrast, the background power is contributed by the vibrationally resonant and nonresonant scattering, and we estimate the level at $\bar{p}_{\mathrm{bkg}} \sim 3.63\,\mu$W for the short pulse, but this drops to $\bar{p}_{\mathrm{bkg}} \sim 0.589\,\mu$W for the long pulse due to a decreases nonresonant scattering. The range of detectable frequencies for FT-CARS is the same as $\delta\omega$.

When the coherent Raman-induced frequency shift is detected by first converting the frequency shift of the pulses into a change in arrival time at a detector by means of a dispersive medium [87] then detecting the RF phase shift of a harmonic of the laser repetition rate [88], the full power of the probe pulse is used in the measurement. In addition, the RF phase shift is measured against a reference RF signal that is derived from the oscillator. In the RF phase detection electronics, signal amplitude fluctuations are largely suppressed, which largely mitigates the effects of RIN in the measurements. In this strategy, the translation of the frequency shift into a time delay affords a unique opportunity to amplify the coherent Raman signal outside of the interaction region with the molecule or analyte under interrogation. In the RF phase, the primary noise source is phase noise generated in the photodetection process. This RF phase noise power spectral density scales inversely with the RF power of the harmonic used for phase detection. As a result RF Raman

detection offers the potential of vastly improved SNR and thus a vastly improved detection of low concentration molecular species. The range of detectable frequencies for RF detection is the same as $\delta\omega$.

Now we shift our attention to methods of detection where the full spectrum is resolved. In the case of spectrally-resolved signal detection, it is normally not possible to resolve the Raman spectrum with short probe pulses. The only known exception is by making use of spectral interferometry, where the phase perturbation acquired by the probe pulse is compared to a time-delayed reference pulse. This strategy records the phase across the spectrum of the probe pulse for one time delay, and a scan of the probe arrival time relative to the pump is required to extract a spectrum. All other spectral techniques rely on a spectrally narrow probe pulse, that is correspondingly stretched in time to span many vibrational periods of the phase modulation induced by the forced Raman response. Three cases may be distinguished: (a) where the long probe pulse can be completely spectrally separated from the short pump pulse and the forced Raman response scatters spectral energy to sidebands (IPS), (b) a long probe pulse that is not distinguishable from the incident pump pulse and the scattered probe pulse energy interferes with the input pump pulse spectral field (SPi), and (c) a long probe pulse that is not distinguishable from the incident pump pulse but where only new spectral components are detected and the signal is now dominated by interference between scattered spectrum from the forced Raman response and nonresonant scattering by the pump pulse (SPn). In the latter two cases, the long probe pulse is often derived directly from the pump pulse by means of pulse shaping with a pulse shaper or optical filter.

With spectral interferometric (SI) detection of the phase, the optimal strategy is to compute the inverse discrete Fourier transform of the recorded spectral interferogram and isolate the phase from the phase of the time delay values at the probe-reference pulse pair time delay. The phase extracted from this peak sideband is based on the ratio of the imaginary and real value of these complex sidebands, and is weighted by a signal proportional to $(1/4)\,\bar{p}_{\mathrm{pr}}$ for each sideband. The noise contribution is based on the shot noise across the spectrum that depends on the incident power on each pixel, with a higher noise contribution form the high amplitude regions of the PSD. When the variance is computed for the time-delay sidebands, the variance for the shot noise is due to a background power contribution of $(1/2)\,\bar{p}_{\mathrm{pr}}$. This produces signal and background levels very similar to the interferometric case where the field interference is not spectrally resolved. The range of detectable frequencies for SI detection is the same as INT, KL, and KS.

In the case of the isolated pulse spectrum (IPS) mode, where the pump pulse is completely rejected before the long probe pulse that has been phase modulated by the forced Raman response is directed into a spectrometer, scattering pump pulse energy to sidebands. For the laser pulse train, each sideband exhibits an average power that is identical to that obtained with the transient grating mode, although in that case the scattering is due to a spatial, rather than a temporal, grating. In IPS, the scattered sideband power differs only by the efficiency of signal collection in the spectrometer, η_s. This signal power then reads $\bar{p}_{\mathrm{IPS}} = \eta_s\,(\delta\phi_0^{\nu}/2)^2\,\bar{p}_{pr}$. Because we are again observing the scattered power, rather than the field, the functional dependence on the vibrational frequency is again $[\tilde{D}^2(\Omega_v)]^2$. Assuming a spectrometer detection efficiency of 80 %, the scattered powers to be detected are $\bar{p}_{\mathrm{IPS}} \sim 0.326\,\mu$W and $\bar{p}_{\mathrm{IPS}} \sim 3.57$ pW for the short and long pulses and the 920.5 cm^{-1}. Whereas the 150 cm^{-1} mode produces IPS signal powers of $\bar{p}_{\mathrm{IPS}} \sim 2.70\,\mu$W and $\bar{p}_{\mathrm{IPS}} \sim 2.00\,\mu$W, respectively. As with TG, there is no additional background power, so that the SNR in the shot noise limit is determined by the scattered power, but that scattered power needs to be above the electronic noise levels set by the NEP of the detector, and the scaling with respect to concentration behaves in exactly the same way. The range of detectable frequencies for IPS detection is the same as TG.

Finally, we consider the cases of single pulse impulsive CRS, where the probe pulse is directly carved out of the pump pulse. This strategy can lead to a considerable simplification in experimental design, but caries with it an intrinsic tradeoff in spectral resolution and probe pulse average power. Because of the comparatively low probe power detection of the Raman spectroscopy signal relies on interference of the scattered field with either part of the input pump pulse spectral field (SPi) or newly generated spectral component (SPn) above a high pass spectral filter edge frequency that are due to the nonresonant scattering of the pump pulse. In these examples, we will assume the most favorable condition for SNR calculations, that is when the probe pulse is carved out of the pump pulse with a vibrational frequency centered on the COM of the pump pulse power spectrum, i.e. $\Omega_{\mathrm{pr}} = 0$.

The efficiency of the nonresonant background scattering depends on the pump pulse duration, with the background power given by $\bar{p}_{\mathrm{bkg,SPn}} \approx \eta_s\,(\tau_{\mathrm{pu}}/3\,\tau_{\mathrm{pr}})\,(\delta\phi_0^{\mathrm{nr}})^2\,\exp[-(2/3)(\tau_{\mathrm{pu}}\,\Omega_{\mathrm{sc}\pm}/2)^2]\,\bar{p}_{\mathrm{pu}}$. Here $\Omega_{\mathrm{sc}\pm} = \Omega_{\mathrm{pr}} \pm \Omega_v$ denotes the frequency has scattered from the probe pulse frequency, with + indicating an increase in frequency (anti-Stokes) and—a decrease in frequency (Stokes). For our long pulse example under the assumed experimental conditions, the power in a single pixel of the spectrometer detector array (matching the spectral width of the extracted probe pulse) is $\bar{p}_{\mathrm{bkg,SPn}} \sim 220$ pW for the 920.5 cm^{-1} frequency vibration and $\bar{p}_{\mathrm{bkg,SPn}} \sim 1.49\,\mu$W for the 150 cm^{-1} frequency vibration. Whereas for the short pump pulse, these powers change to $\bar{p}_{\mathrm{bkg,SPn}} \sim 45.3$ nW for 920.5 cm^{-1} and $\bar{p}_{\mathrm{bkg,SPn}} \sim 185$ nW for 150 cm^{-1}.

By contrast, the background power of the incident pump pulse for SPi detection in the spectrometer pixel at the scattered frequency is $\bar{p}_{\mathrm{bkg,SPi}} = \eta_s\,(\tau_{\mathrm{pu}}/\tau_{\mathrm{pr}})\,\exp[-2(\tau_{\mathrm{pu}}\,\Omega_{\mathrm{sc}\pm}/2)^2]\,\bar{p}_{\mathrm{pu}}$, and for the input pulse for our long and short pump pulses for our two example vibrational frequencies are $\bar{p}_{\mathrm{bkg,SPi}} \sim 4.97$ fW for 920.5 cm^{-1} and $\bar{p}_{\mathrm{bkg,SPi}} \sim 1.55$ mW for 150 cm^{-1} for the long pulse and $\bar{p}_{\mathrm{bkg,SPi}} \sim 674$ nW for 920.5 cm^{-1} and $\bar{p}_{\mathrm{bkg,SPi}} \sim 46.3\,\mu$W for 150 cm^{-1} for the short pulse.

While the background pulse power dictates the noise, the signal power appears through a mixing of the scattered probe field and the field either present in the input pump spectral field or newly scattered from nonresonant scattering. In the case of the former (SPi), the signal powers detected within the probe pulse spectral resolution for our example experimental conditions for neat aacetonitrile are $\bar{p}_{\mathrm{SPi}} \sim 75.5$ nW and $\bar{p}_{\mathrm{SPi}} \sim 168$ fW for the short and long pulses and the 920.5 cm^{-1}. Whereas the 150 cm^{-1} mode produces SPi signal powers of $\bar{p}_{\mathrm{SPi}} \sim 1.80\,\mu$W and $\bar{p}_{\mathrm{SPi}} \sim 70.3\,\mu$W, respectively. By contrast in the latter case, where we interfere with newly scattered spectral fields, the signal power within the probe pulse spectral resolution are $\bar{p}_{\mathrm{SPn}} \sim 19.6$ nW and $\bar{p}_{\mathrm{SPn}} \sim 35.4$ pW for the short and long pulses and the 920.5 cm^{-1}. Scattering to the 150 cm^{-1} mode produces SPn signal powers of $\bar{p}_{\mathrm{SPn}} \sim 0.114\,\mu$W and $\bar{p}_{\mathrm{SPn}} \sim 2.18\,\mu$W, respectively. The cutoff frequencies for SPi detection are 850 cm^{-1} for the short (17 fs) pulse and 340 cm^{-1} for the long (42.5 fs) pulse. However, the cutoff frequencies for SPn detection are 1140 cm^{-1} for the short (17 fs) pulse and 161 cm^{-1} for the long (42.5 fs) pulse.

These calculations of the signal and background powers may be used to estimate the signal and noise levels in order to identify the appropriate noise regime to estimate the SNR. We see that the signals and the noise depend on the pump and probe pulse duration and on the vibrational frequency. While the anticipated performance for a particular experimental configuration must be specifically calculated, we summarise the SNR of these methods for for a neat liquid, using the third order susceptibility parameters given earlier for the cases of low and high vibrational frequencies and short and long pump pulses. For low frequency ISRS with single pixel detection, shot-noise limited detection is achievable, and SNR values are compared for various techniques in table 2 when the integration time is set to 10 μs. The methods that detect spectra in an optical spectrometer are more suitably described by RIN limited SNR because the slow integration time of spectrometers leads to significant accumulation of RIN from low offset frequencies. Table 3 shows a comparison off RIN limited SNR values for our example experimental parameters for a 1 ms spectral integration time. In all cases, when the concentration of the target analyte drops to a sufficiently low value, the signal power will become low enough that electronic noise is also important. Detection of low concentrations is particularly challenging for those methodologies that exhibit a signal power that scales quadratically with the concentration.

7. Conclusions

In this review, we have revisited the fundamental physics of CRS, with an emphasis on the potential for CRS methods to be applied to the rapidly emerging field of low frequency (terahertz-band) Raman spectroscopy. This low frequency band of Raman spectroscopy is expected to provide powerful new insights into problems such as understanding local material properties, protein folding and interactions, as well as for detection and identification of pathogens.

Low frequency Raman vibrations exhibit vibrational energies that are commensurate or lower than thermal energy, and thus multiple vibrational levels may be occupied under thermal equilibrium conditions at room temperature. The effects of this distribution of initially occupied vibrational levels can be effectively modeled with a mixed state treatment of the semiclassical optical response. The mixed state distribution of the forced Raman response is striking in gas phase species, where in the case of the rotational Raman effect, rotational wavepackets the dephase and exhibit periodic revivals may be observed [56]. The rephasing of these wavepackets requires that the coherently excited Raman modes do not dephase too quickly. In the gas phase, vibrational wavepackets may exhibit complex dynamics due to the fact that the system is underdamped [67]. However, in the case of liquid or solid phase systems, it is more common for the systems to be overdamped, so that the excited vibrational wavepackets dephase long before wavepacket revivals may be observed.

Low frequency Raman vibrations are readily excited with a short laser pulse, yet the broad spectral bandwidth of short pulses do not immediately allow for high resolution spectroscopy. Many methods have been developed to enable high spectral resolution using short laser pulses. In all cases, the signals arise from spectral scattering due to a combination of the temporal phase modulation from the forced Raman response and nonresonant scattering. We review these aspects of phase modulation for signal generation and compute expressions for the signal-to-noise ratio (SNR) for all of these methods. While the optimal experimental method depends on the experimental goals, some clear trends have emerged. For high frequency vibrational mode detection it is clear that short laser pulses are required for ISRS, and two detuned pulses for SRS and

CARS are also favorable. The ISRS methods considered here are quite similar in SNR for high molecular concentrations, however, the techniques that rely only on detecting the total scattered power (TG, IPS) that does not interfere with a local oscillator derived either from an input field or nonresonant scattering, exhibit a precipitous drop in SNR with reduced concentration.

In contrast, when the goal is to detect low frequency Raman modes, there is not a strong preference for short or long pump pulses for many methods, but some methods display a clear advantage for longer pump pulses for LF-CRS. Methods, such as FT- and SP-CARS and methods for the detection of a frequency shift, the detection of low-frequency vibrations is suppressed. This suppression of low frequency modes is not evident in methods that directly probe the perturbation to the RI changes, and thus these methods are better suited for the detection of low frequency Raman modes.

Finally we stress that the SNR values provided here are numerical values are all for a fixed integration time and concentration. However for low signal power levels, electronic noise will become important, and SNR values will decrease. In addition the ability to use either balanced detection, a lock-in amplifier for modulation transfer, or both has a large impact of the influence of relative intensity noise from the laser sources. As a practical matter, time domain methods required temporal scanning, which can become complex for high speed delay scanning systems. With spectrometer detection, longer integration times are generally possible, making RIN the most likely dominant noise contribution. In addition, we consider only optimal experimental configurations so that each method is viewed as favorably as possible, although experimental design constrains may cause laboratory implementation to fall short of the expected SNR performance. Despite all of these caveats, the goal here is to explain the connections between these experimental techniques and to provide a resource for designing and optimizing experimental systems dedicated to low-frequency CRS spectroscopy and microscopy systems.

Data availability statement

The data that support the findings of this study are available upon reasonable request from the authors.

Acknowledgment

Funding from Grant No. DE-SC0019545 from the U.S. Department of Energy and from the W.M. Keck foundation are gratefully acknowledged.

Appendix A. The forced Raman response

The forced Raman response is determined by the coherent driving term and the impulse response of the coherent vibrations. We have defined the forced Raman response in equation (28) as the product of the third order nonlinear susceptibility arising from the vibrational resonances and the power spectral density of the driving term, which leads to the expression

$$\tilde{F}_R(\omega) = \chi^{(3),\mathrm{VR}}_{ijkl}(\omega)\,\tilde{D}(\omega - \Delta_{\mathrm{pu}}), \tag{87}$$

and from which we define the time-domain forced Raman response as $f_R(t) = \mathcal{F}^{-1}\{\tilde{F}_R(\omega)\}$. The Raman susceptibility can be written in a normalized form

$$\chi^{(3),\mathrm{VR}}_{ijkl}(\omega) = \sum_{v,m,n} \chi^{(3),v,mn}_{ijkl}(\Omega_{v,mn})\,\tilde{R}^{mn}_{v}(\omega), \tag{88}$$

where the peak vibrational third order susceptibility is

$$\chi^{(3),v,mn}_{ijkl}(\Omega_{v,mn}) = \frac{N}{6\varepsilon_0}\frac{c_m \langle \alpha'_v\rangle_{ij}\langle \alpha'_v\rangle_{kl}}{\Gamma_{v,mn}\,\Omega_{v,mn}}, \tag{89}$$

and the normalized Raman response for a single vibrational frequency as

$$\tilde{R}^{mn}_{v}(\omega) = \frac{\Gamma_{v,mn}\,\Omega_{v,mn}}{\Omega^2_{v,mn} - \omega^2 - i\omega\Gamma_{v,mn}} \equiv -\frac{\Gamma_{v,mn}\,\Omega_{v,mn}}{(\omega-\omega_1)(\omega-\omega_2)}. \tag{90}$$

This spectral response function is normalized such that $\tilde{R}^{mn}_{v}(\Omega_{v,mn}) = i$. The spectral response contains two simple complex poles, $\omega_{1,2} = \Gamma_{v,mn}/2 \pm \tilde{\Omega}^2_{v,mn}$, and where $\tilde{\Omega}^2_{v,mn} = \Omega^2_{v,mn} - \Gamma^2_{v,mn}/4$. We will use the

approximation that $\tilde{\Omega}_{v,mn} \approx \Omega_{v,mn}$ due to the fact $\Gamma_{v,mn} \ll \Omega_{v,mn}$. With these definitions, we may write the power spectral density of the forced Raman response as

$$\tilde{F}_R(\omega) = \sum_{v,m,n} \chi^{(3),v,mn}_{ijkl}(\Omega_{v,mn})\, \tilde{R}^{mn}_v(\omega)\, \tilde{D}(\omega - \Delta_{\rm pu}). \tag{91}$$

The time-domain forced Raman response,

$$f_R(t) = \sum_{v,m,n} f^{mn}_v(t), \tag{92}$$

is a superposition the response of each vibrational level beat frequency that is obtained from the convolution of the driving term, $d(t)$, the normalized time domain response, $h^{mn}_v(t)$, giving the expression

$$f^{mn}_v(t) = \chi^{(3),v,mn}_{ijkl}(\Omega_{v,mn})\, \Gamma_{v,mn}\, d(t) * h^{mn}_v(t) \tag{93}$$

Here $*$ is the convolution operator and we have also defined the normalized time-domain response of a single Raman vibrational resonance for a vibrational frequency between levels m and n at the the inverse Fourier transform

$$h^{mn}_v(t) = \frac{1}{\Gamma_{v,mn}} \mathcal{F}^{-1}\{\tilde{R}^{mn}_v(\omega)\} = \frac{1}{\Gamma_{v,mn}} \frac{1}{2\,\pi} \int_{-\infty}^{\infty} \tilde{R}^{mn}_v(\omega)\, e^{i\omega t}\, d\omega. \tag{94}$$

This relationship is readily evaluated in the complex plane by means of Cauchy's theorem. The choice of the contour enforces causality, and after a few steps of algebra we obtain the vibrational impulse response

$$h^{mn}_v(t) = \sin(\Omega_{v,mn}\, t)\, {\rm e}^{-\frac{1}{2}\Gamma_{v,mn}\, t}\, \Theta(t). \tag{95}$$

Note that $\Theta(t)$ is the Heavyside unit step function. The temporal response is normalized to unity at $t = 0$.

We are now in a position to consider the driven Raman response, which we express in terms of the non-instantaneous vibrational response to the effective linear optical susceptibility. In the case of a particular vibrational frequency, by virtue of Green's theorem, the convolution reads

$$d(t) * h^{mn}_v(t) = \int_{-\infty}^{\infty} h^{mn}_v(t-s)\, d(s)\, \cos(\Delta_{\rm pu}\, s + \delta\phi_{\rm pu})\, ds, \tag{96}$$

where earlier, we defined $d(t) = |u(t)|^2/T_n$ and $\delta\phi_{\rm pu} = \angle A_k - \angle A_l$ iis the phase difference between fields k and l. Explicitly taking into account the causality enforced by the Heavyside step function, we may write

$$d(t) * h^{mn}_v(t) = \int_{-\infty}^{t} \sin(\Omega_{v,mn}\,(t-s))\, {\rm e}^{-\frac{1}{2}\Gamma_{v,mn}\,(t-s)}\, d(s)\, \cos(\Delta_{\rm pu}\, s + \delta\phi_{\rm pu})\, ds. \tag{97}$$

Appendix B. Noise in CRS signal detection

The sensitivity of all optical measurements are limited by noise. Here, we review the characteristics of three typical detectors used for CRS and identity the power ranges where the three dominant noise processes limit the signal to noise ration of the desired CRS signal. These regimes are leveraged in the main body of the paper to illustrate noise limited detection for the low frequency CRS detection modes and for their operation over a large range of analyte concentrations. The concentration dependence is critical because the signal power varies with the analyte concentration, which means that the dominant noise process in signal detection depends directly on the concentration. We will consider the current generated by an incident signal power of $\bar{p}_{\rm sig}$ incident on a photodetector with a responsivity of $\mathcal{R}$, with units of A W^{-1}, that flows into a terminating impedance of R_T, with units of ohms, to produce a signal voltage of $v_{\rm sig} = R_T \mathcal{R} \bar{p}_{\rm sig}$.

Three dominant noise sources appear during optical detection that can mask the CRS signal voltage: shot noise, Johnson noise, and relative intensity fluctuations (RIN) from the light sources. In all cases we will assume that the detection bandwidth is narrow enough the the noise power spectral density (PSD) may be assumed to be constant across the detection bandwidth, $\Delta f = (2\,\Delta t)^{-1}$, that we characterize in terms of a detector integration time Δt. The individual rms noise voltages are then given by the following expressions, with the rms Johnson noise voltage given by

$$v_J = \sqrt{2\,T k_B R_T/\Delta t}, \tag{98}$$

the rms shot noise voltage given by

$$v_{\text{shot}} = R_T \sqrt{e(\mathcal{R}\bar{p}_{\text{bkg}} + i_D)/\Delta t}, \tag{99}$$

and the rms RIN noise voltage given by

$$v_{\text{RIN}} = R_T \mathcal{R} \bar{p}_{\text{bkg}} 10^{\sigma_{\text{RIN}}/20}/\sqrt{2\,\Delta t}. \tag{100}$$

The parameters in these formulae are the detector temperature, T, in Kelvins, the Boltzmann constant, k_B, the elementary charge, e, the detector dark current, i_D, and the relative intensity noise, σ_{RIN}, centered on mean detection offset frequency and is given in units of dBc Hz^{-1}. The power used in the noise calculation, $\bar{p}_{\text{bkg}}$, can be either the total signal power or a larger background power, depending on the CRS detection mode. The SNR performance of a particular CRS technique is strongly dependent on the source of the background noise. The signal-to-noise (SNR) ratio will be considered for a range of conditions for each of the CRS spectroscopy techniques. In all cases, we may write the SNR in terms of an SNR coefficient that is independent of the integration time, with the form SNR $= \kappa\sqrt{\Delta t}$.

The noise processes are independent and add in quadrature so that the total rms noise voltage is written as

$$v_t = \sqrt{v_J^2 + v_{\text{shot}}^2 + v_{\text{RIN}}^2}. \tag{101}$$

For low incident power levels, the noise is dominated by Johnson noise, and is thus independent of of the signal power, producing an SNR coefficient in the low-power limit given by

$$\kappa_J = M_{\text{CRS}}\,\Upsilon_J, \tag{102}$$

where we have assumed that the signal power is related to the probe pulse power by $\bar{p}_{\text{sig}} = M_{\text{CRS}}\,\bar{p}_{\text{pr}}$. We have defined the parameter $\Upsilon_J = \bar{p}_{\text{pr}}\sqrt{(R_T\mathcal{R}^2)/(2\,k_B\,T)}$. This expression shows that in this low power limit, the SNR scales linearly with the average signal power incident on the detector. This limiting case is only relevant for methods that scatter light to new frequencies or spatial positions that can be isolated from the incident light. Such CRS methods include transient grating and single pulse CARS methods.

At intermediate power levels, the noise is dominated by shot noise, leading to an SNR coefficient of

$$\kappa_{\text{shot}} = W_{\text{CRS}}\,\delta\phi_0^v\,\Upsilon_{\text{pr}}, \tag{103}$$

In the shot noise limit, the SNR scales with the square root of the average power incident on the detector, which appears in the term $\Upsilon_{\text{pr}} = \sqrt{\mathcal{R}\bar{p}_{\text{pr}}/e}$. Shot noise is fundamental to light detection and can not be mitigated as in the case of RIN (e.g. balanced detection) or Johnson noise (cooling the detector).

At high enough power levels, when using a single photodetector, the noise will be dominated by intensity fluctuations from the light source. The SNR coefficient in this limiting case is now independent of the power incident on the detector, and reads

$$\kappa_{\text{RIN}} = Y_{\text{CRS}}\,\delta\phi_0^v\,\Upsilon_{\text{RIN}}. \tag{104}$$

The parameter $\Upsilon_{\text{RIN}} = \sqrt{2}\,10^{-\sigma_{\text{RIN}}/20}$ depends entirely on the intensity noise from the laser source. The RIN noise PSD exhibits a strong detector spectral dependence (i.e. detection integration time), and the spectral dependence is generally modelled with an offset frequency scaling of $f_{\text{off}}^{-\alpha}$, where $\alpha \geq 1$. Because of the strong spectral dependence of RIN, much lower RIN values can be obtained in the detection of light by using modulation transfer to detect the signal about a narrow frequency range at an offset frequency larger that $1/\tau_{\text{e}}$, where τ_{e} is the excited state storage lifetime of the laser gain medium. Such a strategy is employed with pump modulation and lock-in detection in many CRS methods.

Due to the linear scaling of RIN rms noise voltage, at high enough power levels, RIN dominates the CRS signal SNR. The power threshold for RIN dominance is computed with

$$p_3 = \frac{2\,e}{\text{R}}\,10^{-\sigma_{\text{RIN}}/10}. \tag{105}$$

Here the dark current can be neglected because it is orders of magnitude smaller than the photocurrent at these power levels. In the RIN limit the SNR scaling is set by Υ_{RIN}, and is independent of the average probe pulse power. At very low power levels, Johnson noise will always dominate. Here, the CRS SNR scales with Υ_{J} and SNR improvement scales linearly with the average probe pulse power. The low-power limit depends on

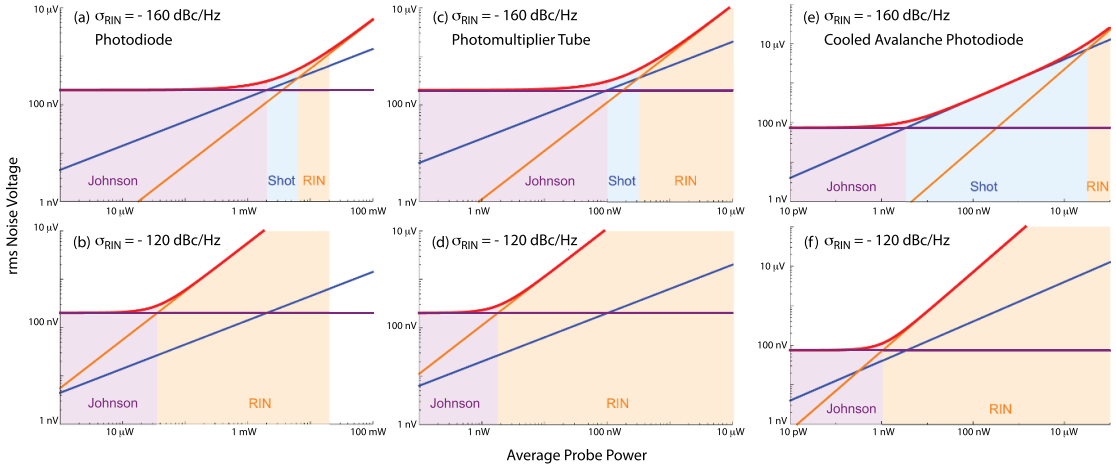

Figure 12. Typical regions of operation for optical detectors used for CRS showing the ranges of noise-dominated behaviors for a range incident power levels for the detectors with low and high levels of RIN for a photodiode with low (a) and high (b) RIN, a photomultiplier tube (PMT) with low (c) and high (d) RIN, and a cooled (to 200) (k) avalanche photodiode (APD) with low (e) and high (f) RIN. The red line shows the total rms voltage noise, whereas, Johnson noise is in purple, shot noise is in blue, and RIN is orange. The shaded regions highlight the areas of noise domination for these three noise processes.

the value of RIN. For high values of RIN, we will transition directly from a RIN dominated noise to Johnson dominated noise at a threshold power of

$$p_2 = 10^{-\sigma_{\rm RIN}/20}\sqrt{\frac{4\,k_B\,T}{\mathrm{R}^2\,R_T}}. \tag{106}$$

However, when RIN values are low enough, then below p_3 the rms voltage noise is dominated by shot noise and then as the power drops further, the transition to Johnson noise occurs at

$$p_1 = \frac{2\,k_B\,T}{e\,\mathrm{R}\,R_T} - \frac{i_D}{\mathrm{R}}. \tag{107}$$

When RIN is low enough, we can directly operate in a shot noise limited regime for an intermediate range of power levels in the range of $p_1 \leq \bar{p}_{\rm pr} \leq p_3$. In this the shot noise limit, CRS SNR scales with $\Upsilon_{\rm SH,j}$ and SNR improvement scales with the square root of the average probe pulse power. Otherwise, when RIN levels are too high, there is not a shot noise limited regime, and the noise behavior switches from Johnson to RIN at p_2. In the RIN-dominated regime RIN, can be suppressed by 20–50 dB with balanced detection, allowing the recovery of shot-noise limited operation even at high power levels. This then allows for an improvement of shot-noise limited SNR up to the saturation power of the detector.

To facilitate identifying favorable detectors for various CRS methods and to ascertain which noise process is dominate for a given operating condition, we consider the typical noise performance of several typical detectors: a photodiode, a photomultiplier tube (PMT), and a cooled avalanche photodiode (APD). For each detector, we consider two levels of RIN, with $\sigma_{\rm RIN} = -120$ dBc Hz^{-1} for a high value of RIN and $\sigma_{\rm RIN} = -160$ dBc Hz^{-1} for a low value of RIN.

Figures 12(a) and (b) shows the rms noise voltage as a function of average power on the detector for a typical photodiode with parameters R = 0.5 A W^{-1}, $R_T = 50\,\Omega$, $T = 293$ K, and $i_D = 0.3$ nA. For this detector, $p_1 = 2$ mW. For low RIN, $p_2 = 3.6$ mW and $p_3 = 6.41$ mW, as we see in figure 12(a). However for high RIN, the shot-noise limited operation vanishes detection noise switches from RIN to Johnson when the average probe power drops below $p_2 = 36\,\mu$W as seen in figure 12(a). For this detector the SNR scales according to $\Upsilon_{\rm J} = 3.93 \times 10^{10}\,\bar{p}_{\rm pr}$ in the Johnson noise limit, $\Upsilon_{\rm pr} = 1.77 \times 10^{9}\,\sqrt{\bar{p}_{\rm pr}}$ in the shot limit, $\Upsilon_{\rm RIN} = 1.41 \times 10^{8}$ and $\Upsilon_{\rm RIN} = 4.47 \times 10^{5}$ in the RIN limit for low and high RIN, respectively.

Figures 12(c) and (d) shows the rms noise voltage as a function of average power on a typical photomultiplier tube with parameters R = 10 000 A W^{-1}, $R_T = 50\,\Omega$, $T = 293$ K, and $i_D = 0.3$ nA. For this detector, $p_1 = 101$ nW. For low RIN, $p_2 = 180$ nW and $p_3 = 320$ nW, as we see in figure 12(c). However for high RIN, the shot-noise limited operation vanishes detection noise switches from RIN to Johnson when the average probe power drops below $p_2 = 1.80\,\mu$W as seen in figure 12(d). For this detector the SNR scales according to $\Upsilon_{\rm J} = 3.93 \times 10^{10}\,\bar{p}_{\rm pr}$ in the Johnson noise limit, $\Upsilon_{\rm pr} = 7.86 \times 10^{14}\,\sqrt{\bar{p}_{\rm pr}}$ in the shot limit, $\Upsilon_{\rm RIN} = 2.50 \times 10^{11}$ and $\Upsilon_{\rm RIN} = 4.47 \times 10^{5}$ in the RIN limit for low and high RIN, respectively.

Figures 12(e) and (f) show the rms noise voltage as a function of average power on the detector for a typical cooled avalanche photodiode with parameters $R = 100$ A W^{-1}, $R_T = 100\,k\Omega$, $T = 200$ K, and $i_D = 10^{-19}$ A. For this detector, $p_1 = 3.45$ nW. For low RIN, $p_2 = 332$ nW and $p_3 = 32\,\mu$W, as we see in figure 12(e). However for high RIN, the shot-noise limited operation vanishes detection noise switches from RIN to Johnson when the average probe power drops below $p_2 = 1.05$ nW as seen in figure 12(f). For this detector the SNR scales according to $\Upsilon_J = 4.26 \times 10^{10}\,\bar{p}_{pr}$ in the Johnson noise limit, $\Upsilon_{pr} = 2.50 \times 10^9\,\sqrt{\bar{p}_{pr}}$ in the shot limit, $\Upsilon_{RIN} = 1.41 \times 10^8$ and $\Upsilon_{RIN} = 4.47 \times 10^5$ in the RIN limit for low and high RIN, respectively.

ORCID iD

Randy A Bartels https://orcid.org/0000-0003-0530-0435

References

[1] Smekal A 1923 *Naturwissenschaften* **11** 873–5
[2] Raman C V and Krishnan K S 1928 *Nature* **121** 501–2
[3] Landsberg G and Mandelstam L 1928 *Die Naturwissenschaften* **16** 557–8
[4] Malard L, Pimenta M, Dresselhaus G and Dresselhaus M 2009 *Phys. Rep.* **473** 51–87
[5] Butler H J *et al* 2016 *Nat. Protocols* **11** 664–87
[6] Parrott E P J, Fischer B M, Gladden L F, Zeitler J A and Jepsen P U 2012 Terahertz spectroscopy of crystalline and non-crystalline solids *Terahertz Spectroscopy and Imaging* (Berlin: Springer) pp 191–227
[7] Larkin P J, Dabros M, Sarsfield B, Chan E, Carriere J T and Smith B C 2014 *Appl. Spectrosc.* **68** 758–76
[8] Hudson B S 2009 Vibrational spectroscopy via inelastic neutron scattering *Frontiers of Molecular Spectroscopy* (Amsterdam: Elsevier) pp 597–622
[9] Parrott E P and Zeitler J A 2015 *Appl. Spectrosc.* **69** 1–25
[10] Balakhnina I A, Brandt N N, Chikishev A Y, Mankova A A and Shpachenko I G 2017 *J. Biomed. Opt.* **22** 1–6
[11] Kalanoor B S, Ronen M, Oren Z, Gerber D and Tischler Y R 2017 *ACS Omega* **2** 1232–40
[12] Turton D A, Senn H M, Harwood T, Lapthorn A J, Ellis E M and Wynne K 2014 *Nat. Commun.* **5** 3999
[13] Kuramochi H, Takeuchi S, Kamikubo H, Kataoka M and Tahara T 2019 *Sci. Adv.* **5** eaau4490
[14] Tsen K T, Dykeman E C, Sankey O F, Lin N T, Tsen S W D and Kiang J G 2006 *Virol. J.* **3** 79
[15] Yeh Y T *et al* 2020 *Proc. Natl Acad. Sci.* **117** 895–901
[16] Blatz L A 1967 *J. Chem. Phys.* **47** 841–9
[17] Moser C and Havermeyer F 2009 *Appl. Phys.* B **95** 597–601
[18] Moser C and Havermeyer F 2010 Compact raman spectrometer system for low frequency spectroscopy *Optical Components and Materials VII* ed S Jiang, M J F Digonnet, J W Glesener and J C Dries (SPIE)
[19] Glebov A L, Mokhun O, Rapaport A, Vergnole S, Smirnov V and Glebov L B 2012 Volume Bragg gratings as ultra-narrow and multiband optical filters *Micro-Optics 2012* ed H Thienpont, J Mohr, H Zappe and H Nakajima (SPIE)
[20] Nims C, Cron B, Wetherington M, Macalady J and Cosmidis J 2019 *Sci. Rep.* **9** 7971
[21] Ruhman S, Joly A, Kohler B, Williams L and Nelson K 1987 *Revue de Phys. Appl.* **22** 1717–34
[22] Domingue S R, Winters D G and Bartels R A 2014 *Opt. Lett.* **39** 4124–7
[23] Ren L, Frostig H, Kumar S, Hurwitz I and Silberberg Y 2017 *Opt. Express* **25** 28201–9
[24] Raanan D, Ren L, Oron D and Silberberg Y 2018 *Opt. Lett.* **43** 470–3
[25] Raanan D, Lüttig J, Silberberg Y and Oron D 2018 *APL Photon.* **3** 092501
[26] Ren L, Hurwitz I, Raanan D, Oulevey P, Oron D and Silberberg Y 2019 *Optica* **6** 52–5
[27] Raanan D, Audier X, Shivkumar S, Asher M, Menahem M, Yaffe O, Forget N, Rigneault H and Oron D 2019 *Opt. Lett.* **44** 5153
[28] Yan Y, Gamble E B and Nelson K A 1985 *J. Chem. Phys.* **83** 5391–9
[29] Silberberg Y 2009 *Annu. Rev. Phys. Chem.* **60** 277–92
[30] Tolles W M, Nibler J W, McDonald J R and Harvey A B 1977 *Appl. Spectrosc.* **31** 253–71
[31] Long D A 2002 *The Raman Effect* (New York: Wiley)
[32] Cheng J X, Volkmer A and Xie X S 2002 *J. Opt. Soc. Am.* B **19** 1363–75
[33] Evans C L and Xie X S 2008 *Ann. Rev. Anal. Chem.* **1** 883–909 PMID: 20636101
[34] Zhang C, Zhang D and Cheng J X 2015 *Annu. Rev. Biomed. Eng.* **17** 415–45 PMID: 26514285
[35] Zhang C and Cheng J X 2018 *APL Photon.* **3** 090901
[36] Rigneault H and Berto P 2018 *APL Photon.* **3** 091101
[37] Pauling L 1936 *Introduction to Quantum Mechanics, With Applications to Chemistry* 1st edn, ed L Pauling and E B Wilson Jr (London: McGraw-Hill) 1935 30s (Dover), p xiii+468
[38] Hellwarth R W 1977 *Prog. Quantum Electron.* **5** 1–68
[39] Stähelin M, Moylan C R, Burland D M, Willetts A, Rice J E, Shelton D P and Donley E A 1993 *J. Chem. Phys.* **98** 5595–603
[40] Zyss J and Oudar J L 1982 *Phys. Rev.* A **26** 2028–48
[41] Singer K D, Kuzyk M G and Sohn J E 1987 *J. Opt. Soc. Am.* B **4** 968–76
[42] Hartinger K, Nirmalgandhi S, Wilson J and Bartels R A 2005 *Opt. Express* **13** 6919–30
[43] Hartinger K and Bartels R A 2008 *Appl. Phys. Lett.* **92** 021126
[44] Hartinger K and Bartels R A 2008 *Opt. Lett.* **33** 1162–4
[45] Brasselet S 2011 *Adv. Opt. Photon.* **3** 205
[46] GUBSKAYA A V and KUSALIK P G 2001 *Mol. Phys.* **99** 1107–20
[47] Silbey R J 1996 *J. Am. Chem. Soc.* **118** 12872
[48] Butcher P N and Cotter D 1990 *The Susceptibility Tensors* (Cambridge: Cambridge University Press) Cambridge Studies in Modern Optics, pp 56–121
[49] Schlup P, Wilson J W and Bartels R A 2009 *IEEE J. Quantum Electron.* **45** 777–82

[50] Yuratich M and Hanna D 1977 *Mol. Phys.* **33** 671–82
[51] Rahav S and Mukamel S 2010 *Proc. Natl Acad. Sci.* **107** 4825–9
[52] Cleff C, Rigneault H, Brasselet S and Duboisset J 2017 *Phys. Rev.* A **96** 013851
[53] Walter M and Moseler M 2020 *J. Chem. Theory Computat.* **16** 576–86
[54] Acosta-Maeda T E, Misra A K, Porter J N, Bates D E and Sharma S K 2016 *Appl. Spectrosc.* **71** 1025–38
[55] Shen Y R and Bloembergen N 1965 *Phys. Rev.* **137** A1787–805
[56] Bartels R A, Weinacht T C, Wagner N, Baertschy M, Greene C H, Murnane M M and Kapteyn H C 2001 *Phys. Rev. Lett.* **88** 013903
[57] Bartels R A, Weinacht T C, Leone S R, Kapteyn H C and Murnane M M 2002 *Phys. Rev. Lett.* **88** 033001
[58] Masihzadeh O, Baertschy M and Bartels R A 2006 *Opt. Express* **14** 2520–32
[59] Hartinger K and Bartels R 2006 *Opt. Lett.* **31** 3526–8
[60] Hartinger K and Bartels R 2008 *J. Opt. Soc. Am.* B **25** 407–13
[61] Shimizu F 1967 *Phys. Rev. Lett.* **19** 1097–100
[62] Alfano R R and Shapiro S L 1970 *Phys. Rev. Lett.* **24** 584–7
[63] Brewer R G 1967 *Phys. Rev. Lett.* **19** 8–10
[64] Kupka D, Wilson J W, Masihzadeh O and Bartels R A 2010 *Chem. Phys. Lett.* **490** 97–101
[65] Wilson J W and Bartels R A 2012 *J. Opt. Soc. Am.* B **29** 1875–83
[66] Yuratich M A 1979 *Mol. Phys.* **38** 625–55
[67] Bartels R A, Weinacht T C, Leone S R, Kapteyn H C and Murnane M M 2002 *Phys. Rev. Lett.* **88** 033001
[68] Hertz E, Chaux R, Faucher O and Lavorel B 2001 *J. Chem. Phys.* **115** 3598–603
[69] Weinacht T C, Bartels R, Backus S, Bucksbaum P H, Pearson B, Geremia J M, Rabitz H, Kapteyn H C and Murnane M M 2001 *Chem. Phys. Lett.* **344** 333–8
[70] Oron D, Dudovich N and Silberberg Y 2002 *Phys. Rev. Lett.* **89** 273001
[71] Oron D, Dudovich N and Silberberg Y 2003 *Phys. Rev. Lett.* **90** 213902
[72] Gershgoren E, Bartels R A, Fourkas J T, Tobey R, Murnane M M and Kapteyn H C 2003 *Opt. Lett.* **28** 361–3
[73] Masihzadeh O, Baertschy M and Bartels R A 2006 *Opt. Express* **14** 2520–32
[74] Audier X, Heuke S, Volz P, Rimke I and Rigneault H 2020 *APL Photon.* **5** 011101
[75] Merlin R 1997 *Solid State Commun.* **102** 207–20
[76] Liu Y, Frenkel A, Garrett G A, Whitaker J F, Fahy S, Uher C and Merlin R 1995 *Phys. Rev. Lett.* **75** 334–7
[77] Wahlstrand J K, Merlin R, Li X, Cundiff S T and Martinez O E 2005 *Opt. Lett.* **30** 926–8
[78] Wilson J W, Schlup P and Bartels R A 2008 *Chem. Phys. Lett.* **463** 300–4
[79] Wilson J W, Schlup P and Bartels R 2008 *Opt. Lett.* **33** 2116–18
[80] McMorrow D and Lotshaw W T 1991 *J. Phys. Chem.* **95** 10395–406
[81] Bachler B R, Fermann M E and Ogilvie J P 2012 *Opt. Express* **20** 835–44
[82] Nelson K A, Dlott D D and Fayer M D 1979 *Chem. Phys. Lett.* **64** 88–93
[83] De Silvestri S, Fujimoto J G, Ippen E P, Gamble E B, Williams L R and Nelson K A 1985 *Chem. Phys. Lett.* **116** 146–52
[84] Voehringer P and Scherer N F 1995 *J. Phys. Chem.* **99** 2684–95
[85] Wahlstrand J K, Merlin R, Li X, Cundiff S T and Martinez O E 2005 *Opt. Lett.* **30** 926–8
[86] Gautier C A, Lefumeux C, Albert O and Etchepare J 2000 *Opt. Commun.* **178** 217–24
[87] Bartels R A and Winters D G 2018 Apparatus and method for measurement of optical frequency shifts US Patent App. 15/317,963
[88] Smith D R, Field J J, Winters D G, Domingue S R, Rininsland F, Kane D J, Wilson J W and Bartels R A 2021 *APL Photon.* **6** 026107
[89] McFerran J J, Ivanov E N, Bartels A, Wilpers G, Oates C W, Diddams S A and Hollberg L 2005 *Electron. Lett.* **41** 650–1
[90] Jung K and Kim J 2015 *Opt. Lett.* **40** 316–19
[91] Song Y, Kim C, Jung K, Kim H and Kim J 2011 *Opt. Express* **19** 14518–25
[92] Kim J and Kärtner F 2010 *Laser Photon. Rev.* **4** 432–56
[93] Dudovich N, Oron D and Silberberg Y 2002 *Nature* **418** 512 E
[94] Dudovich N, Oron D and Silberberg Y 2003 *J. Chem. Phys.* **118** 9208–15
[95] Polack T, Oron D and Silberberg Y 2005 *Chem. Phys.* **318** 163–9
[96] Ogilvie J P, Beaurepaire E, Alexandrou A and Joffre M 2006 *Opt. Lett.* **31** 480–2
[97] Sinjab F, Hashimoto K, Zhao X, Nagashima Y and Ideguchi T 2020 *Opt. Lett.* **45** 1515–8
[98] Bartels R, Backus S, Murnane M and Kapteyn H 2003 *Chem. Phys. Lett.* **374** 326–33
[99] Camp Jr C H and Cicerone M T 2015 *Nat. Photon.* **9** 295–305
[100] Oron D, Dudovich N, Yelin D and Silberberg Y 2002 *Phys. Rev. Lett.* **88** 063004
[101] Lim S H, Caster A G and Leone S R 2005 *Phys. Rev.* A **72** 041803
[102] Katz O, Levitt J M, Grinvald E and Silberberg Y 2010 *Opt. Express* **18** 22693–701
[103] Natan A, Levitt J M, Graham L, Katz O and Silberberg Y 2012 *Appl. Phys. Lett.* **100** 051111
[104] Prince R C, Frontiera R R and Potma E O 2017 *Chem. Rev.* **117** 5070–94